DEVELOPMENT OF PILLARED M(IV) PHOSPHATE PHOSPHONATE INORGANIC ORGANIC HYBRID ION EXCHANGE MATERIALS FOR APPLICATIONS IN SEPARATIONS FOUND IN THE NUCLEAR FUEL CYCLE

A Dissertation

by

JONATHAN DAVID BURNS

Submitted to the Office of Graduate Studies of
Texas A&M University
in partial fulfillment of the requirements for the degree of

DOCTOR OF PHILOSOPHY

Approved by:

Chair of Committee,	Abraham Clearfield
Committee Members,	Timothy Hughbanks
	Charles M. Folden III
	Sean McDeavitt
Head of Department,	David H. Russell

December 2012

Major Subject: Chemistry

ABSTRACT

This dissertation focuses on key intergroup and intragroup separations found in the back end of the nuclear fuel cycle, specifically americium from lanthanides and americium from other actinides, most importantly americium from curium. Our goal is to implement a liquid-solid separation process to reduce waste and risk of contamination by the development of metal(IV) phosphate phosphonate inorganic organic hybrid ion exchange materials with the ideal formula of $M(O_6P_2C_6H_4)_{0.5}(O_3PO\mathit{A}) \bullet \mathit{n}H_2O$, where M = Zr or Sn, *A* = H or Na. These materials have previously shown to have high affinity for Ln, this work will expand on the previous studies and provide methods for the above target separation, exploiting oxidation state and ion charge to drive the separation process.

The optimum hydrothermal reaction conditions were determined by adjusting parameters such as reaction temperature and time, as well as the phosphonate to phosphate (pillar-to-spacer) ligands ratio. Following these results four bulk syntheses were performed and their ion exchange properties were thoroughly examined. Techniques such as inductively coupled mass spectrometry and liquid scintillation counting were used to determine the affinity of the materials towards Na^{+}, Cs^{+}, Ca^{2+}, Sr^{2+}, Ni^{2+}, Nd^{3+}, Sm^{3+}, Ho^{3+}, Yb^{3+}, NpO_2^{+}, Pu^{4+}, PuO_2^{2+}, Am^{3+}, AmO_2^{+}, and Cm^{3+}.

Separation factors in the thousands have been observed for intergroup separations of the Ln from the alkali, alkaline earth, and low valent transition metals. A new method for Am oxidation was developed, which employed $Na_2S_2O_8$ as the oxidizing agent and $Ca(OCl)_2$ as the stabilizing agent for AmO_2^+ synthesis. Separation factors of 30-60 for Nd^{3+} and Eu^{3+} from AmO_2^+, as well as 20 for Cm^{3+} from AmO_2^+ were observed at pH 2. The work herein shows that a liquid-solid separation can be carried out for these difficult separations by means of oxidation and ion exchange.

DEDICATION

To my mother, Patricia, and my father, Timothy, who's expectations for success were never without tireless words of encouragement. Your love and support has allowed me to push through the growing pains and emerge better than I started. To my brother, Joshua, you have taught me what it means to believe in oneself and the power that can be found in self-confidence, something that has been in short supply many times in my life. To my wife, Jennifer, who's dreams, dedication, and determination to my success have always overwhelmed me and often given me the extra strength I needed to succeed, without you this work would not be complete, and it is to you that I also dedicate my life and love.

ACKNOWLEDGEMENTS

The following are a few names among many who have contributed in no small manner to my development in both professional and educational capacities. While each one has had a unique role, it is their combined effort that has resulted in the philosopher, scientist, and man I am today.

Robert Cope served as my first exposure to the mystery and wonder of the hard sciences of chemistry and physics, which later developed into an understanding and appreciation for the order found in the natural universe. Your excitement for teaching students and the creativity in which you do so, has left many lessons still resonating in my mind.

Dr. Donald T. Reed who gave me my first opportunity to pursue chemistry outside of academia and has been a scientific mentor for the past six years. That first summer you taught me one of the most valuable lessons I have ever learned in chemistry, "Two hours at your desk thinking, can save two weeks in the lab." Thank you for your continued support.

Dr. Marian Borkowski who has served not only as a scientific mentor for my journey from undergraduate, to graduate, to professional scientist; but has, as a friend, imparted me with many words of wisdom. Your friendship has been evident by the countless hours you have spent allowing me to learn, rather than telling me what to know. Your encouragement has given me the confidence needed to carry out rigorous scientific research. A better mentor I have yet to meet.

Dr. Sherry Yennello, who opened the door for me to come to Texas A&M, and who taught me that nobody's path is the same in graduate school or in life. Thank you for your grace as I found my path at A&M.

I also would like to acknowledge the members of my graduate committee, Dr. Timothy Hughbanks, Dr. Charles M. Folden III, and Dr. Sean McDeavitt. They were asked to sit on my committee because of the respect I have for them in their area of scientific expertise and their willingness to push and teach me to learn.

To my family, both nuclear and surrogate, who have offered me support intellectually, emotionally, financially, and spiritually. Without you this work would not have possible, and to you is owed a share in my success at Texas A&M University.

Finally, I gratefully acknowledge Dr. Abraham Clearfield, you have truly been a blessing from God. I could not ask for a better research advisor, your combination of guidance and free rein has given me the opportunity to become an independent thinker and researcher. You have allowed me to work on a project that I am very interested and passionate about and to learn, stumble, and ultimately succeed in my development as a scientist. Your words of wisdom have made me a better scientist as well as a better human being. To you I owe a debt that I will never be able to repay, I only hope that my hard work over the past four years has met your expectations.

NOMENCLATURE

α–PHA	Alpha Pulse Height Analysis
α–ZrP	Alpha Zirconium Phosphate
An	Actinide(s)
CEMRC	Carlsbad Environmental Monitoring and Research Center
ddi	Distilled Deionized
EDS	Energy Dispersive System
FP	Fission Products
HDEHP	Bis-(2-Ethylhexyl) Phosphoric Acid
ICP-AES	Inductively Coupled Plasma Atomic Emission Spectroscopy
ICP-MS	Inductively Coupled Plasma Mass Spectrometry
K_d	Distribution Coefficient
LANL-CO	Los Alamos National Laboratory-Carlsbad Operations
Ln	Lanthanide(s)
LSC	Liquid Scintillation Counting
MA	Minor Actinides
MAS	Magic Angle Spinning
NMR	Nuclear Magnetic Resonance
P	Pillar Ligand
PGT	Princeton Gamma Tech
S	Spacer Ligand

SEM	Scanning Electron Microscope
SF	Separation Factors
SRNL	Savannah River National Laboratory
TGA	Thermogravimetric Analysis
TW	Terawatts
WDS	Wavelength-Dispersive Spectrometers
XRPD	X-ray Powder Diffraction
Z_{eff}	Effective Charge

TABLE OF CONTENTS

Page

LIST OF FIGURES

FIGURE Page

FIGURE Page

LIST OF TABLES

TABLE Page

TABLE Page

CHAPTER I

INTRODUCTION

1.1 Identifying the problem

The demand for energy is ever present and ever growing as the world's population continues to grow. Energy has established itself as a necessity in any economically growing society. The rate at which energy is being consumed is increasing faster than the rate of world population growth. In the last several decades we have seen these demands further strained by the modernization and mass urbanization of highly populated countries such as China and India, adding roughly one billion new energy users to the currently growing population base. The exodus from the countryside into the city cannot be stemmed and should not be questioned, as it provides these populations access to a new world of great potential in the areas of: education, technological advancement, healthcare, and overall standard of living. Energy, when looked back on by history, may turn out to be the biggest problem of the 21st century.

In the pursuit of short-term increases in the standard of living, the impacts imparted to future generations must be in the forefront of energy policy. Gagnon *et al.* [1] performed a life cycle assessment on a variety of energy sources, which examined the "cradle-to-grave" overall environmental impact on each energy source. Nash *et al.* [2] later revised the study to better identify the role of nuclear power in the future. The life

cycle assessment identified and ranked the respective energy source by four major areas of concern: greenhouse gas emissions, SO_2 emissions, direct land requirements, and energy payback ratios. In both emissions categories nuclear scored as well, if not slightly better than most of the "renewable" sources; and greatly outscored all the fossil-fuel sources. Nuclear power had the smallest impact on direct land requirements; but it should be pointed out that final disposal of nuclear waste was not taken into account, as no real stance has been taken on the back end of the fuel cycle in the United States. Nuclear was out scored in payback, but was still competitive with the "renewable" sources. Nash *et al.* pointed out that nuclear is the only energy source that has not been––but has the potential to be—expanded on a large scale to meet the nation's growing energy needs. They also emphasized that, "nuclear plants can be configured to provide continuous on-demand power (no matter what the weather)."

Several analyses have been made on global energy production and consumption [3-5], one of which, prepared by Hoffert *et al.* [5], placed an emphasis on energy concerns of the future. They estimated the global power consumption in 2002 to be ~ 12 terawatts (TW), with ~ 85% of that coming from fossil fuels. The trending of atmospheric CO_2 showed 275 ppm in 1900, 370 ppm in 2000, and is projected to reach 550 ppm in 2100. In conclusion they stated that by the year 2050 nearly 15 TW of emission-free power will be needed to stabilize CO_2 levels at 550 ppm. Nash *et al.* echo the concern, in their synopsis of the Hoffer *et al.* analysis, "fission based nuclear power is the only presently developed technology that could deliver this performance." Ghoniem [4] stated,

"Nuclear energy and renewable resources are necessary components of the energy source mix, which are also carbon free. Nuclear power is a scalable resource that can satisfy [a] larger fraction of electricity generation needs, but concerns over waste, safety and security must be addressed." Nash *et al.* further suggest that known terrestrial reserves of uranium are inadequate to sustain this level of power production if we utilize only the fissile ^{235}U that is present naturally. They conclude, that it is "imperative that development begin immediately on a serious international effort to close the nuclear fuel cycle and to breed additional fissile plutonium." The breeding of new fuel in commercial reactors is currently illegal in the United States due to concerns with waste management and weapons proliferation, and has resulted in a "once-through" or open fuel cycle.

The nuclear fuel cycle, presented in Figure 1 can be broken up into three phases: the front end, middle, and back end. The front end is comprised of mining, milling, conversion, enrichment, and fuel fabrication. The whole reason for the fuel cycle, energy production, occurs in the middle. The back end, however, is slightly more ambiguous as two approaches have been taken. Approach one, the closed fuel cycle, contains three stages: interim storage, reprocessing, and final disposition. Approach two, the "once-through" or open fuel cycle, allows for only a single use of the nuclear fuel and then ideally calls for the disposal of the used fuel by going from interim storage into a geological repository, skipping the reprocessing step entirely.

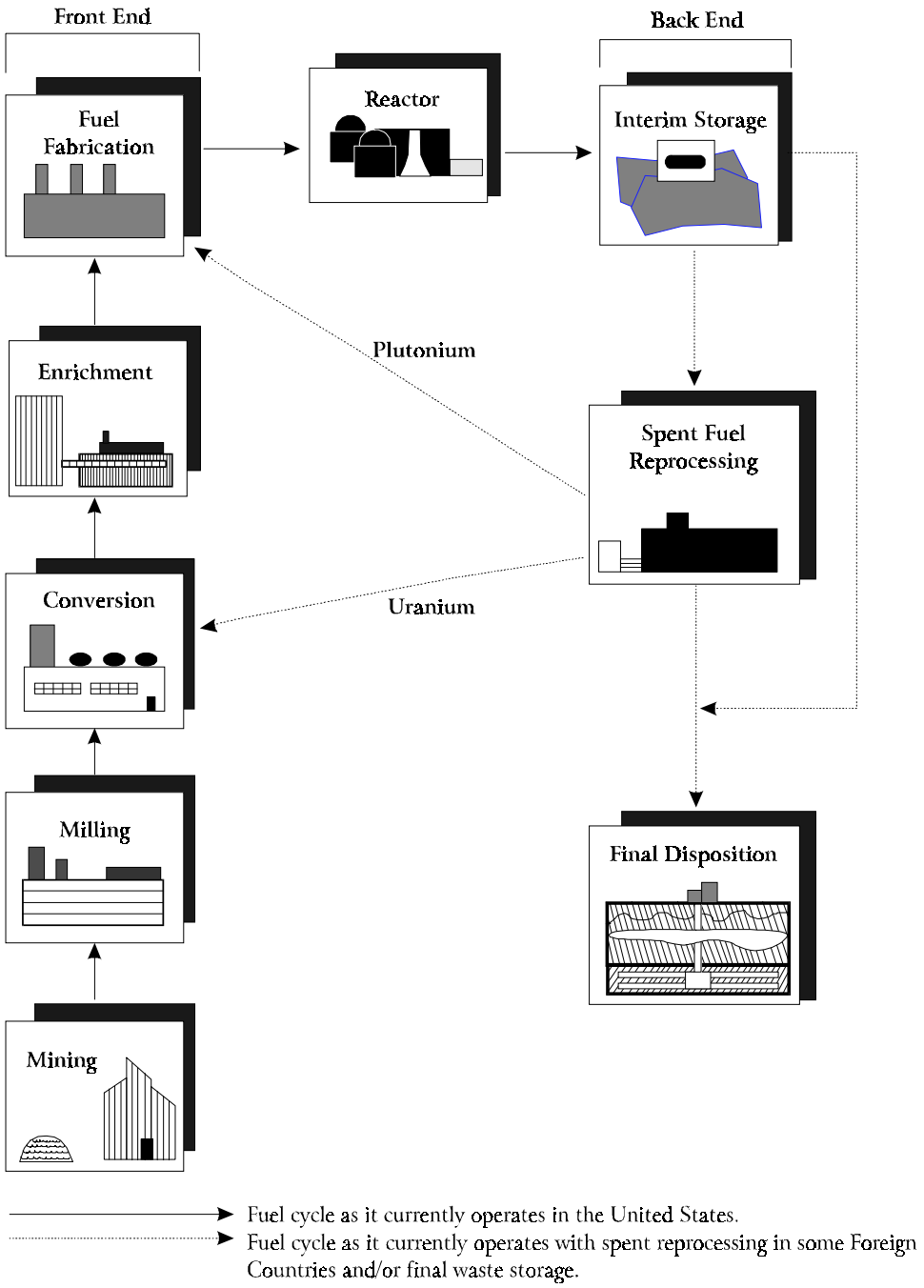

Source: Energy Information Administration.

Figure 1: Nuclear fuel cycle schematic, adapted from the United States Energy Information Administration Nuclear Power Generation and Fuel Cycle Report released September 1, 1997.

In a closed fuel cycle, the reprocessing stage has a number of separation steps that extract out the fission products (FP) and minor actinides (MA) into waste streams while the uranium and plutonium are harvested and reintroduced into the front end, thereby closing the fuel cycle. Some countries, like France, have industrialized this process, generating over 85% of their electricity [4]. They also export a good portion of energy to neighboring countries. In contrast, the United States has adopted the "once-through" approach, where the fuel is used once and sent to a geological repository. (However, no such repository has been, or is currently, in use. Moreover, at present no final geological disposal site has even been identified in the US). This can lead to a strain on the interim storage facilities; however, these facilities have not been commissioned for operation either. The result is the accumulation of 10-60 years worth of used nuclear fuel (the full operational nuclear waste legacy) at any given reactor. This burden of amassed used fuel has begun to tax (pun intended) the facilities and in 2010 [6] a number of electricity utilities, the Nuclear Energy Institute, and the National Association of Utility Regulators filed lawsuits against the US Department of Energy regarding utility industry payments into the Nuclear Waste Fund, which was designed to pay for the transportation and disposal of the used nuclear fuel, and to date, has done neither. Since then several large sums of money have been refunded, with a possibility of more to come in the future [7, 8].

This has resulted in major concerns in expanding the nuclear power industry in the US. While nuclear power has many advantages the major concern lies in the waste generated

in the process. The current stockpiles of waste must be dealt with to make room for future energy production. Like most tasks, it is much easier said than done. To start with, the initial radiation dose emitted by the used assemblies is quite high, and remains so, even after some of the short-lived radionuclides have decayed away. Exposure concerns are present throughout the entire process. Other concerns involve the heat production of waste from species like ^{90}Sr and ^{137}Cs [9-12], and ^{241}Am [13, 14]. In both cases a well-designed separation process can reduce the amount of waste, the space needed to house the waste, and the time needed for the doses to become manageable. One approach to reduce long-term radiotoxicity and heat load is transmutation of the radionuclides to shorter-lived species [15-17]. This approach requires a pure sample of the nuclide of interest, in most cases ^{241}Am. Under acidic conditions americium is most stable as a trivalent cation and behaves very similar to the early lanthanides (Ln), making the separation very difficult. This issue will be discussed in more detail later, in Chapter V.

The Ln also play an important negative role in fuel as many of them have high thermal neutron capture cross sections [18-22]. As the fission products grow in, many of the light Ln are produced and begin to scavenge neutrons. The Ln, unlike fissile materials, capture neutrons without releasing additional neutrons, a process known as "poisoning" because it kills the nuclear chain reaction. The final outcome of this process is too few free neutrons to sustain criticality and the reaction shuts down. Although there is enough poison to prevent a chain reaction from occurring, the poisons only make up a very small

amount by mass of the used fuel, ≤ 1%, while there is still ~ 95% of the original starting material present [23, 24]. This alone should be reason enough to recycle used nuclear fuel. In light of the world's burgeoning energy needs, it is a travesty, that after only 5% of the fuel is consumed the whole assembly is destined for disposal. The answer to the problem is not to avoid it altogether, but rather to allow scientific creativity and ingenuity to run its course and develop a safe system of policies, procedures, and technologies to expand nuclear power to its full potential.

1.2 History α-zirconium phosphate derivatization

The Clearfield Research Group has been investigating zirconium phosphate and its derivatives for the past 50 years. Alpha-zirconium phosphate (α–ZrP), $Zr(HPO_4)_2 \bullet H_2O$, has been known to be an ion exchange material since before it was first crystallized by Clearfield and Stynes in 1964 [25]. Clearfield and Stynes developed methods of synthesizing α–ZrP by refluxing zirconium phosphate gels in phosphoric acid. It was found that both the acid concentration as well as the reflux time played a large roll in the crystallization process. As the H_3PO_4 concentration was increased from 1-12 M the gels converted into crystalline forms much faster, taking ~ 100 hrs in 1 M H_3PO_4 and only 1 hr in 8-12 M H_3PO_4. It was also observed that the crystals themselves had much more rapid growth in the more concentrated acids.

The structure was solved 1969 [26] and then refined in 1977 [27] in the $P2_1/n$ space group with the unit cell dimensions of a = 9.060 (2) Å, b = 5.297 (1) Å, c = 15.414 (3) Å, β = 101.71 (2)º and Z = 4 (see Figure 2). α–ZrP can be described, as a layered structure comprised of octahedrally coordinated zirconium atoms bound to six oxygen atoms from six different phosphate groups. The phosphate groups are bound to the layer by three oxygen atoms, with a protonated oxygen pointing towards the interlayer space, along with one unit formula water molecule that does not hydrogen bond the layers together. The interlayer distance of α–ZrP is 7.6 Å and each layer is offset by 1/3 a_h and 2/3 b_h. The proton on the oxygen dangling into interlayer space is acidic and therefore can participate in ion exchange reactions. An extensive amount of research has been performed on the ion exchange properties of α–ZrP [28-38]. Using the traditional way for determining total exchange capacity of an ion exchange material, titration with a NaCl + NaOH mixture, resulted in an assay of 6.6 mEqu g^{-1} total ion exchange capacity for α–ZrP. It was also found that the exchange behavior was highly dependent on the crystallinity of the ZrP [38]. Highly crystalline samples form distinct exchange phases, while less crystalline samples form single solid solutions. The size of the cation also plays a large role. Changing the counter cation in the MOH + MCl mixture from Li^+, to Na^+, to K^+, to Rb^+, to Cs^+ the crystalline α–ZrP shows a sieving effect [25], where Rb^+ and Cs^+ react solely with the surface exchange sites. The smaller ions, however, are able to penetrate the layers and react with all the exchange sites [32, 35]. The sieving properties are not observed with the less crystalline samples, but an order of selectivity is observed as follows: $Li^+ < Na^+ < K^+ < Rb^+ < Cs^+$ [39]. Another interesting property of

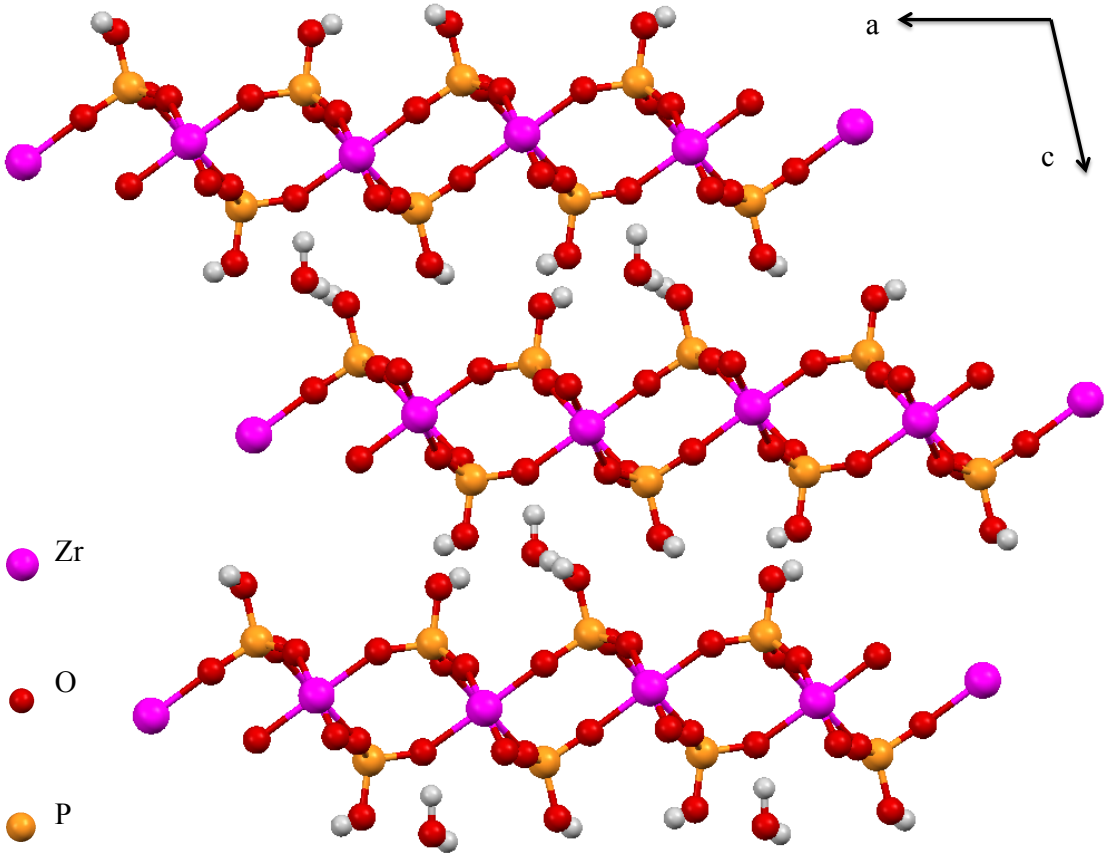

Figure 2: Alpha-zirconium phosphate looking down the b-axis.

ZrP, is that the layers can be exfoliated, presumably into single nano-sheets suspended in solution [40-42]. Over the last fifty years study of α–ZrP and its less crystalline forms have expanded to encompass a large variety of research foci, one of which is organic derivatization, to which we turn our focus.

The phenyl phosphonate derivative was synthesized in 1978 [43] by reacting phenyl phosphonic acid and zirconyl chloride, and the structure was later solved in 1993 [44]. It was found to form a layered compound, much like α–ZrP, with an interlayer spacing of 14.8 Å. The phenyl groups take the place of the dangling –OH group and form a bilayer within the interlayer space. Aryl bisphosphonate Zr^{4+} compounds were later synthesized to form a pillaring of the metal layers [45, 46]. The pillaring of the layers not only holds them together, preventing them from being exfoliated, but holds them apart, leading to the potential of microporosity.

Mixed derivatives have also been synthesized by the addition of a second ligand into the layer [46, 47]. These ligands have potential to add functionality to materials and affect both their physical and chemical properties. First, if a small ligand, such as methylphosphonate or phosphite is used to space the aryl diphosphonates, the physical property of microporosity can be created in these materials. On the other hand, chemically active spacer ligands can be used, like a carboxylate phosphonate or phosphate, and the chemical property of chelation or ion exchange can be created in materials. In many cases, incorporating chemically active spacer ligands, also leads to

formation of porosity. The Clearfield Research Group synthesized a mixed derivative from phosphate and monophenyldiphosphonate (see Figure 3) along with the biphenyl analog, where the bisphosphonate pillars are spaced by the smaller phosphate, having the ideal formula $Zr(O_6P_2(C_6H_4))_{1-x/2}(O_3POH)_x \bullet nH_2O$ [48, 49]. They both exhibited ion exchange properties, but the monophenyl derivatives displayed selectivity for the lanthanides. Their behavior towards the actinides was not previously tested, but will be one focus of this dissertation.

Using the α–ZrP layer as a basis for our model shown in Figure 3 and doing a simple calculation the interlayer distance should be ~ 9.6 Å from one metal layer to the next, being held apart by the phenyldiphosphonate pillar ligand. The α–ZrP layers have been observed to be 6.3 Å thick, so in the positions occupied by the phosphate spacer ligand there should be roughly 3.3 Å of free space between the two dangling pendant oxygens. Following the α–ZrP layer, the in-plane distance from one phosphate/phosphonate site is believed to be 5.3 Å. If the arbitrary value for $x = 0.5$ in the above formula is used and the statistically ideal conformation is obtained (shown in the bottom row of the schematic), the lateral distance from one phosphonate phosphorus to its nearest neighbor phosphonate phosphorus would be 10.6 Å. Taking into account the phenyl ring van der Waals radius of approximately 3.4 Å [50], the lateral interlayer free space would be about 7.2 Å. It should be pointed out that these calculations are established on zirconium-based materials; changing the tetravalent metal cation to tin should not dramatically affect the interlayer distance, but should have a noticeable change in the

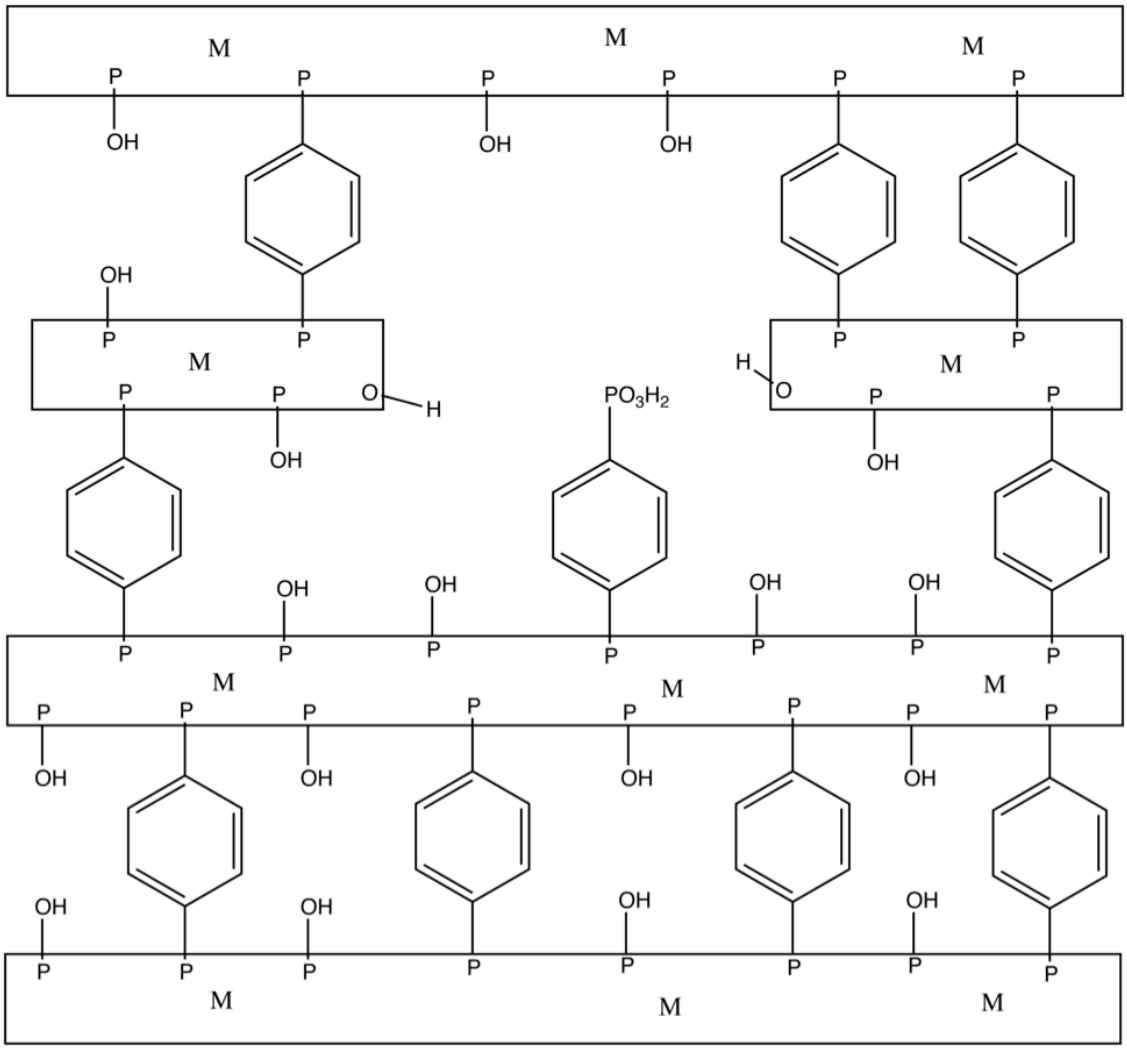

Figure 3: A schematic of how the mixed derivative of the M(IV) monophenyl-bisphosphonate phosphate may be formed.

in-plane distances, as Sn^{4+} is significantly smaller than Zr^{4+}.

Now, with all that being said there are believed to be defects in these structures, which may open up larger pores [51]. For example, there could be aggregation of like ligands, leading to hydrophobic phenyldiphosphonate rich areas in the materials, as well as hydrophilic phosphate rich portions. This would generate larger slit-like pores within the layers, with lateral free spaces well beyond 7.2 Å. Another defect you might expect is missing cations within the metal layers themselves, which would create larger pores or cavities in the material, and which could even result in a free phosphonic acid within the pores. The consequent chapters will elucidate the difficulties in describing the exact conformation and structure of the materials caused by their poorly crystalline nature; however it will be seen that the data from a variety of characterization techniques supports the proposed model, but like George Edward Pelhem Box once said, "All models are wrong but some are useful." [52] and again, "Remember that all models are wrong; the practical question is how wrong do they have to be to not be useful." [53]

1.3 Ion exchange theory

Generally, ion exchange materials can be thought of as insoluble solids that have either cations or anions that are bound in an ionic fashion. The following is an explanation of a simple binary system consisting of ions $\bar{A}^x$ and B^y, the bar above the symbol signifies

the species to be in the solid phase. The chemical equation of ion exchange is provided in Equation 1.

$$y\bar{A}^{x} + xB^{y} \longleftrightarrow yA^{x} + x\bar{B}^{y} \quad (1)$$

where x and y are the charges of the ions. From this equilibrium it can be seen that ion exchange is a charge neutral process, so for every unit charge that sorbs to the material an equivalent charge must desorb from the material in order to preserve charge balance. The ion exchange process is different from physisorption. In physisorption, the charge neutrality concerns have to be satisfied by the species being sorbed—as no ions are being released—and requires room for counter ions to accompany a charged species. Ion exchange is an equilibrium process, and so the selectivity of one ion over another can be determined for a given ion exchange material. Of course, many factors play an important role in selectivity, to name a few: the functionality of active site; pore size and structure of the material; the ion size, charge, and hydration of the ions; as well as the concentration and composition of the solution being contacted with the exchanger. In the current example the equilibrium constant can be written and calculated by Equation 2:

$$k_{B/A} = \frac{[A]^{y}[\bar{B}]^{x}}{[\bar{A}]^{y}[B]^{x}} \quad (2)$$

where the bracketed species represent the concentration of the ion in the exchange material (barred) or in solution (no bar). However, to calculate such a constant a complete understanding of the exchange materials, ions involved in the exchange process, and the solution makeup must be acquired. For our purposes, as will be seen in the subsequent chapters and as mentioned earlier, there are still some key unknowns involved with the ion exchange materials we are using, in particular the environment of the binding sites. We will use the distribution coefficient, or K_d value, to estimate the selectivity of the exchange materials in this study.

The K_d value is a measure of the distribution of the ion of interest between the solid and liquid phase at equilibrium and carries the units of mL g^{-1} (see Equation 3).

$$K_d = \frac{[\bar{B}]}{[B]} \tag{3}$$

The distribution coefficient will be discussed in more detail on Chapter II Section 2.5 and will include the explicit definition of calculating its value. However, it should be remembered that without a more rigorous understanding of the ion exchange material being investigated, you cannot directly relate the K_d value to the equilibrium constant.

For the sake of providing a thorough background, the following discussion is offered to show how the thermodynamic constant $k_{B/A}$ can be related to the empirically calculated,

non-thermodynamic K_d value (if the ion exchange material is fully described). If $[\bar{B}] << [\bar{A}]$ and $[B] << [A]$ then the concentration of ion A in the solid phase ($[\bar{A}]$) only changes slightly, and can be assumed to be constant and equal to the total exchange capacity, Q, of the ion exchange material ($[\bar{A}] \sim$ Q). Rearranging Equation 2 and substituting it into Equation 3, we can write Equation 4 as follows:

$$K_d^{\ x} \approx k_{B/A} \frac{[Q]^y}{[A]^y} \tag{4}$$

By taking the logarithm of Equation 4, a mechanism of exchange behavior can be derived and gives Equation 5.

$$\log K_d = \left(\frac{1}{x}\right)\log(k_{B/A} Q^y) - \left(\frac{y}{x}\right)\log[A] \tag{5}$$

Ideally, plotting log K_d as a function of log [A] should result in a straight line having a slope – (y/x). However, this is only accurate when $[\bar{B}] << [\bar{A}]$ and $[B] << [A]$. As [B] increases the log-log plot may become nonlinear or the slope may deviate away from –(y/x) [54, 55].

1.4 Scope of study

The scope of this study is a combination of several fields including, materials science, solution chemistry, and analytical chemistry, broadly falling within the category of inorganic chemistry. Chapter II provides a concise description of all the experimental details of the work covered in this dissertation and is mainly analytical in focus, but touches on some solution chemistry. Chapters III and IV present the results of the materials science portion of the research and describe the development of the zirconium- and tin-based materials, respectively. The main focus of Chapter V is investigation of the ion exchange properties of these inorganic organic hybrid ion exchange materials, and includes elements of all three: materials science, solution chemistry, and analytical chemistry. The primary concern is to develop materials that have utility as separations media in harsh environments, such as those found in the nuclear fuel cycle. Chapter VI offers some general conclusions and identifies some areas where this research could be expanded and improved.

CHAPTER II

MATERIALS AND METHODS*

2.1 Introduction

The focus, nature, and aim of this research allows for a consolidation of experimental procedures, methods, analysis, and approach. This chapter is designed to provide a clear and detailed account of the materials, experimental synthetic procedures, characterization methods, and scientific approaches including K_d value determination, along with any other experimental information that is required for a complete understanding of the experiments contained in the subsequent chapters of this dissertation, with the aim to deconvolute the narrative of the successive chapters. Except in specific instances, where a discussion of the experimental details is required to allow the reader a full understanding of the points being addressed, step by step experimental details will be limited to this chapter. This will neccessitate only brief mention of such

* Part of this chapter is reprinted with permission from "Pillared metal(IV) phosphate-phosphonate extraction of actinides." Burns, J. D.; Clearfield, A.; Borkowski, M.; and Reed, D. T. *Radiochim. Acta*, **2012**, *100* (6), 381-387 by Copyright 2012 Oldenbourg Wissenschaftsverlag; "Separation of oxidized americium from lanthanides by use of pillared metal(IV) phosphate-phosphonate hybrid materials." Burns, J. D.; Borkowski, M.; Clearfield, A.; and Reed, D. T. *Radiochim Acta*, **in press**, by Copyright 2013 Oldenbourg Wissenschaftsverlag; and ""Separation of americium from curium by oxidation and ion exchange." Burns, J. D.; Clearfield, A.; Shehee, T. C.; and Hobbs, D. T. 2012, 84 (16), 6930-6932 by Copyright 2012 American Chemical Society.

content in the subsequent chapters where needed, along with the occasional cross-references in the narrative back to specific sections in this chapter.

This chapter is divided into four major sections for clarity. First, a detailed description of the starting materials is laid out (Section 2.2). Second, an account of the different synthetic approaches of the M(IV) inorganic organic hybrid ion exchange materials is provided (Section 2.3); including the bulk synthesis of the four representative ion exchange materials, which were rigorously investigated for their utility in ion exchange processes pertaining to the nuclear fuel cycle. Next, a complete account of the characterization methods is given (Section 2.4). Lastly, the experimental methods for determining ion affinity is discussed (Section 2.5), including a discussion on how the K_d value is calculated along with solution details for both the single and mixed ion studies.

2.2 Materials

Neodymium chloride hexahydrate (99.9%, $NdCl_3 \cdot 6H_2O$), calcium nitrate tetrahydrate (99%, $Ca(NO_3)_2 \cdot 4H_2O$), lithium hydroxide monohydrate (98%, $LiOH \cdot H_2O$), concentrated perchloric acid (Trace Metal Grade, $HClO_4$), stannic chloride pentahydrate (98%, $SnCl_4 \cdot 5H_2O$), and zirconyl chloride octahydrate (98%, $ZrOCl_2 \cdot 8H_2O$) were purchased from Aldrich; nickel(II) nitrate hexahydrate (Reagent Grade, $Ni(NO_3)_2 \cdot 6H_2O$) was purchased from Matheson Coleman & Bell Manufacturing; tribasic potassium phosphate (≥98%, K_3PO_4) and sodium persulfate (≥98, $Na_2S_2O_8$) were purchased from

Sigma-Aldrich; samarium nitrate hexahydrate (99.9%, $Sm(NO_3)_3 \bullet 6H_2O$) and ytterbium nitrate hydrate ($Yb(NO_3)_3 \bullet xH_2O$, 99.9%) were purchased from Alfa; phosphoric acid (ACS Grade, H_3PO_4) and sodium nitrate (99%, $NaNO_3$) were purchased from EMD; sodium persulfate (98+%, $Na_2S_2O_8$) was purchased from Acros; tribasic sodium phosphate dodecahydrate (99%, $Na_3PO_4 \bullet 12H_2O$), calcium hypochlorite (65% or 71% available chloride, $Ca(OCl)_2$), strontium nitrate (ACS Grade, $Sr(NO_3)_2$), lanthanum nitrate hexahydrate (Reagent Grade, $La(NO_3)_3 \bullet 6H_2O$), as well as concentrated nitric acid (ACS or Optima Trace Metal Grade, HNO_3) were purchased from Fisher; cesium nitrate (99.9%, $CsNO_3$) was purchased from Strem Chemicals, Inc.; neodymium nitrate hexahydrate (99.9%, $Nd(NO_3)_3 \bullet 6H_2O$) and holmium nitrate hydrate (99.9%, $Ho(NO_3)_3 \bullet xH_2O$) were purchased from K and K Laboratories Inc.; and hydrofluoric acid (Trace Metal Grade, HF) was purchased from Fluka Analytical; all the above chemicals were used without further purification. 1,4-monophenyldiphosphonic acid ($H_2O_3PC_6H_4PO_3H_2$) was prepared by a modified Hirao [56-59] Pd cross-coupling reaction. The Teflon-lined steel pressure reaction vessels used in the hydrothermal experiments were manufactured by the Department of Chemistry's machine shop at Texas A&M University. Neptunium–237 (^{237}Np), plutonium–242 (^{242}Pu), and americium–243 (^{243}Am) were taken from stock solutions on hand at Los Alamos National Laboratory-Carlsbad Operations (LANL-CO). The NpO_2^+ was purified by solvent extraction to remove accumulated daughter products with equal volumes of 0.1 M HNO_3 and 0.1 M bis-(2-ethylhexyl) phosphoric acid (HDEHP) and used immediately. The neptunyl(V) ion (95+% purity by mass as ^{237}Np) is retained in the aqueous phase,

while the other species generated by redox and decay processes are removed in the organic phase. Plutonium(IV) (99.9+% purity by mass as, ^{242}Pu) was synthesized by air-oxidizing Pu(III) that was formed by heating to dryness in concentrated hydrobromic acid. The PuO_2^{2+} (99.9+% purity by mass as ^{242}Pu) was synthesized by fuming in concentrated perchloric acid to near dryness. The ^{243}Am (99.9% purity by activity, ^{243}Am) stock contained a europium carrier in 10 μg/mL quantities. For the trivalent studies, Am was passed through an Eichrom-TRU (2 mL, 100-150 μm) column in 2 M HNO_3 to remove any impurities. The trivalent Am is retained, while impurities in other valences are washed from the column. The Am was then stripped from the column with 4 M HCl. The Am used in the pentavalent oxidation state experiments was taken to near dryness in $HClO_4$ and then oxidized by the procedure described in a later chapter (see Chapter V Section 5.5.3). The final pH of all the solutions were adjusted to ~ 2 with NaOH and HNO_3. In all cases, the oxidation state was confirmed by absorption spectrometry (Varian Cary 5000 spectrometer equipped with a temperature controller). Liquid scintillation counting (LSC, Beckman Coulter, LS 6500 scintillation counter) was used to measure Np, Pu, and Am activities. In the case of Am(V) the LSC counting window was restricted to 700–800 eV. Inductively coupled plasma mass spectrometry (ICP-MS, Agilent ICP-MS 7500ce mass spectrometer) was used to determine the concentration of Nd and Am, as well as relative Eu concentrations, in the mixed ion studies at LANL-CO. Americium–241 (^{241}Am) was recovered from fuel reprocessing at the Savannah River Site and the curium–244 (^{244}Cm) recovered from a gamma and X-ray primary source on hand at Savannah River National Laboratory (SRNL). The

dissolution of the ^{244}Cm source was as follows, the source holder was first placed in 8 M HNO_3 to dissolve the beryllium window, followed by the Cm source being dissolved in HF. After four days of dissolution in HF the sample was taken to dryness and brought back up into solution with 6 M HNO_3. Both the Am^{3+} and Cm^{3+} were each purified by passing them through an Eichrom DGA-branched column in ~ 1 M HNO_3, and then eluted off the column with 0.01 M HNO_3. The final purity of ^{244}Cm was determined by alpha pulse height analysis (α–PHA) by Savannah River National Laboratory analytical division, where the ^{241}Am purity was determined by spectroscopic techniques (Avantes AvaSpec–2048TEC Thermo-electric cooled Fiber Optic Spectrometer coupled with a 100 cm World Precision Instruments LWCC liquid waveguide capillary cell with an Ocean Optics LS-1 tungsten halogen lamp. The data were collected and compiled in the AveSpec-USB2 7.2 software in absorbance mode). The americium-curium solution was made as follows, by first oxidizing the Am^{3+} to AmO_2^+ using the method discussed in Chapter V Section 5.5.3 and then adding the appropriate amount of Cm^{3+} to give equal amounts of Am and Cm, the solution was then diluted with ultrapure water from a MilliQ Elements system (Millipore, Billerica, MA) to 30 mL and the pH was adjusted with HNO_3 and NaOH to bring the working stock to a pH ~ 2.

2.3 M(IV) hybrid materials synthesis

2.3.1 Materials development synthesis

2.3.1.1 Synthesis temperature

The general procedure was to dissolve a mixture containing the 0.5 mmol (0.1190 g) of $C_6H_4(PO_3H_2)_2$ and 1 mmol (66.7 μL) of H_3PO_4 in 3 mL of distilled deionized (ddi) H_2O in a Teflon liner. A solution of 0.5 M [M(IV)] in ddi H_2O was prepared ahead of time. While stirring, 1 mmol (2 mL) of the metal solution was added to the phosphate/phosphonate mixture drop wise. Immediately after the metal addition the stir bar was removed and the reaction vessels were sealed and placed in constant temperature ovens at 80, 105, 120, 140, 160, 180, or 200 ºC for 4 days. After cooling, the white solids were washed copiously with ddi H_2O by vacuum filtration and dried at 60–80 ºC overnight. Once dried the resulting products were white pastes that were easily ground into powders. The analytical data are included in the narrative in subsequent chapters, as they directly relate to the discussion.

2.3.1.2 Synthesis time

The general procedure was to dissolve a mixture containing the 0.5 mmol (0.1190 g) of $C_6H_4(PO_3H_2)_2$ and 1 mmol (66.7 μL) of H_3PO_4 in 3 mL of ddi H_2O in a Teflon liner. A

solution of 0.5 M [Zr(IV)] in ddi H_2O was prepared ahead of time. While stirring, 1 mmol (2 mL) of the zirconium solution was added to the phosphate/phosphonate mixture drop wise. Immediately after the metal addition the stir bar was removed and the reaction vessels were sealed and placed in constant temperature ovens at 120 ºC for 0, 2, 4, and 10 days. After cooling, the white solids were washed copiously with ddi H_2O by vacuum filtration and dried at 60–80 ºC overnight. The reaction heated for 0 days was left on the bench top for an hour after the addition of Zr before filtering and washing. Once dried, the resulting products were white pastes that were easily ground into powders. The analytical data is included in the narrative in subsequent chapters, as they directly relate to the discussion.

2.3.1.3 Pillar-to-spacer ligand ratio

The general procedure was to dissolve a mixture containing the appropriate amounts of $C_6H_4(PO_3H_2)_2$ and of H_3PO_4 in 3 mL of ddi H_2O in a Teflon liner (see Table 1). A solution of 0.5 M [M(IV)] in ddi H_2O was prepared ahead of time. While stirring, 1 mmol (2 mL) of the metal solution was added to the phosphate/phosphonate mixture drop wise. Immediately after the metal addition the stir bar was removed and the reaction vessel was sealed and placed in a constant temperature oven at the desired temperature for the desired time. After cooling, the white solid was washed copiously with ddi H_2O by vacuum filtration and dried at 60–80 ºC overnight. The resulting products were white pastes that ground easily into white powders. For the reactions

based on zirconium, the P:S ratios chosen to be investigated were 1:2, 1:4, 1:6, and 1:8. For the reactions based on tin, the ratios were adjusted, because the surface areas were undesirable at higher ratios (see Chapter IV Section 4.3 for a complete discussion). The P:S ratios that were used for the Sn–hybrids were:1:1, 1:2, 1:4, and 1:6.

Table 1: Starting amount of the pillar (P) and spacer (S) ligands to synthesize a material with an ideal formula of $M(C_6H_4(PO_3)_2)_{1-x/2}(O_4PH)_x \bullet nH_2O$.

P:S	x =	$C_6H_4(PO_3H_2)_2$ (mmol)	$C_6H_4(PO_3H_2)_2$ (g)	H_3PO_4 (mmol)	H_3PO_4 (µL)
1:1	0.66	0.66	0.1570	0.66	44.0
1:2	1.00	0.50	0.1190	1.00	66.7
1:4	1.33	0.33	0.0785	1.33	88.7
1:6	1.50	0.25	0.0595	1.50	100.0
1:8	1.60	0.20	0.0476	1.60	106.7

2.3.1.4 Phosphate source of the spacer ligand

The general procedure was to dissolve a mixture containing the 0.5 mmol (0.1190 g) of $C_6H_4(PO_3H_2)_2$ and 1 mmol (0.3799 g) of $Na_3PO_4 \bullet 12H_2O$ or 1 mmol (0.2123 g) K_3PO_4 in 3 mL of ddi H_2O in a Teflon liner. The Li_3PO_4 was made *in situ* by first dissolving 3 mmol (0.1675 g) of $LiOH \bullet H_2O$ and then adding 1 mmol (66.7 µL) H_3PO_4. A solution of 0.5 M [Zr(IV)] in ddi H_2O was prepared ahead of time. While stirring, 1 mmol (2 mL) of the metal solution was added to the phosphate/phosphonate mixture drop wise. Immediately after the metal addition the stir bar was removed and the reaction vessels were sealed and placed in a constant temperature oven at 120 ºC for 4 days. After

cooling, the white solids were washed copiously with ddi H_2O by vacuum filtration and dried at 60–80 ºC overnight. The resulting products were white pastes that ground easily into powders. The analytical data is included in the narrative in subsequent sections.

2.3.2 Bulk synthesis

The materials were synthesized on a ~ 3 g scale under hydrothermal conditions having the ideal formula of $M(O_3PC_6H_4PO_3)_{1-x/2}(O_3PO\mathit{A})_x \bullet nH_2O$, where M = Zr or Sn, *A* = H or Na. The general procedure was to dissolve a mixture of 5 mmol (1.1897 g) of pillar and 10 mmol (0.667 mL) of spacer in 25 mL of ddi H_2O in the Teflon liner. While stirring, 10 mmol (20 mL) of either the $ZrOCl_2 \bullet 8H_2O$ or $SnCl_4 \bullet 5H_2O$ solution was added drop wise. Immediately after the metal addition the stir bar was removed and Teflon liner was sealed in a steel reaction vessel and placed in a constant temperature oven at 120–140 ºC for 4–5 days. After cooling, the white solid was washed copiously with ddi H_2O by vacuum filtration and dried at 60–80 ºC for 24 hours. The resulting product was a white paste that ground easily into a powder. The reactions that started from Na_3PO_4 were carried out using the same method, but the sodium phosphate was substituted for the phosphoric acid. The reaction conditions are summarized in Table 2 and the characterization is summarized in Table 3.

2.4 M(IV) hybrid materials characterization

Thermogravimetric analysis (TGA) was performed on a TA Instruments TGA Q-500 at a heating rate of 10 ºC min^{-1} under 10/90 N_2/airflow. X-ray powder diffraction patterns were collected on a Bruker AXS Advanced diffractometer with CuKα radiation (λ=1.5418 Å) operated at 40 mA and 40 kV by the step-scan method (step 0.009º, time 0.1 s). N_2 sorption-desorption isotherms were obtained on a Quantachrome Autosorb-6 instrument at liquid nitrogen temperature. The samples were dried in an oven at 140–150 ºC and then degassed under vacuum at 120 ºC for 21–24 hrs on a Quantachrome degasser. Surface areas were derived from the isotherms by the BET and *t*-plot methods. All isotherm and hysteresis classifications are in line with the IUPAC standards. Elemental analysis for carbon and hydrogen (C and H) was performed by Atlantic Microlab, Inc. or Robertson Microlit Laboratories. For zirconium and phosphorus ratios, samples were digested in HF and Anderson Analytical determined relative amounts by inductively coupled plasma atomic emission spectroscopy (ICP-AES). Zr/Sn:P:Na:Cl ratios were also determined on a four spectrometer Cameca SX50 electron microprobe with an accelerating voltage of 15 kV at a beam current of either 10 or 20 nA. All quantitative work employed wavelength-dispersive spectrometers (WDS). Analyses were carried out after standardization using very well characterized compounds or pure elements. Qualitative analyses (spectra) were obtained with an Imix Princeton Gamma Tech (PGT) energy dispersive system (EDS) using a thin-window detector. Solid state Magic Angle Spinning (MAS) Nuclear Magnetic Resonance (NMR) spectra were

Table 2: Reaction conditions and yields of the four bulk syntheses.

Sample	Time	Reactants	Yield (g)	%Yield
H–Zr–hybrid	4 days	$ZrOCl_2 \cdot 8H_2O + 0.5\ C_6H_4P_2O_6H_4 + H_3PO_4$	3.093	93.5%
Na–Zr–hybrid	4 days	$ZrOCl_2 \cdot 8H_2O + 0.5\ C_6H_4P_2O_6H_4 + Na_3PO_4$	3.199	97.7%
H–Sn–hybrid	5 days	$SnCl_4 \cdot 5H_2O + 0.5\ C_6H_4P_2O_6H_4 + H_3PO_4$	3.338	98.1%
Na–Sn–hybrid	4 days	$SnCl_4 \cdot 5H_2O + 0.5\ C_6H_4P_2O_6H_4 + Na_3PO_4$	3.510	99.3%

Table 3: Elemental analysis along with the derived formulas of the four bulk syntheses.

							%C		%H	
Sample	Formula	FW	M	:P	:Na	:Cl	Calc.	Exp.	Calc.	Exp.
H–Zr–hybrid	$Zr(O_6P_2C_6H_4)_{0.49}(O_3POH)_{0.86}(OH)_{0.32} \cdot 2.0H_2O$	331	1.0	1.8	-	-	10.7	10.6	2.2	2.3
Na–Zr–hybrid	$Zr(O_6P_2C_6H_4)_{0.43}(O_3POH)_{0.18}(O_3PONa)_{0.66}(OH)_{0.60} \cdot 1.7H_2O$	328	1.0	1.7	0.66	-	9.5	9.5	1.8	2.1
H–Sn–hybrid	$Sn(O_6P_2C_6H_4)_{0.44}(O_3POH)_{0.80}(OH)_{0.53}Cl_{0.11} \cdot 1.6H_2O$	340	1.0	1.7	-	0.11	9.3	9.4	1.9	2.3
Na–Sn–hybrid	$Sn(O_6P_2C_6H_4)_{0.44}(O_3POH)_{0.74}(O_3PONa)_{0.05}(OH)_{0.66} \cdot 2.4H_2O$	353	1.0	1.7	0.05	-	9.0	9.3	2.3	2.4

obtained on a Bruker Avance-400 Solids NMR spectrometer operating at 10 kHz for ^{31}P and 6 kHz for ^{23}Na, 0 ppm H_3PO_4 and 0 ppm NaCl were used as external chemical shift standards for ^{31}P and ^{23}Na, respectively. Scanning electron microscopy (SEM) images were acquired on a JEOL JSM-7500F (FE-SEM). Samples were prepared using copper grids from Ted Pella.

2.5 Ion affinity determination

The K_d values, as mentioned in the previous chapter, are good measures of ion affinity for ion exchange materials and in all cases were calculated as follows:

$$K_d = \frac{C_I - C_{Eq}}{C_{Eq}} \bullet \frac{V}{m} \tag{6}$$

where C_I is the initial ion concentration in solution, C_{Eq} is the equilibrium ion concentration in solution, V is the volume of metal solution, and m is the mass of exchanger. The average of three repetitions of the experiment was used to estimate the K_d values and the uncertainty was calculated from the confidence interval at a 70% confidence level of those three measurements. For radioactive isotopes, where activity was used to measure the ion concentration, A_I and A_{Eq} were substituted for C_I and C_{Eq} respectively.

2.5.1 Groups 1, 2, d-block and lanthanides

The general procedure of the uptake studies was to shake 20 mg of sample with 5-10 mL of 1×10^{-4} M [M^{n+}] in HNO_3 at pH 3 (unless otherwise stated) for 1–2 days on an orbital shaker. After shaking, samples were allowed to settle and aliquots were removed and diluted with 2% ICP grade HNO_3 to reduce the [M^{n+}] to match the sensitivity of the instrument. Metal concentrations before (C_I) and after (C_{Eq}) contact with the exchanger were determined by ICP-MS on a PerkinElmer SCIEX ICP Mass Spectrometer ELAN DRC II in standard mode and K_d values were determined by Equation 6.

Mixed ion studies were performed in order to directly observe the selectivity of the material. Intergroup separations were performed by introducing the following cation pairs, Cs^+ and Nd^{3+}, Sr^{2+} and Nd^{3+}, and Ni^{2+} and Nd^{3+}, to create three sets of competitive reactions; the solution details are reported in Table 4. Intragroup separations were performed with several lanthanides (Nd, Sm, Ho, and Yb) in competition. The intragroup separations were run as a function of pH and the solution details are presented in Table 5. Metal concentrations before (C_I) and after (C_{Eq}) contact with the ion exchangers were determined by ICP-MS on Perkin Elmer ICP-Mass Spectometer NexION 300D.

Table 4: Solution details for the intergroup lanthanide group 1, group 2 or transition metal separations studies. Metal concentration in M estimated error < 1%.

Solution	Concentration (M)	pH
Nd^{3+} / Cs^{+}	2.80×10^{-5} / 4.95×10^{-5}	2
Nd^{3+} / Sr^{2+}	2.83×10^{-5} / 2.75×10^{-5}	2
Nd^{3+} / Ni^{2+}	2.89×10^{-5} / 5.32×10^{-5}	2

Table 5: Solution details for the intragroup lanthanide separations studies. Metal concentration in M estimated error < 1%.

pH	$[Nd^{3+}]$	$[Sm^{3+}]$	$[Ho^{3+}]$	$[Yb^{3+}]$
1.0	1.95×10^{-5}	2.07×10^{-5}	2.15×10^{-5}	2.35×10^{-5}
1.5	2.01×10^{-5}	2.12×10^{-5}	2.21×10^{-5}	2.41×10^{-5}
2.0	2.04×10^{-5}	2.14×10^{-5}	2.22×10^{-5}	2.43×10^{-5}
2.5	2.06×10^{-5}	2.17×10^{-5}	2.25×10^{-5}	2.45×10^{-5}
3.0	1.98×10^{-5}	2.07×10^{-5}	2.18×10^{-5}	2.39×10^{-5}

2.5.2 Actinides

The general procedure of An uptake studies was to shake 20 mg of exchanger with 2 mL of an An solution (see Table 6 for An solution details) for 24 hours. After shaking, the samples were allowed to settle and 100 µL aliquots were passed through a 100 kDa filter by centrifugation at 13,000 RPM for 15 minutes. 50 µL of each filtrate were then added to 3 mL of LSC cocktail and counted for 10-60 minutes. The Na-Zr-hybrid reduced the actinide concentration so low that its cocktails were spiked with 100 µL and 200 µL for Pu^{4+} and PuO_2^{2+} experiments, respectively. Actinide activity was measured by liquid scintillation counting (LSC, Beckman Coulter, LS 6500 scintillation counter) before (A_I)

and after (A_{Eq}) contact with the exchanger and the K_d values were calculated using Equation 6.

Table 6: Actinide solutions, estimated error < 1%.

Solution	Concentration (M)	pH	Z_{eff}
$[AmO_2]^+$ / Eu^{3+}	9.04×10^{-6} / 2.55×10^{-6}	1.99	2.1 [60] / 3.0 [61]
$[NpO_2]^+$	3.24×10^{-4}	2.11	2.2 [62]
Am^{3+} / Eu^{3+}	4.72×10^{-6} / 1.33×10^{-6}	2.00	2.9 [61] / 3.0 [61]
$[PuO_2]^{2+}$	1.02×10^{-4}	1.94	2.9 [62]
Pu^{4+}	4.19×10^{-5}	1.79	4.0 [61]

Details for the mixed ion lanthanide-actinide systems are summarized in Table 7. 100 μL of a solution containing the appropriate amount of Nd^{3+} was added to the reaction mixture to keep the volume constant at 2 mL (for Am(V) experiments the neodymium solution contained OCl^-). The samples were then allowed to shake for another 24 h and sampled following the same procedure. The Nd and Eu concentrations were determined by ICP-MS (Agilent ICP-MS 7500ce mass spectrometer), the Np and Pu concentrations were determined for both by LSC counting only, and the Am concentrations were determined by both ICP-MS as well as LSC counting and were in good agreement. K_d values were calculated using Equation 6 and separation factors (SF) were determined by directly taking the ratio of the K_d values.

Table 7: Actinide/lanthanide solutions, estimated error < 1%.

Solution	Concentration (M)	pH	Z_{eff}
$[AmO_2]^+/Nd^{3+}/Eu^{3+}$	$8.59\times10^{-6}/1.23\times10^{-4}/2.43\times10^{-6}$	1.99	2.1 [60]/2.9 [61]/3.0 [61]
$[NpO_2]^+ / Nd^{3+}$	$3.08 \times 10^{-4} / 1.00 \times 10^{-4}$	2.11	2.2 [62] / 2.9 [61]
$[PuO_2]^{2+} / Nd^{3+}$	$9.70 \times 10^{-5} / 1.00 \times 10^{-3}$	1.94	2.9 [62] / 2.9 [61]

The general procedure of the Am-Cm separation studies was to shake 20 mg of exchanger with 2 mL of a solution 3.8×10^{-6} M $[AmO_2^+]$ and 3.0×10^{-6} M $[Cm^{3+}]$ for 24 hours on a rotatory shaker in 15 mL HDPE centrifuge tubes. After shaking, the samples were passed through a 0.45 μm syringe filter. Samples were analyzed by α–PHA to determine percent activity for the respective actinides. K_d values were calculated from Equation 6 and SF's were determined using the ratio of the K_d values.

CHAPTER III

MATERIALS DEVELOPMENT:

ZIRCONIUM

3.1 Introduction

The way in which a material is prepared and synthesized can play a profound role on the properties of that material. Parameters such at synthesis time and temperature, as well as types and relative amounts of ligands may lead to significant changes in the total porosity, overall pore structure, and ion exchange behavior of the product. The aim of this chapter is to provide a clear discussion of four different specific areas and the effect on the properties of the zirconium based materials, these area include: 1) synthesis temperature (Section 3.2), 2) synthesis time (Section 3.3), 3) pillar-to-spacer ligand ratio (Section 3.4), and 4) phosphate source of spacer ligand (Section 3.5).

3.2 Synthesis temperature

A series of reactions were designed to determine what effect synthesis temperature has on the formation and structure of these hybrid materials. The synthetic procedure follows that of the general procedure (see Chapter II section 2.3.1.1) with synthesis temperatures spanning from 105–200 ºC and reaction time of 4 days. The X-ray powder diffraction (XRPD) patterns, presented in Figure 4, reveal the semi-crystalline nature of

Zr–hybrids, having only four broad, weak reflections in the range of 4–40º 2θ at d ~ 9.6, 4.4, 3.6 and 2.6 Å. This first reflection is believed to be the interlayer distance, corresponding to the distance of the metal layers being held apart by the diphosphonate pillar. The later three reflections are believed to be in-plane values. Upon raising the temperature to 160 ºC the Zr–hybrids begin to become multiphased as observed by XRPD, most evident in the reflections at d = 5.9 and 4.5 Å which are characteristic of zirconium phosphate, no further discussion will be made of the Zr–hybrids synthesized above 160 ºC.

The general thermal decomposition of these materials can be seen in Figure 5. There are four weight losses observed, the first loss is attributed to loosely bound water loss below 190 ºC and is ~ 11%. The next loss between 190–480 ºC is believed to be a continuous water loss from inside the pores, similar to that of a polymer and is ~ 1.5%. The next two losses of ~ 10% overlap from 480–880 ºC and are believed to be 1) the combustion of the internal organic groups and 2) condensation of phosphate groups. The total weight loss is ~ 22.5%, with the final product identified by XRPD was ZrP_2O_7. If the TGA plots are normalized to neglect water loss, which can be done by taking the first derivative of the weight loss (see Figure 6), very little difference can be identified in signals resulting from the combustion and condensation reactions taking place up to the synthesis temperature of 145 ºC; however at 160 ºC there is a shift towards a higher content of PO_4 moiety which may indicate the beginnings of a phase transition towards a

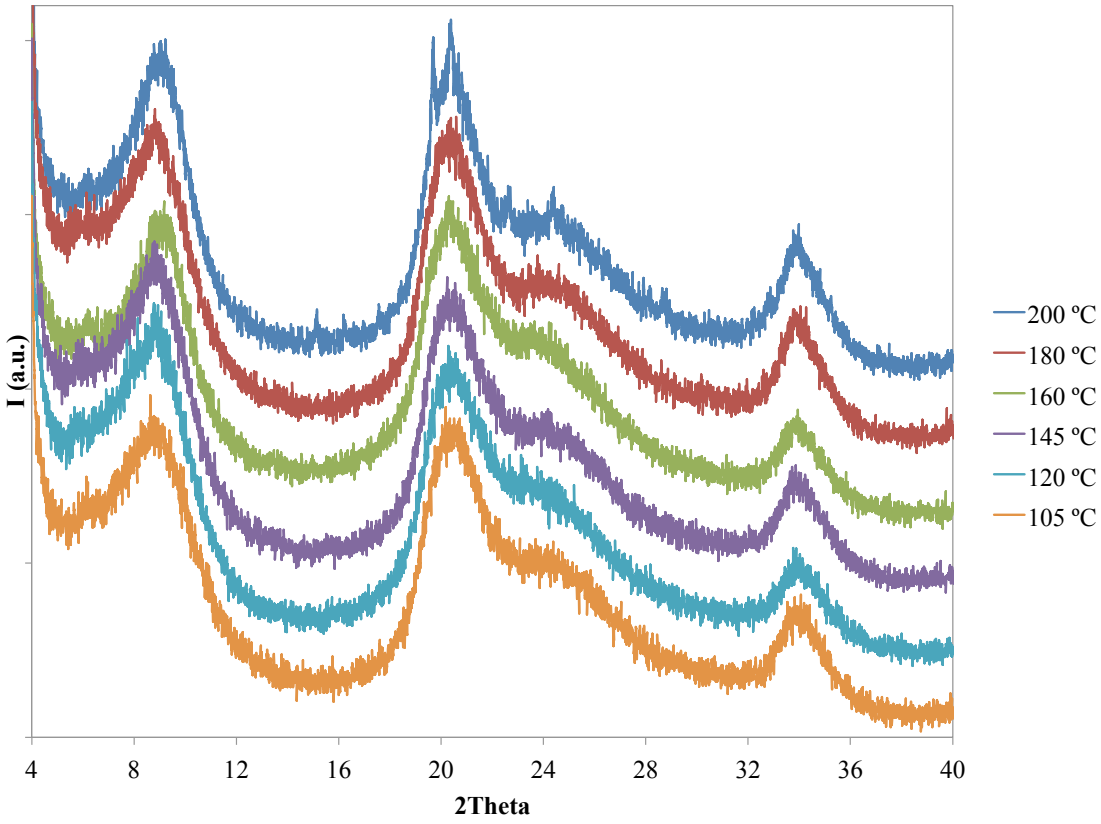

Figure 4: XRPD patterns of Zr–hybrid materials synthesized at 105–200 ºC.

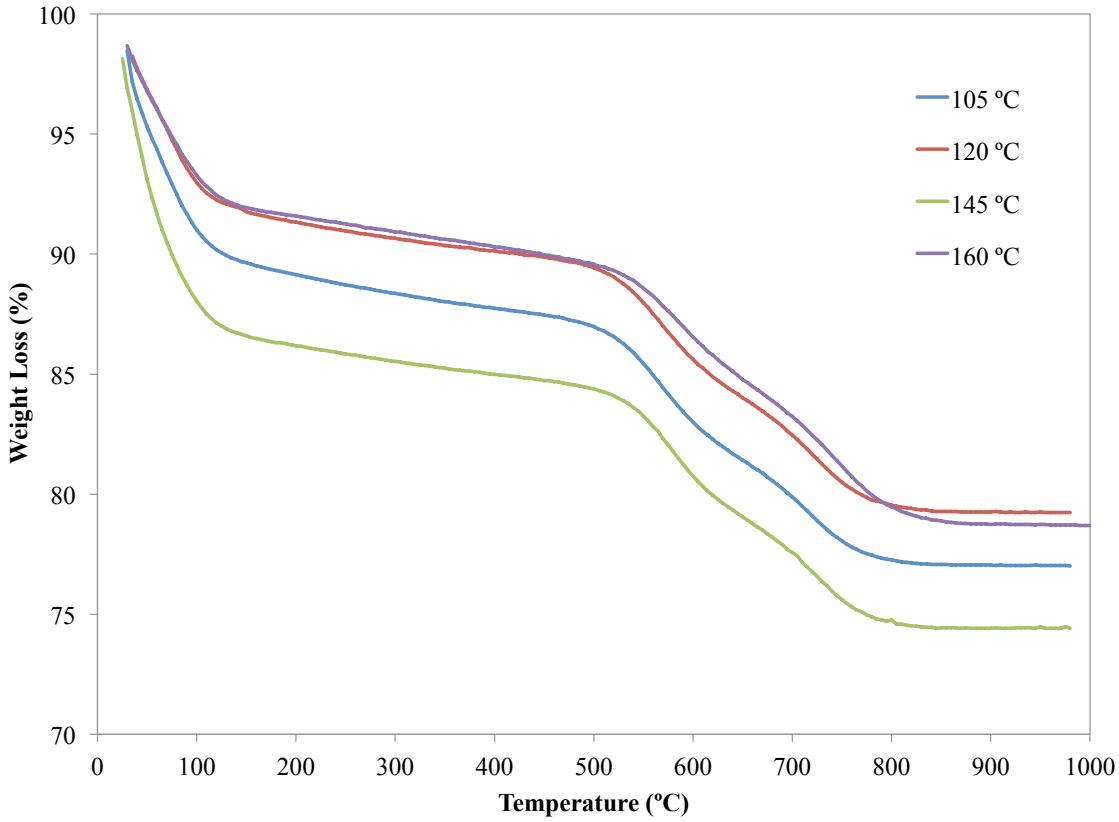

Figure 5: Thermogravimetric analysis of the Zr–hybrids synthesized at 105–160 ºC.

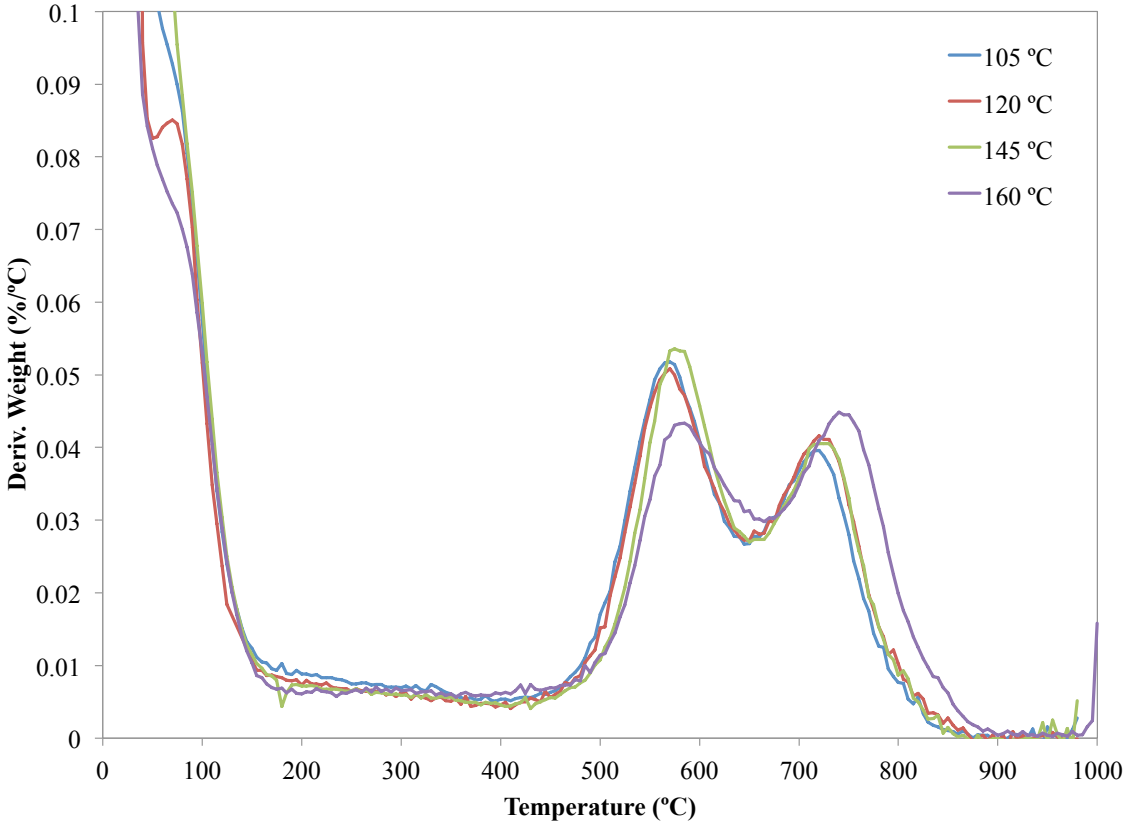

Figure 6: 1st derivative of the TGA signals for the Zr–hybrid synthesized at 105–160 ºC.

multiphased system as in the in the case when the reaction temperature is above 160 ºC. It is therefore believed that there is very little difference in chemical composition in the resultant material on increasing the synthesis temperature from 105–145 ºC.

Comparing the TGA results with the element analysis, as summarized by Table 8, it can be seen that the actual molecular formula is within experimental error of the ideal formula provided. The yields were 85% and above in all cases.

The N_2 sorption isotherms for the Zr–hybrids can be generally characterized as a modified Type II isotherm (see Figure 7). All materials contain a small H4 hysteresis loop, which indicates a major combination of slit-like micropores to the total surface area. The other major contribution of porosity, which originates from mesopores, is believed to be generated from the "house of cards" arrangement [51, 63]. The "house of cards" arrangement can be described as an aggregation of small platelet particles in a dissordered fashion to create a large distribution of mesopores and can be visualized in Figure 8. The calculated values of both the total surface area and percent microporosity, BET and *t*-plot method respectively, are summarized in Table 9. The total surface area appears to subtly decrease with an increase of temperature, this is most likely due to an increase in particle size. It is well understood that the particle size of α–ZrP correlates directly with synthesis temperature [64], and it is reasonable to believe the same phenomenon is taking place in our system. All conjecture aside, it is clear that low

Table 8: Molecular formula determination and percent yield calculation based on the TGA, ICP-AES and elemental analysis for the Zr–hybrid materials as a function of synthesis temperature, estimated error < 5%.

Synthesis Temperature	Formula	FW	Zr:P	%C		%H		Yield (g)	% Yield[a]
				Calc	Exp	Calc	Exp		
105 ºC	$Zr(O_6P_2C_6H_4)_{0.5}(O_3POH)\bullet 1.7H_2O$	331.0	1:1.9	10.9	10.2	2.7	2.2	0.288	95%
120 ºC	$Zr(O_6P_2C_6H_4)_{0.5}(O_3POH)\bullet 1.8H_2O$	334.9	1:1.9	10.8	10.7	2.7	1.7	0.287	93%
145 ºC	$Zr(O_6P_2C_6H_4)_{0.5}(O_3POH)\bullet 2.3H_2O$	343.5	1:1.9	10.5	10.8	2.6	1.8	0.271	86%
160 ºC	$Zr(O_6P_2C_6H_4)_{0.5}(O_3POH)\bullet 1.5H_2O$	330.4	1:2.0	10.9	10.3	2.7	1.8	0.260	85%

a: Based on starting amount of Zr.

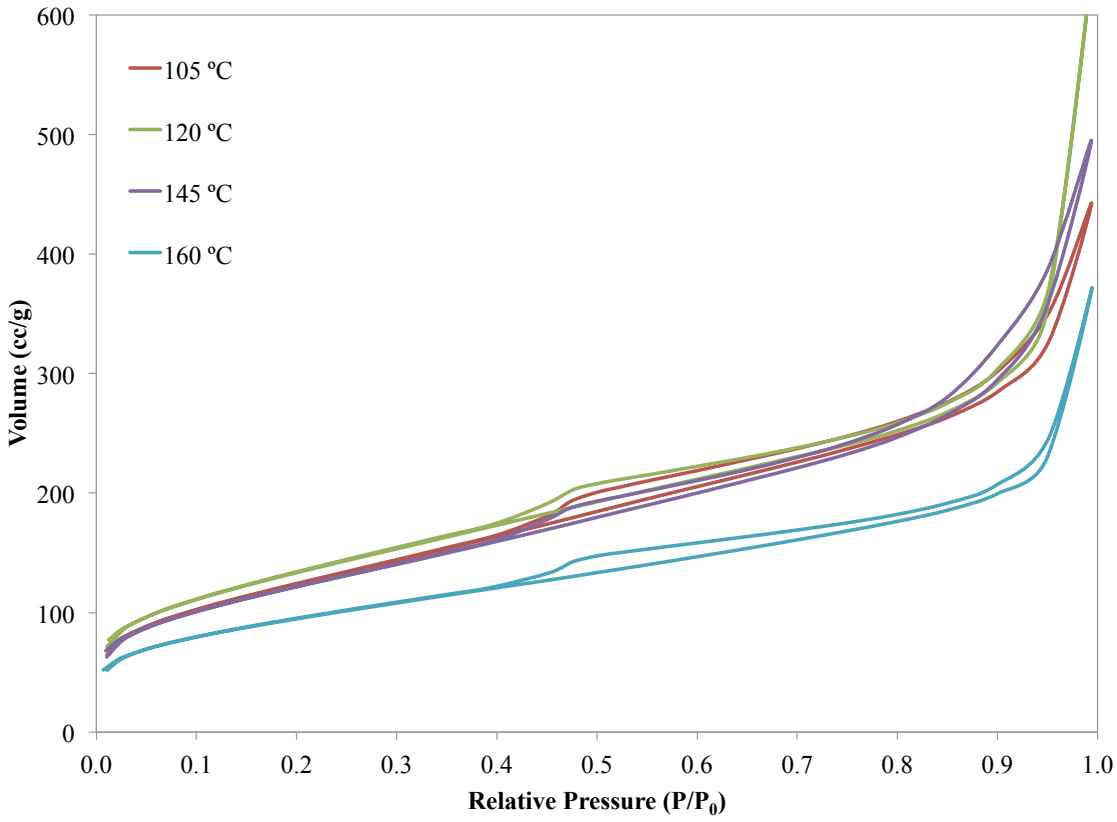

Figure 7: N_2 sorption isotherms of Zr–hybrids synthesized at 105–160 ºC.

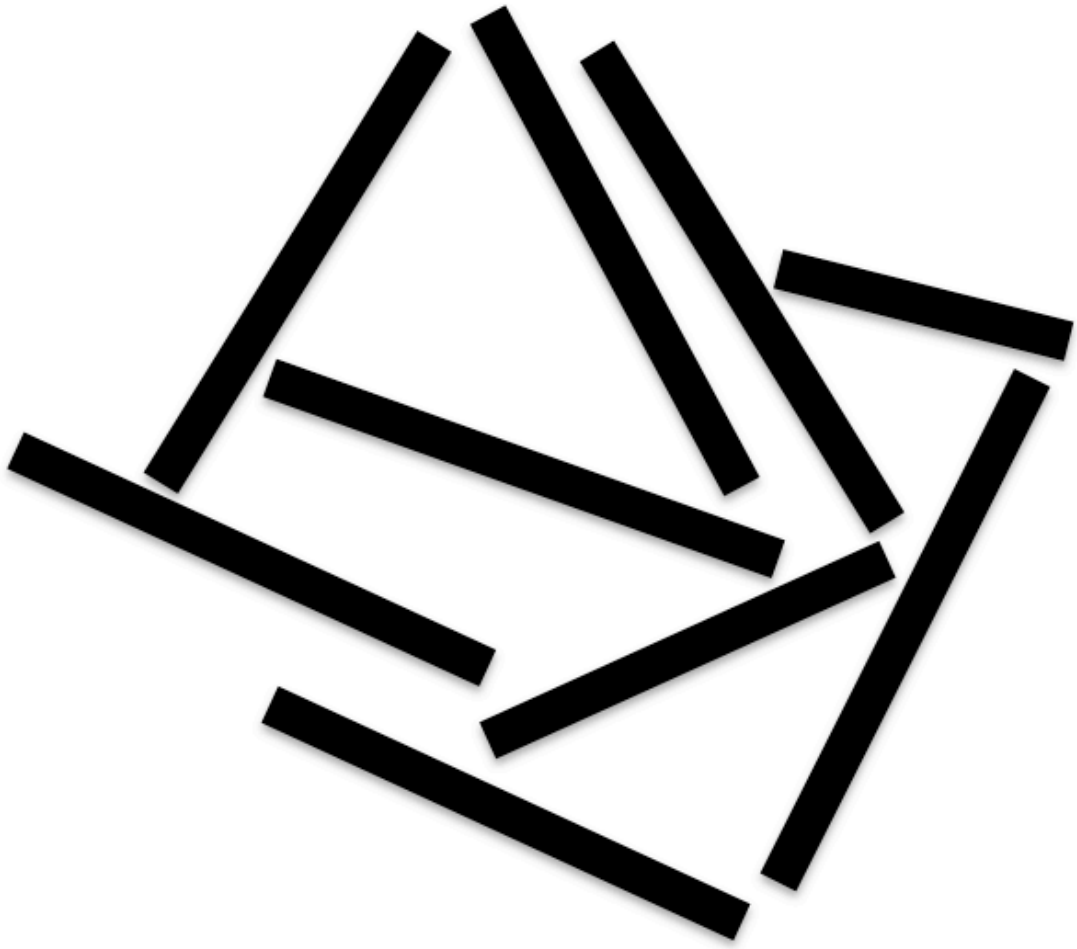

Figure 8: Model of the “house of cards” arrangement.

Table 9: Calculated N_2 sorption surface area for the Zr–hybrids as a function of synthesis temperature, estimated error < 10%.

Synthetic Temperature	Total Surface Area (m^2/g)	Microporous (%)
105 ºC	450	56%
120 ºC	490	58%
145 ºC	440	45%
160 ºC	340	63%

temperatures provide the ideal conditions to generate a material best suited for our purposes, as the surface areas are larger.

The K_d values were observed for materials synthesized from 105–145 ºC and are provided in Table 10. There does not appear to be any change in Nd^{3+} extraction upon raising the synthesis temperature from 105 to 145 ºC and therefore, no benefit to increasing the synthesis temperature above 120 ºC as it relates to the affinity of Nd^{3+}.

Table 10: Nd^{3+} affinity as a function of synthesis temperature, reported in K_d.

Synthesis Temperature	K_d values ($mL\ g^{-1}$)
105 ºC	92,000 ± 22,000
120 ºC	100,000 ± 49,000
145 ºC	77,000 ± 24,000

It can be seen from the above data that the synthesis temperature of 120 ºC provides the most advantageous materials for our purposes, providing the largest surface area with ≥ 58% originating from micropores, without making large sacrifices in crystallinity or material composition. That is to say, if a marked improvement in crystallinity would

have been observed at higher temperatures, there may have been reason to increase the scope of the research and investigate other properties such as the effect of crystallinity on ion exchange kinetics like was performed on other inorganic ion exchange materials [10] or an investigation of selectivity as a function of crystallinity. As it stands, very little to no improvement was seen in crystallinity with elevated synthesis temperature, preventing any study that necessitated crystallinity to be a variable. From these results all future materials were synthesized at 120 ºC unless otherwise stated.

3.3 Synthesis time

Next, we were interested in investigating if the percent microporosity could be increased in the Zr–hybrid materials by simply extending the reaction time, and in turn increasing the Nd^{3+} affinity. To probe this, materials were heated for 0, 2, 4, and 10 days at 120 ºC. When examined by XRPD, the patterns show that there is a minimum time required to make the semi-crystalline product (see Figure 9). The product of no heating (0 days) was a completely amorphous material, but the products of 2, 4 and 10 days at 120 ºC show very similar diffraction patterns to those discussed in the previous section, with the same semi-crystalline reflections with d-spacings of ~ 9.6, 4.4, 3.6 and 2.6 Å.

The thermal decomposition plots are very similar to those of the synthesis temperature experiments, having generally the same weight loss with the only real difference being that of water loss (see Figure 10 and Figure 11). The material that was not heated does

behave differently, having only one major weight loss other than water at ~ 500 ºC with a large tail that extends to 1000 ºC. The amorphous character of the product that was not heated is emphasized in the TGA showing a much broader range of condensation of the –POH moieties, and will not be investigated further.

The nitrogen sorption isotherms of these Zr–hybrids are also similar to the synthesis temperature experiments, and are presented in Figure 12. The isotherms for these materials are again Type II with H4 hysteresis loops. Table 11 summarizes the total surface area as determined by BET and the percent micropore as determined by *t*-plot method. There is little difference in the total surface area of the materials and within error they are essentially the same. The percent microporosity appears to be directly correlated to the heating time. Thus it appears that the mesopores tend to anneal out of the structure with increased time at temperature.

Table 11: Calculated N_2 sorption surface area for the Zr–hybrids as a function of reaction time, estimated error < 10%.

Reaction Time	Total Surface Area ($m^2\ g^{-1}$)	Microporous (%)
2 days	470	51%
4 days	490	58%
10 days	480	73%

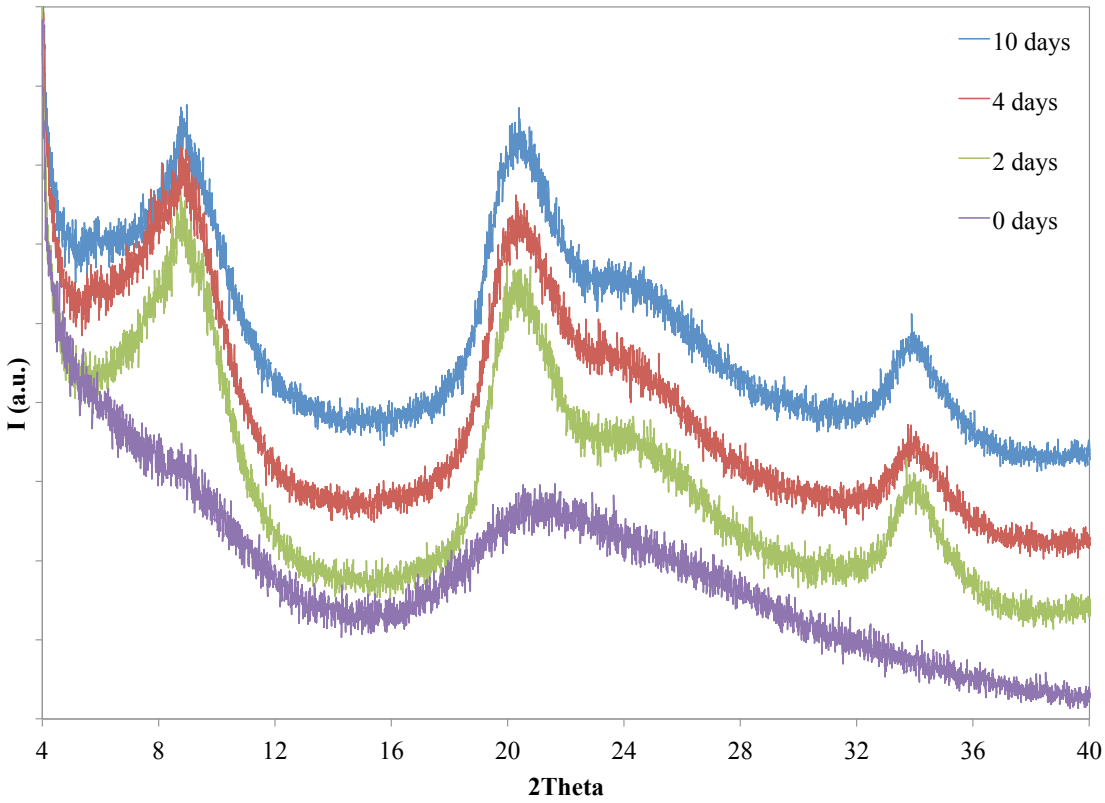

Figure 9: XRPD patterns of Zr–hybrids heated for 0–10 days at 120 ºC.

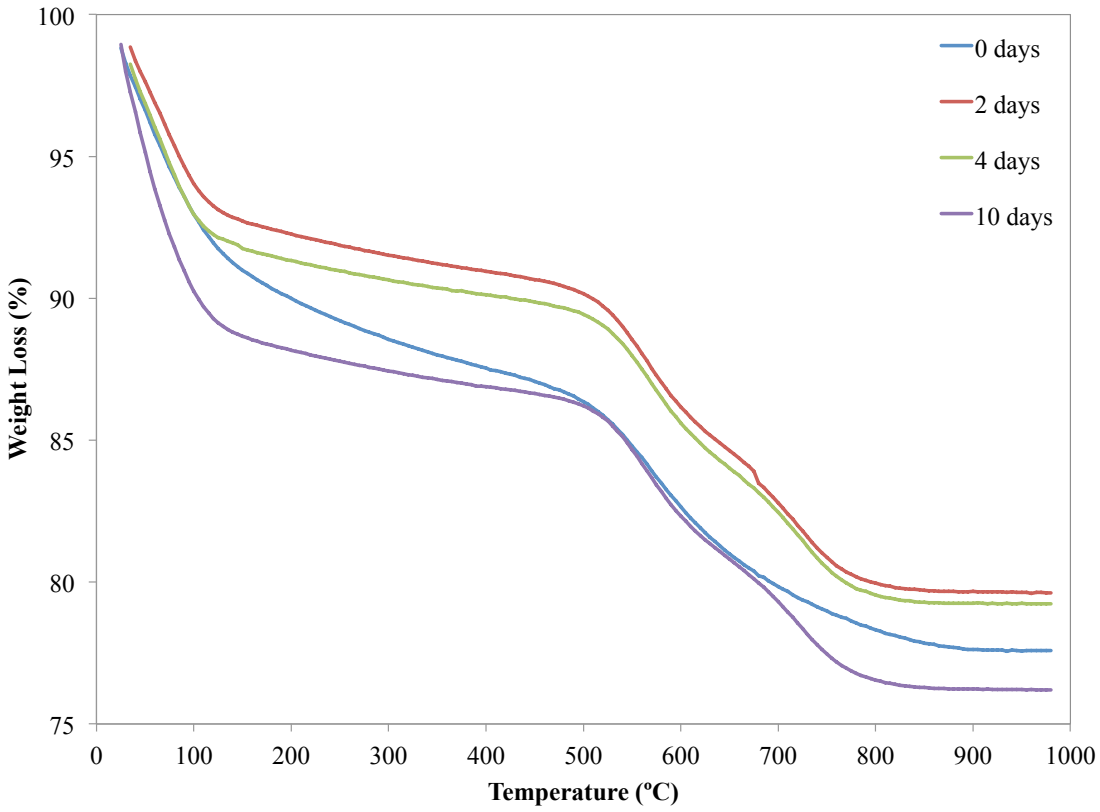

Figure 10: Thermal decomposition of Zr–hybrids heated for 0–10 days at 120 ºC.

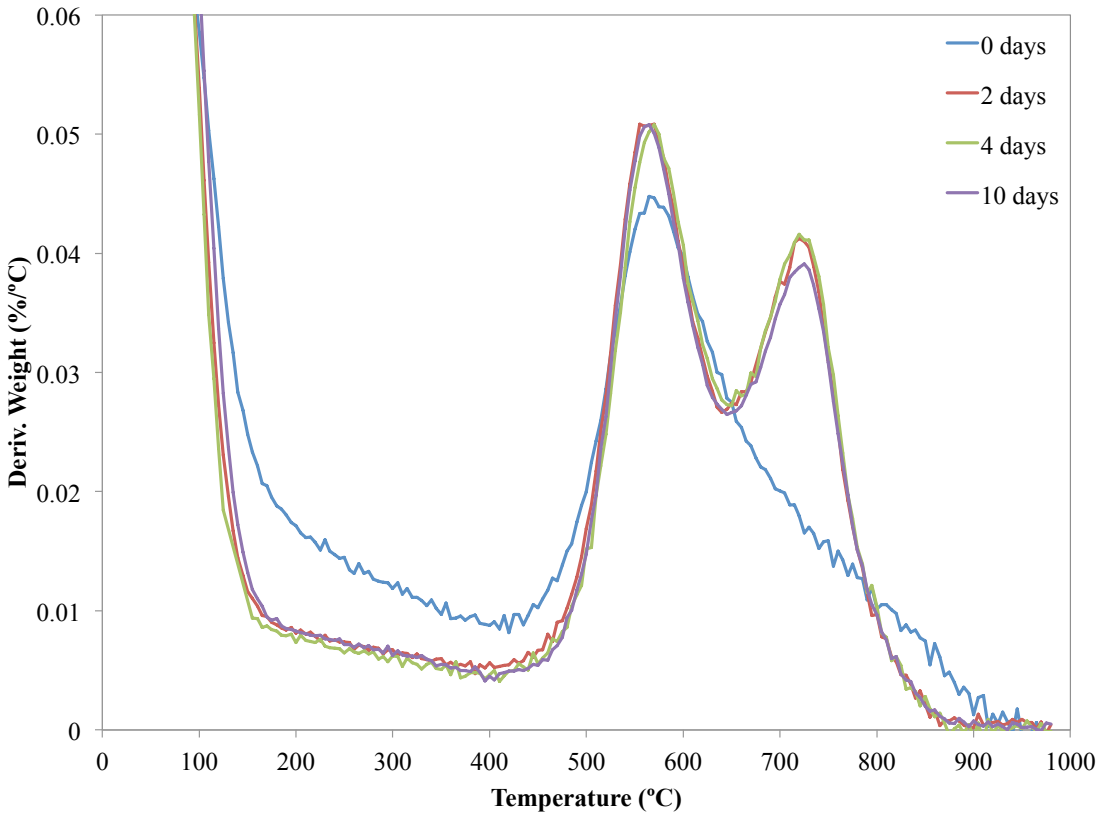

Figure 11: 1st derivative of the TGA of Zr–hybrids heated from 0–10 days at 120 ºC.

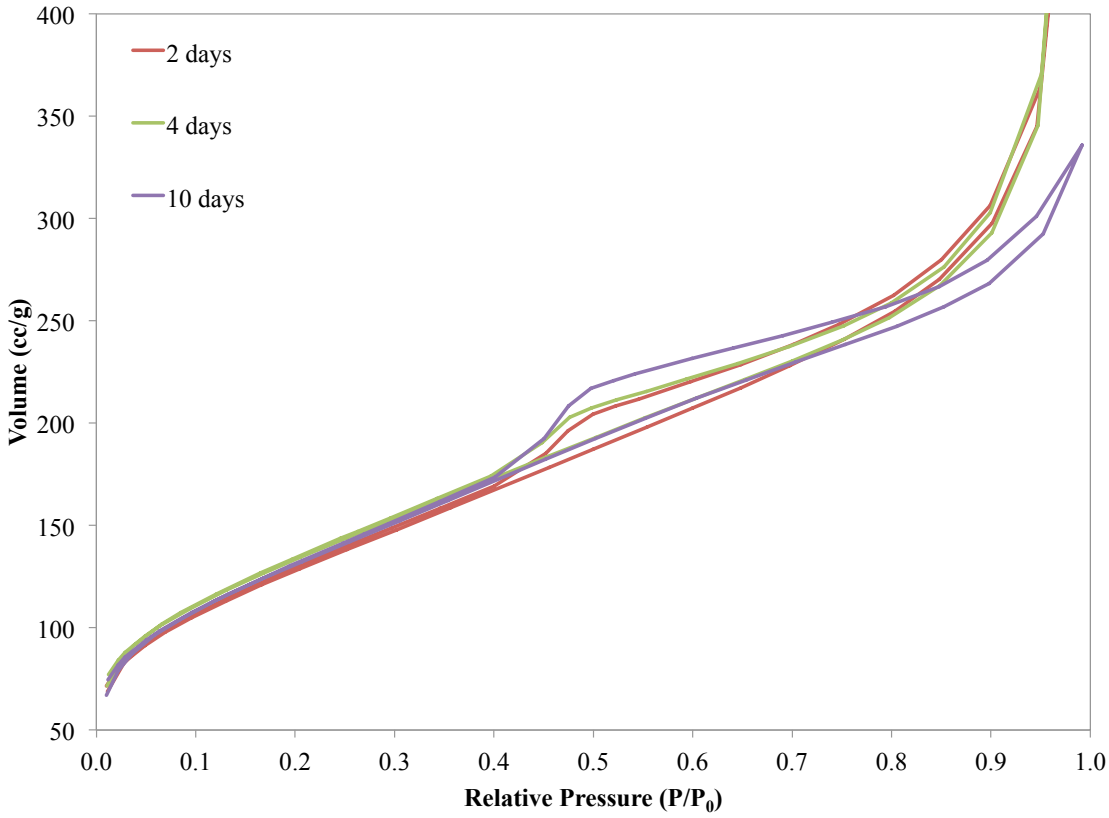

Figure 12: N_2 sorption isotherms of Zr–hybrids heated for 2–10 days at 120 ºC.

The Nd^{3+} K_d values for reaction times of 2, 4, and 10 days are presented in Table 12. At this point it is worth pointing out the K_d values observed from the synthesis temperature studies seem to be much lower than in the synthesis time studies. The large difference is mostly an artifact of the calculation, i.e. a K_d value of 77,000 mL g^{-1} represents >99% of the Nd^{3+} being removed from solution, so the denominator is very small leading to large changes in K_d from small changes in C_{Eq}. There does not appear to be any correlation between reaction time and Nd^{3+} affinity.

Table 12: Nd^{3+} affinity as a function of reaction time, reported in K_d.

Reaction Time	K_d values (mL g^{-1})
2 days	350,000 ± 59,000
4 days	500,000 ± 100,000
10 days	410,000 ± 85,000

It can be seen that after two days, extending the reaction time does not affect the crystallinity or the overall composition of the material to a large extent. As expected the percent microporosity does increase with synthesis time, but this does not correlate well with the K_d values. For our purposes the reaction times will be 4–5 days unless otherwise stated.

3.4 Pillar-to-spacer ligand ratio

To this point a generic ratio of 1:2 pillar-to-spacer ligand, that is 1,4-monophenyldiphosphonate to phosphate, has been investigated. This ratio was arbitrarily selected to form an ideal material that contains two equally abundant types of phosphorous, the organophosphonate and the phosphate ion exchange active site. A different way to think about this hybrid material is to imagine a single zirconium phosphonate derivative, zirconium p-monophenyldiphosphonate, and removing half of the (i.e. every other) phenyldiphosphonates and replacing the phosphorus sites with phosphate moieties (see Figure 13). If the ion exchange behavior of this mixed derivative is similar to that of alpha zirconium phosphate (α–ZrP) the total ion exchange capacity should be 3.3 mEqu g^{-1}, exactly half of α–ZrP [65]. This loss in efficiency is acceptable, as it is balanced by a drastic increase in selectivity (this will be discussed in more detail in a later chapter). It was believed that by simply manipulating the ratio of the two ligands during synthesis, the efficiency of the material could be pushed towards that of α–ZrP without sacrificing the benefits that a balanced ratio provides. To investigate this, a series of reactions were carried out to synthesize materials with the ideal general formula of $Zr(O_3PC_6H_4PO_3)_{1-x/2}(O_3POH)_x \bullet nH_2O$ with x varying between 1.0 and 1.6 (See Chapter II Section 2.3.1.3).

The XRPD patterns of the pillar-to-spacer ratio studies are shown in Figure 14. The pure derivative, added for reference, of the p-phenyldiphosphonate shows a much more

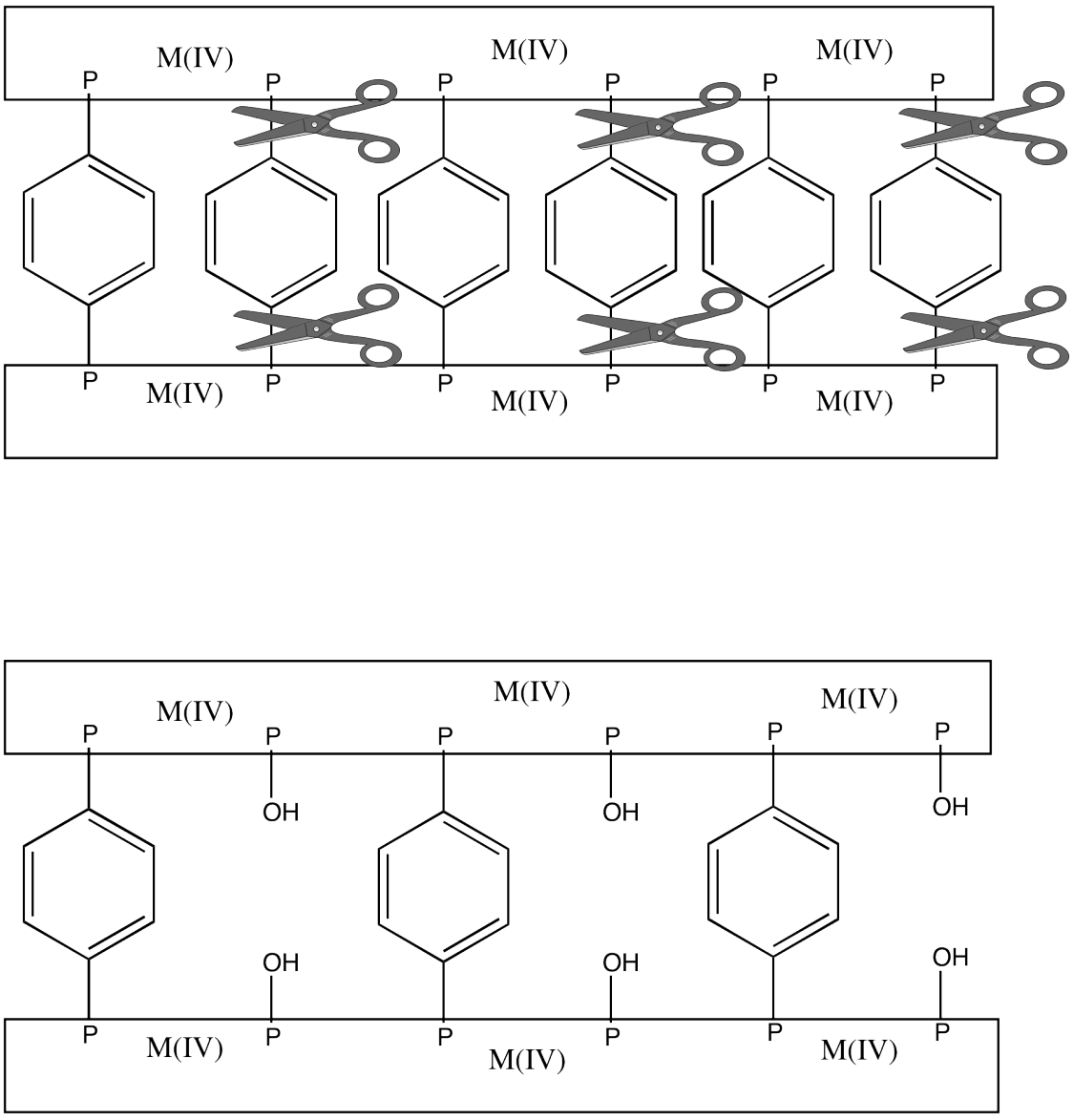

Figure 13: Visualization of converting the single derivative M(IV) material (top) to the mix derivative having a pillar-to-spacer ratio of 1:2 (bottom).

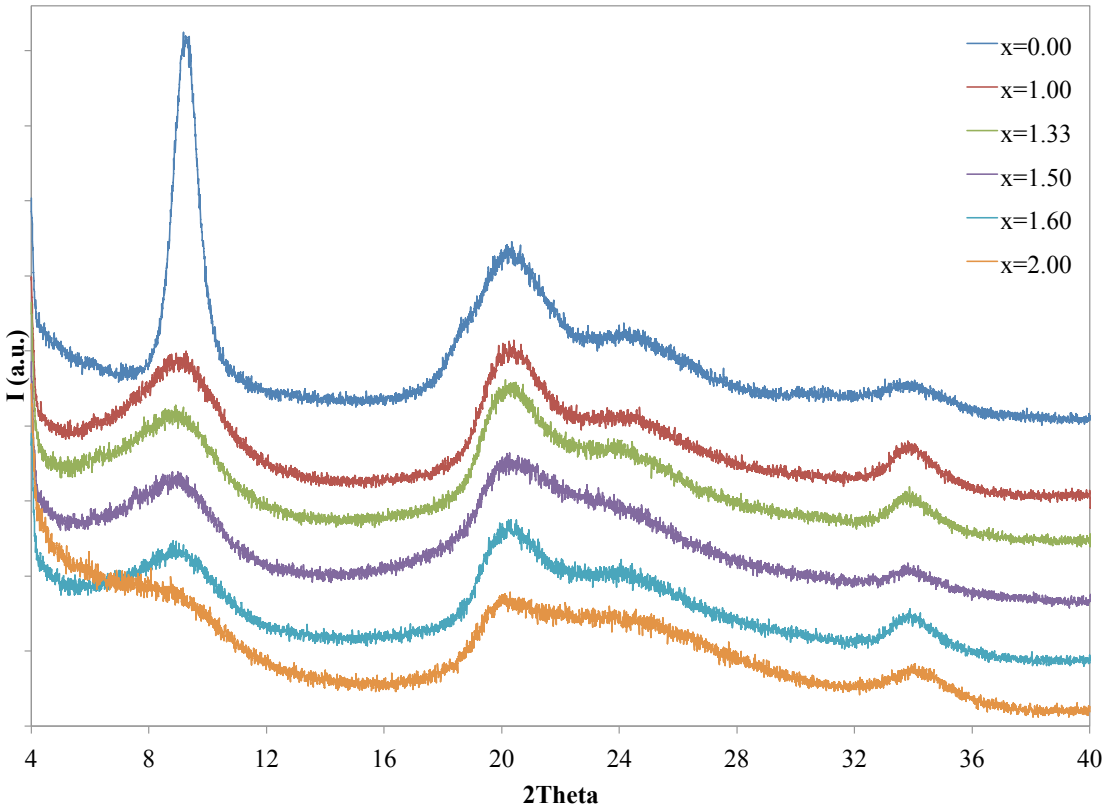

Figure 14: XRPD patterns of $Zr(O_3PC_6H_4PO_3)_{1-x/2}(O_3POH)_x$.

pronounced reflection at a d-spacing of 9.6 Å. This reaffirms our working model that this first reflection originates from the interlayer distance, as every phosphorus position must be occupied by a pillar ligand. The latter three reflections appear to be in the same position as those of the synthesis temperature and synthesis time studies that were discussed earlier. Upon addition of the phosphate ligand this first reflection quickly diminishes and the pattern remains the same until the other pure derivative is reached, in which case an amorphous zirconium phosphate gel is generated [25].

Thermogravimetric analysis lends itself as a useful tool for observing compositional changes in the materials. Figure 15 shows the first derivative of the TGA and can be interpreted as follows. When $x = 0$ the primary loss has a local maxima at 540 ºC and a shoulder that develops at 675 ºC and extends up to 900 ºC. The primary loss is undoubtedly combustion of the organics, while the second loss is surmised to be carbon burn up as well. One can imagine the ideal structure has very tightly packed pillars, of which the outer will combust first. When enough of the pillars at the edge of the particles have combusted, the layers should collapse and trap the interior pillars. If the edge of the particle collapses, a higher energy barrier may exist to allow combustion and the subsequent release of CO_2. In unison with the collapse of the layer is the pyrolysis of the metal phosphate layers to form the metal pyrophosphate, which begins formation at 650-700 ºC. At this early stage, ZrP_2O_7 is amorphous and does not begin to crystalize until 800 ºC [25]. During this phase change any trapped carbon would be allowed to evacuate the material, ideally leaving a white crystalline powder of ZrP_2O_7.

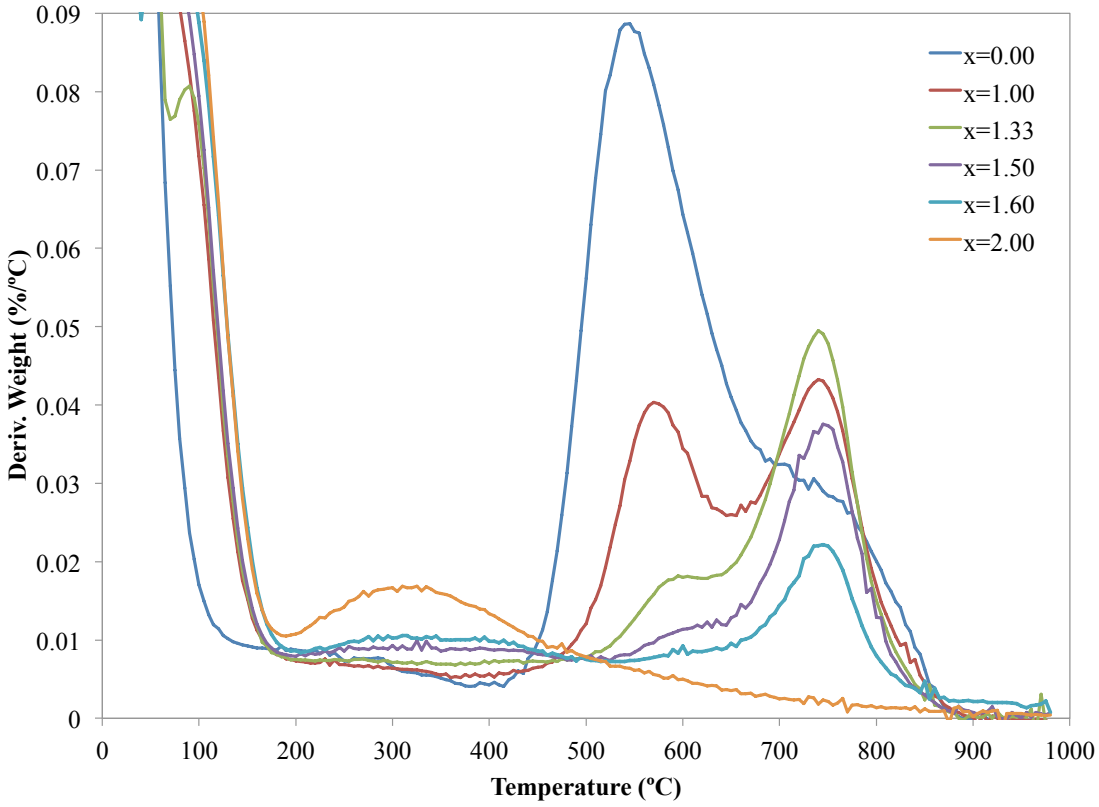

Figure 15: 1st derivative of the TGA of $Zr(O_3PC_6H_4PO_3)_{1-x/2}(O_3POH)_x$.

The mixed derivative Zr–hybrids show a nice trend in the first derivative of the thermal decomposition, with a decrease in the loss resulting from combustion and an increase in loss ensuing from condensation as *x* is changed from 1.00 to 1.60. This supports the hypothesis that more and more phosphate is being incorporated into the layers, while the amount of p-phenyldiphosphonate is decreasing. The carbon hydrogen elemental analysis is in line with the TGA and is presented in Table 13. The percent carbon decreases, as expected, upon increasing *x* from 0 to 2. This decrease corresponds to expected decrease in the percent carbon and hydrogen when compared the ideal formula of $Zr(O_3PC_6H_4PO_3)_{1-x/2}(O_3POH)_x \bullet 2H_2O$, resulting in a very close correlation between the calculated and experimental values.

Table 13: C and H percent based on elemental analysis as a function of pillar-to-spacer ratio of $Zr(O_3PC_6H_4PO_3)_{1-x/2}(O_3POH)_x$.

x =	% C		% H	
	Calc	Exp	Calc	Exp
0.00	19.9%	18.5%	2.2%	2.6%
1.00	10.6%	10.2%	2.1%	1.9%
1.33	7.1%	6.9%	2.0%	1.8%
1.50	5.5%	–	2.0%	–
1.60	4.4%	4.2%	2.0%	2.1%
2.00	0.0%	–	1.9%	–

Finally, when *x* = 2.00, the pure phosphate derivative, an initial water loss is observed up to ~ 200 ºC followed by a broad loss from 200-1,000 ºC also believed to be the pyrolysis water. This is much lower than that of the mixed derivatives at 700-800 ºC. This is

believed to be caused by the close proximity of the phosphate groups. In the zirconium phosphate, once the intercalated water is removed at 200 ºC, the layers will be sitting right on top of each other providing a very short distance of 2.0-2.5 Å allowing the proton to hop between the dangling hydroxyl moieties and split out water. The proton in the mixed derivative, initially, has a much larger energy barrier with the pillar holding the layers apart roughly 3.3 Å between hydroxyl moieties; and it is only after the combustion of the organics that the layers will be allowed to come together allowing condensation of the remaining phosphate groups.

The nitrogen sorption surface area analysis reveals an interesting trend shown in Figure 16 and Table 14. The single p-phenyldiphosphonate derivative (x = 0.00) shows a large total surface area, only exceeded when x = 1.00; however, this material has the lowest percent microporosity of those expected to exhibit porosity in the microporous regime. After x = 1.00, where the maximum in total surface area is reached, a steady decrease is observed, until it all but drops off for x = 2.00. At this time, it is believed that the microporosity of the pure phosphonate derivative is originating from defects of layer growth, as previously reported [45, 51, 66]. The defects in the layers themselves, coupled with the nanoparticle size of the material contribute to a sizable surface area.

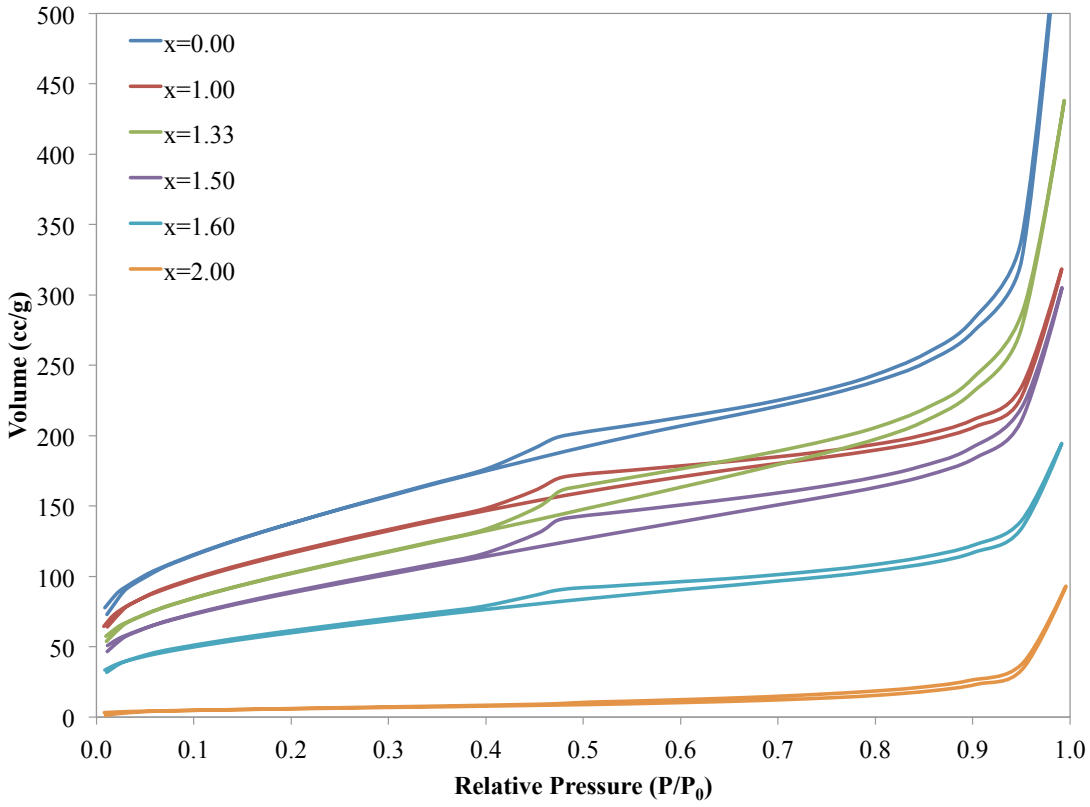

Figure 16: N_2 sorption isotherms of $Zr(O_3PC_6H_4PO_3)_{1-x/2}(O_3POH)_x$.

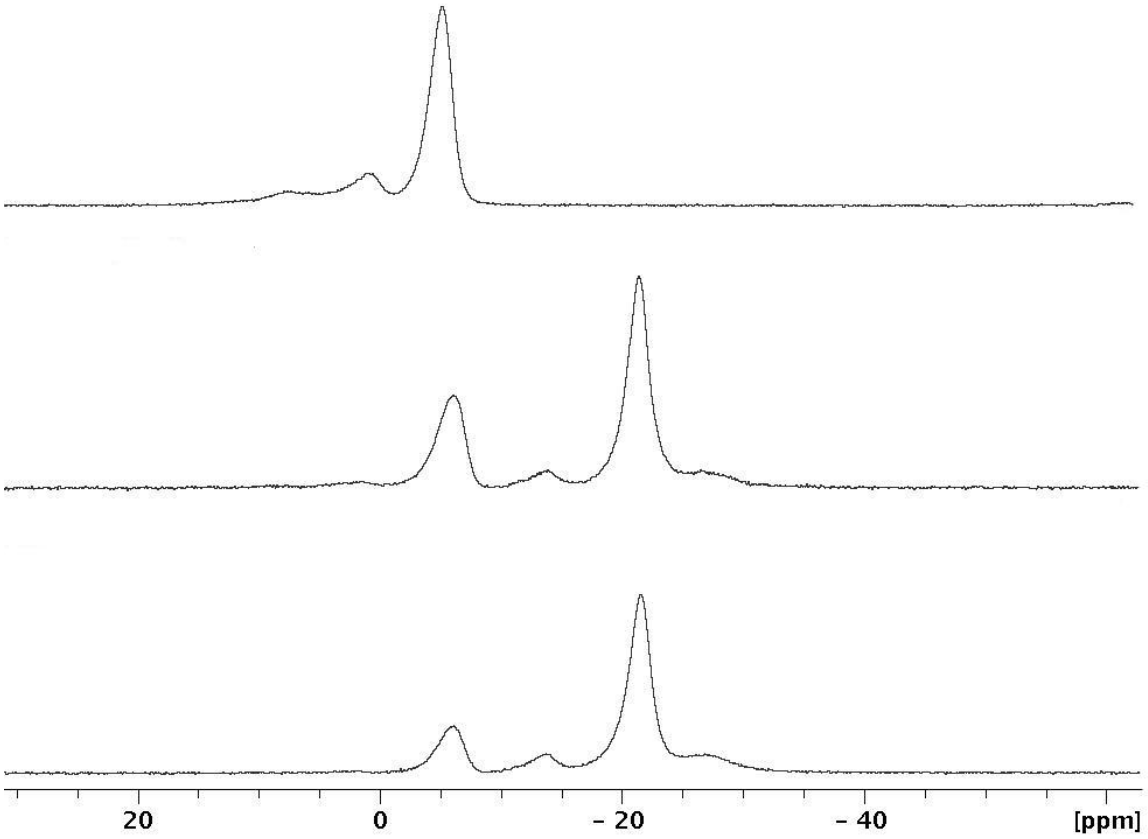

Figure 17: MAS solid-state ^{31}P NMR spectra of $Zr(O_3PC_6H_4PO_3)_{1-x/2}(O_3POH)_x$ with x = 0.00 (top), 1.33 (middle), and 1.60 (bottom).

Table 14: The calculated total surface area (BET) and percent microporosity (*t*-plot) for $Zr(O_3PC_6H_4PO_3)_{1-x/2}(O_3POH)_x$, < 10% estimated error.

x =	Total Surface Area ($m^2\ g^{-1}$)	Microporous (%)
0.00	380	52%
1.00	420	80%
1.33	370	56%
1.50	320	67%
1.60	220	69%
2.00	22	0%

Solid-state ^{31}P Magic Angle Spinning (MAS) Nuclear Magnetic Resonance (NMR) was observed for three of the six materials: x = 0.00, 1.33, and1.60 (see Figure 17). The spectra show two major phosphorus resonances at –6 ppm and –21 ppm with respect to an external phosphoric acid ^{31}P reference. The pure phosphonate derivative was expected to have only one of these resonances, but as observed in the top spectra of Figure 17 there are three lines. The major resonance at –6 ppm originates from the phosphonate fully bonded to the metal layer. The two smaller resonances at 7 and 1 ppm are believed to be caused by the defects in the metal layers mentioned earlier leading to chemically different phosphorus environments. It can easily be imagined that there are phosphonate positions that are only bonded to two, one, or no Zr^{4+} ions. However, the data suggests that only two of these defects are present, most likely the two that are present are phosphonates bonded to either two or no Zr^{4+} ions (see Figure 18). This will result in pillars that are bonded at the edge of the layer or next to a Zr^{4+} vacancy, where the third bonding oxygen does not contribute to the integrity of the structure. The second scenario, that of a free phosphonic acid, will result in a pillar completely bonding

to the metal layer at one end, and free of any metal layer bonds at the other end. The last scenario, and least likely, is that either end of the pillar is only bound to the metal layer by one oxygen, which would be easy to remove by hydrolysis.

Upon addition of the second ligand, phosphate, the emergence of several new resonances appear at –14, –21 and –27 ppm as well as the –6 ppm resonance. The two major resonances, –6 and –21 ppm, represent the phosphonate [67-70] and phosphate [68, 70-73] phosphorus atoms, respectively. Wang *et al.* [68] reported the ^{31}P chemical shifts for a staged material that contained both phosphate and phenylphosphonate to be –5.3 and–20.2 ppm, respectively; while Cabeza *et al.* [67] reported a shift of –5 ppm for the biphenylbisphosphonate derivative. While these systems are not identical to those of the current work they provide some basis for interpretation, appearing within one ppm. The minor resonances are more ambiguous in what they represent and a thorough investigation falls outside of this realm of this study; a brief comment will be made, however. These could originate from a variety of different changes in environments including: 1) differences in neighboring ligands, meaning that there is not a true statistical distribution of pillars to spacers, but rather, as previously mentioned an aggregation of like ligands; 2) differences in protonation of either the phosphates and phosphonates ligands throughout the material, caused by local incomplete bonding to the metal layer; and 3) defects in the metal layer much like was discussed previously. Unfortunately, these complications are seemingly unavoidable when dealing with an amorphous material, as is the case of our endeavor. However, they clearly are small

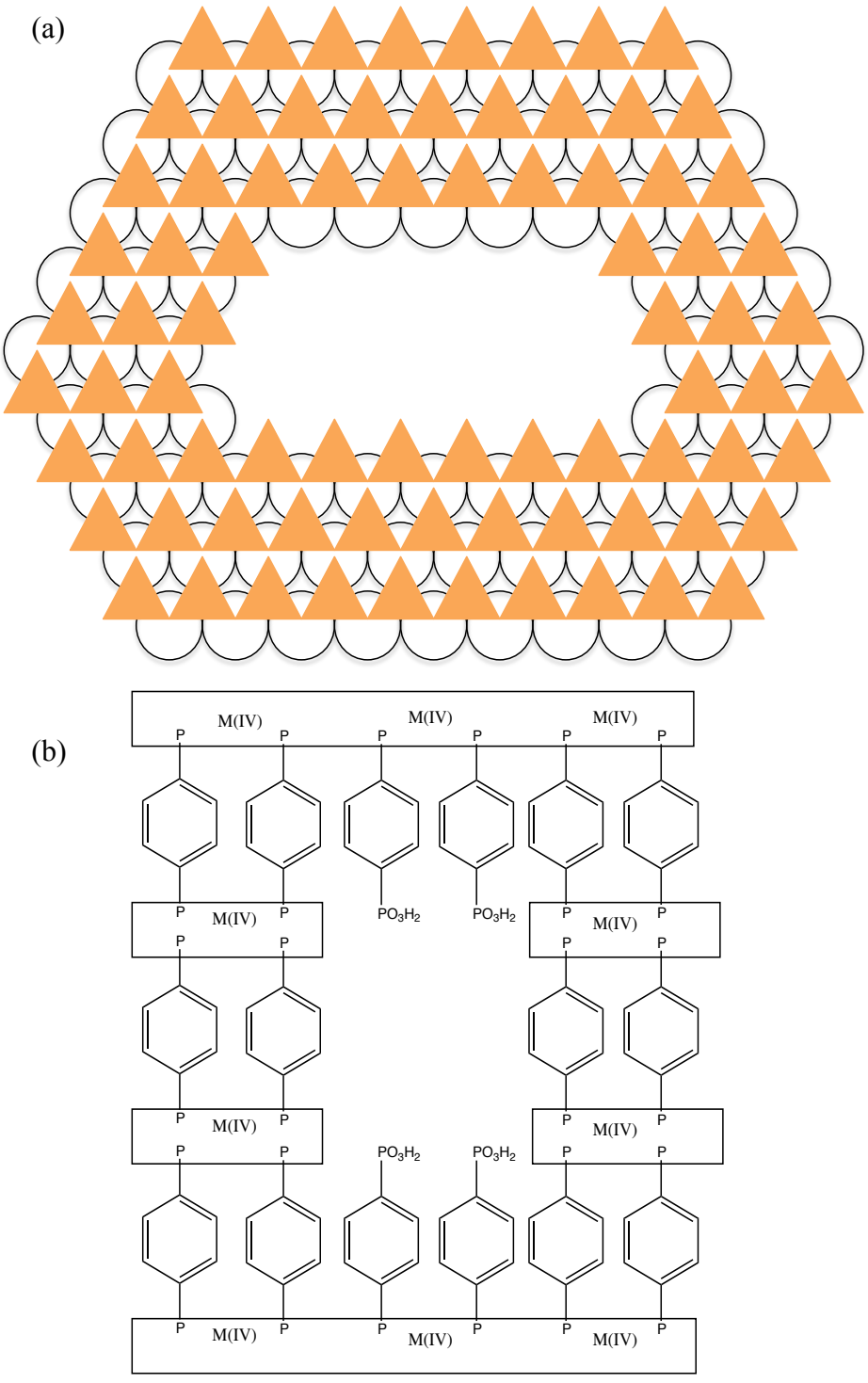

Figure 18: Proposed defects in the single phosphonate derivative: top view (a) only two oxo groups are bonding to the metal layer, circles represent Zr^{4+} ion and triangles represent the base of the phosphonate tetrahedra and side view (b) only one end of the pillar is bound to a metal layer.

contributions to the overall phosphate/phosphonate structure in the material, with the majority of phosphorus atoms being observed in the –6 and –21 ppm resonances.

By taking the integral of the resonances an estimation of the relative amounts of the different types of phosphorus are obtained. When x = 1.33, it is expected that there would be a ratio of 1:2 with respect to the phosphonate to phosphate phosphorus types, and in fact a ratio of 1:2.0 was observed. However, when x = 1.60 the expected ratio 1:4 is not reached, the observed ratio is 1:3.5. This indicates that a limit is being reached to which the phosphate is being incorporated into the material.

The K_d values for neodymium were observed from x = 1.00–1.60, and are presented in Table 15. It should be noted that these values were observed at pH ~ 2, and so they are artificially lower than the above Nd^{3+} affinity experiments (the effect of pH on the K_d values will be covered in detail in Chapter V). There is a correlation between x and Nd^{3+} affinity, as x is increased the K_d value also increases. Certainly this is a clear indication that more and more phosphate is incorporating into the material, and that indeed, like α–ZrP, that the active ion exchange sites are those of the dangling –POH moiety containing an acidic proton.

Table 15: K_d values observed for $Zr(O_3PC_6H_4PO_3)_{1-x/2}(O_3POH)_x$ at pH ~ 2.

x =	K_d values (mL g^{-1})
1.00	9,400 ± 200
1.33	15,700 ± 1090
1.50	28,700 ± 1,500
1.60	51,000 ± 1,400

3.5 Phosphate source of spacer ligand

Starting from phosphoric acid can only result in a proton as the exchangeable cation, but this may not always be desirable. Other monovalent cations were explored (see Chapter II section 2.3.1.4 for the synthetic procedure): Li^+, Na^+, and K^+. Lithium phosphate is only slightly soluble and no single-phased material could be recovered. The product recovered from the potassium phosphate reaction was completely amorphous and had almost no surface area. These pursuits were set aside when it was seen that the material synthesized from the trisodium phosphate appeared to be very similar to the phosphoric acid derivative, but showed a very high uptake for neodymium, with a K_d value of nearly 2×10^6 at pH 3 (this will be discussed further in a later chapter). It should be noted that, at this time, it is unclear if the only difference of the two materials is a substitution of Na^+ for H^+ or if the nature of the material is different altogether. Solid state ^{23}Na MAS NMR revealed a single symmetric resonance at –6 ppm with respect to sodium chloride, which is common for the loosely bound sodium ion. While the NMR data is not conclusive it does support the hypothesis that Na^+ is simply replacing the proton as the exchangeable cation.

Several attempts were made to convert the proton phase to the sodium phase post-synthetically by titration. First a dynamic titration was performed using a Radiometer Analytical TIM860 auto titrator with a 0.1 M NaOH and 0.1 M NaCl solution at rate of 0.01 mL/min and 20 mg of Zr–hybrid, however no inflection point was observed. Thinking that the inflection point had been overrun; a less concentrated solution was used, 0.01 M [NaOH] and [NaCl], still no inflection point was observed. Every parameter adjustment resulted in a curve similar to titrating H_2O with NaOH, indicating it was not a dilution problem. If it was not a dilution problem, the next thought was, "It is a diffusion problem." To investigate this, a static titration was set up where several 20 mg samples were shaken with different concentrations of NaOH for 48 hours and the equilibrium pH was observed for each. The points obtained from the static titration fell on the curve obtained from the dynamic titration! The H–phased material could not be neutralized using NaOH and therefore could not be converted to the Na–phase. This will be discussed more in a later chapter, but it is believed that the free space between the layers, 3.3 Å, is too small for a hydrated Na^+ ion to diffuse into the layers.

3.6 Conclusion

These zirconium based inorganic organic hybrid ion exchange materials are a highly tunable class of compounds. A simple manipulation of synthesis temperature or reaction time has large impacts on the morphology and structure of the product. For our purposes, 120 ºC was found to produce the most advantageous material. While the

microporosity increased with reaction time, even up to 10 days, the impact on affinity towards neodymium was negligible, so 4–5 days was deemed to be acceptable for a general synthesis procedure. As expected, adjusting the ratio of pillar-to-spacer ligand caused sizable changes in the pore structure and pore size distribution of the materials. ^{31}P SS-NMR indicates that there is a limit to which the phosphate can be incorporated into the material, showing less phosphate present than expected when x = 1.60. Increasing this ratio also increased the Nd^{3+} affinity, causing the K_d value to increase by a factor greater than 5 going from x = 1.00 to x = 1.60.

The most impactful adjustment observed was that of the phosphate source. By starting with tribasic sodium phosphate the K_d values increase ~ 50 fold. The exact source of this increase is still ambiguous, but this discovery, which will be covered more extensively in a later chapter, has resulted in a material that quantitatively removes Ln^{3+} and, as will be seen, An^{3+} ions are removed in a similar fashion, providing tremendous potential in closing the nuclear fuel cycle.

CHAPTER IV

MATERIALS DEVELOPMENT:

TIN

4.1 Introduction

The previous chapter described four basic synthesis parameters that have an important roll on the outcome of the zirconium-based ion exchange materials: 1) synthesis temperature, 2) synthesis time, 3) pillar-to-spacer ligand ratio, and 4) phosphate source of spacer ligand. This chapter seeks to point out the differences observed when the tetravalent metal ion is changed from zirconium to tin. Only two of the four basic areas will be discussed in detail: 1) synthesis temperature (Section 4.2) and 2) pillar-to-spacer ligand ratio (Section 4.3). Changing the reaction time will not be investigated, because as will be seen, the Sn–hybrids are ≥ 95% microporous at shorter synthesis times, even after only four days. This is in contrast to the Zr–hybrids, which only reach ~ 73% microporosity after 10 days of heating (see Chapter III Section 3.3). With almost no mesoporousity there is no reason to investigate whether there is any annealing effect at longer reaction times. No investigations into alternate phosphate sources will be discussed in this chapter, except to state that bulk materials were synthesized from both phosphoric acid and tribasic sodium phosphate (the synthesis of materials is discussed in Chapter II Section 2.3.2 and a description of some of their physical properties is in discussed in Chapter V Section 5.2). That it is to say, this approach of starting with

Na_3PO_4 was immediately investigated without exploring the other group one phosphates (Li_3PO_4 and K_3PO_4) because of the marked improvement in lanthanide affinity when synthesizing from the sodium phosphate in place of phosphoric acid in the Zr–hybrids. As will be seen, the Sn–hybrids have many similarities to the zirconium analogs, but where they do differ the distinctions are conspicuous and worthy of independent investigations.

4.2 Synthesis temperature

Much like the zirconium analogs, a series of experiments was designed to determine the effect synthesis temperature has on the formation and structure the tin ion exchangers. The synthetic procedure follows that for the general procedure varying the reaction temperature 80–200 ºC (see Chapter II section 2.3.1.1). The XRPD patterns are very similar to those of the Zr–hybrids, with four broad, weak reflections at ~ 9.6, 4.1, 3.4 and 2.5 Å (see Figure 19). The first reflection is in line with Zr–hybrids showing an identical d-spacing, reinforcing the hypothesis that the first reflection correspond to the interlayer distance, which is that of the metal layers being held apart by the diphosphonate pillar ligands. The other three reflections all have smaller d-spacing than their zirconium counterparts, which is expected as the Sn^{4+} ion is smaller than that of the Zr^{4+} ion. With the assumption these are generated from intralayer atom spacings, we would expect these later three reflections to be sifted to larger angles, resulting from

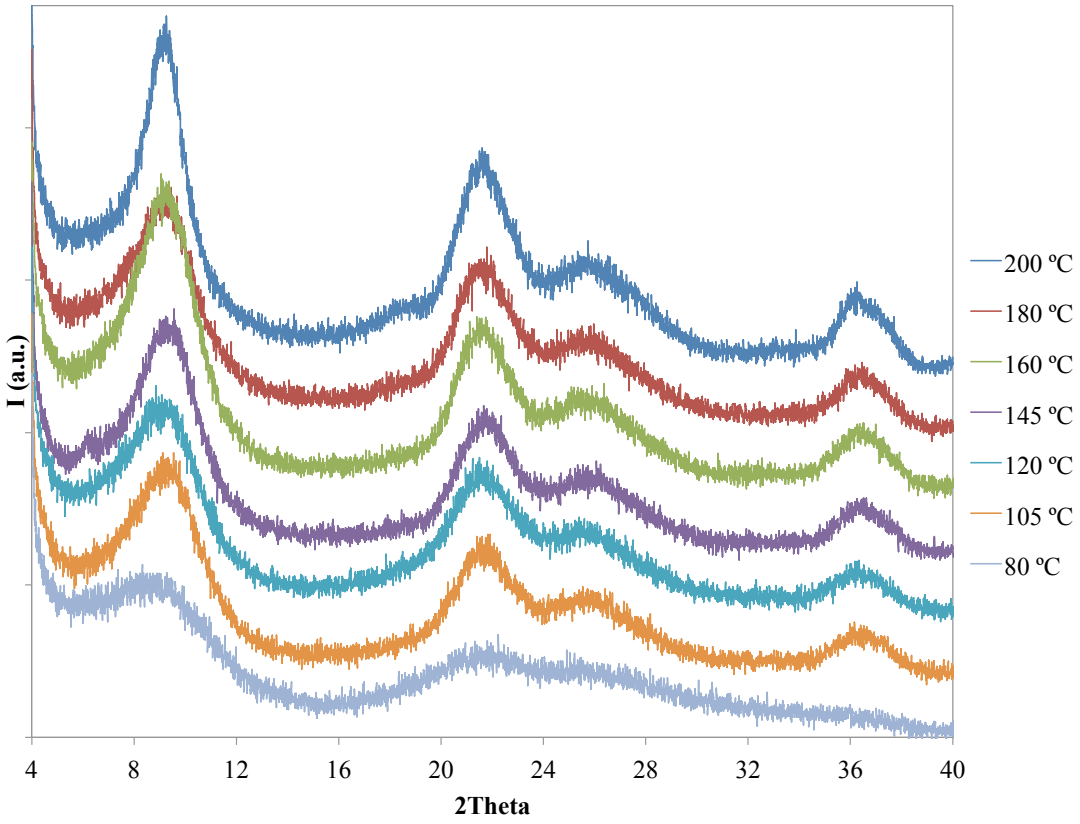

Figure 19: XRPD patterns of Sn-hybrid materials synthesized from 80–200 ºC.

smaller d-spacings. The hybrid synthesized at 80 ºC displays the weakest diffraction pattern and appears not to be fully formed. All other patterns have very similar features, with a subtle increase in crystallinity as a function of synthesis temperature. Unlike the Zr–hybrids there is no evidence in the XRPD patterns that a multiphased system is being synthesized, even up to 200 ºC.

An investigation of the thermal decomposition, presented in Figure 20 and Figure 21, of the Sn–hybrids reveals a four weight loss decomposition pathway occurring from 0–190 ºC (10%), 190–450 ºC (3.5%), and the last two from 450–720 ºC (11%). The tin hybrids differ from the zirconium in that they have a slight gain in mass from 720–1000 ºC (0.5%), which is believed to be the oxidation of the phosphorus species that lose an OH moiety during phosphate condensation to result in the production of stannic pyrophosphate (SnP_2O_7) as identified by XRPD; the reader should keep in mind that the TGA was run in 90% air, so sufficient oxygen is available. This gain is not observed for the Zr–hybrids. It should be noted at this point, as mentioned earlier, that the material synthesized at 80 ºC does not appear to have been subjected to high enough temperature and therefore the activation energy to form the ion exchange material was not reached. TGA revealed a water loss of ~ 15% up to 460 ºC, followed by a major multicomponent loss of ~ 50% from 460–750 ºC, with no further loss observed up to 1000 ºC. It is unknown what type of material is formed at 80 ºC and it is of little interest for this study, so it will not be investigated further. To a lesser extent, the exchanger

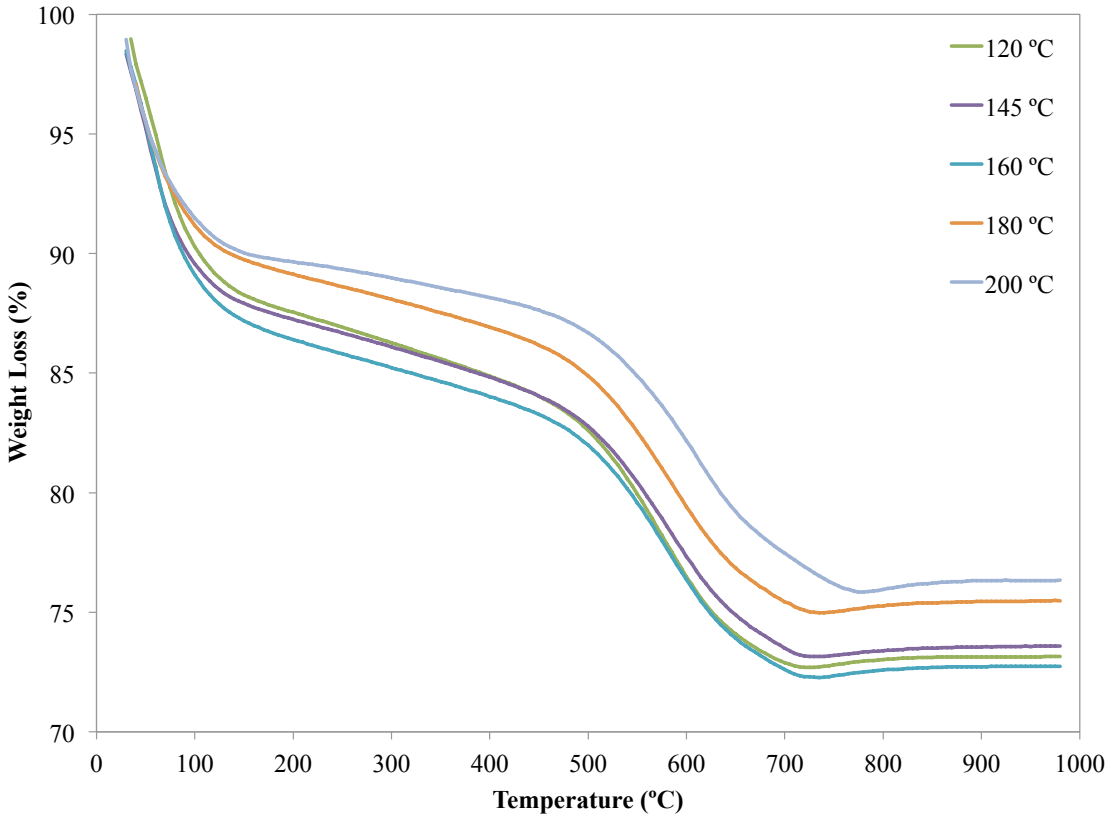

Figure 20: Thermal decomposition of Sn–hybrids synthesized from 120–200 ºC.

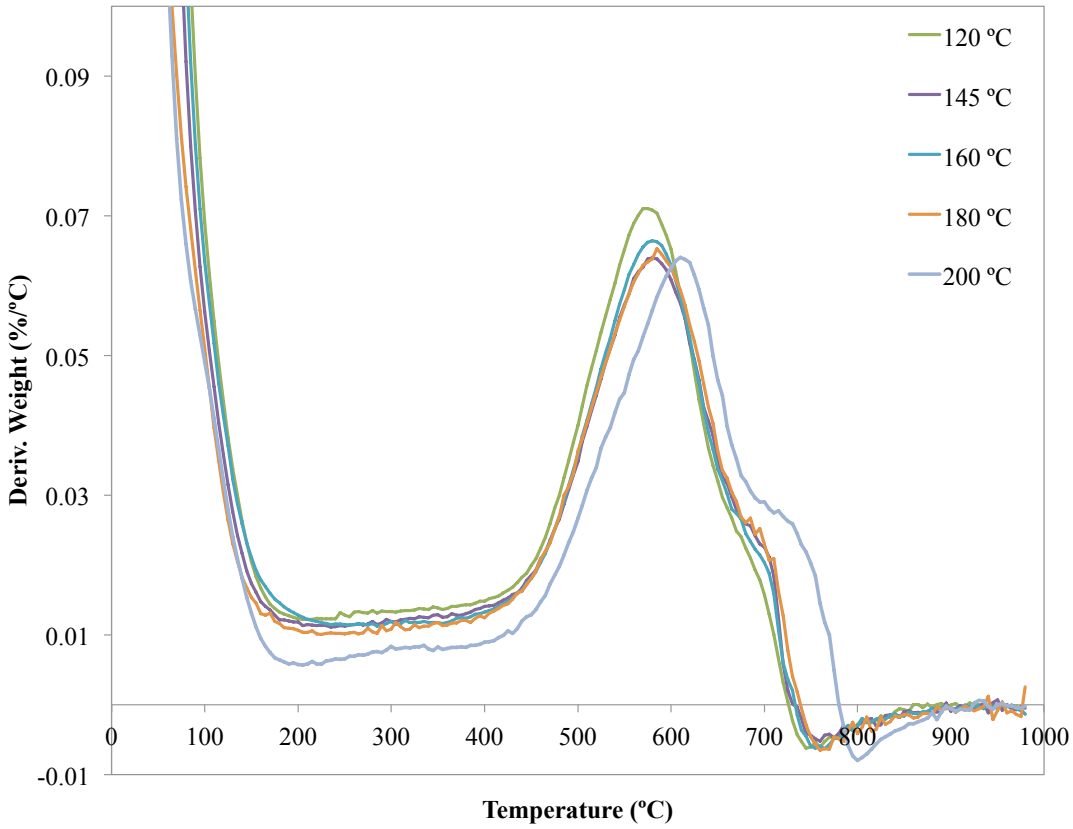

Figure 21: 1st derivative of the TGA signals for the Sn–hybrids synthesized at 120–200 ºC.

synthesized at 105 ºC has a similar multicomponent decomposition pathway from 450–725 ºC; this material will also be left out of further investigations.

Comparing the TGA results with the element analysis, as summarized by Table 16, it can be seen that the actual molecular formula is within experimental error of the ideal formula provided. The Sn:P ratios were not determined because these materials proved very difficult to digest and therefore a good ICP measurement could not be made. The yields were all above 76%. It may be noticed that the reported yields for the Sn–hybrids are distinctively lower than those of the Zr–hybrids. The reason for this is that the particle size for the tin based materials is dramatically smaller than the zirconium materials. The particles are so small, in fact that the smallest of these particles pass through Whatman No. 1 filter paper. This can be avoided to some extent by using Millipore Durapore® membrane filters, but even still the tiniest particles are trapped in the pores of the filters. This accounts for roughly 50 mg of the sample. The loss of 50 mg of sample is much less significant when the reaction is scaled up. The bulk reactions resulted in much higher yield almost quantitative (see Table 2 in Chapter II Section 2.3.2).

The Sn–hybrids N_2 sorption isotherms can be generally characterized as a Type I isotherm with H4 type hysteresis loops (see Figure 22). The materials synthesized at 200 ºC behaved differently than the other materials and will be discussed last. Below 180 ºC the isotherms are zeolite-like in shape, which indicates a uniform pore size

Table 16: Molecular formula determination and percent yield calculation based on the TGA and elemental analysis for Sn–hybrid ion exchange materials, estimated error < 5%.

Synthesis Temperature	Formula	FW	%C		%H		Yield (g)	% Yield[a]
			Calc	Exp	Calc	Exp		
120 ºC	$Sn(O_6P_2C_6H_4)_{0.5}(O_3POH)\bullet 2.98H_2O$	385.3	9.3%	9.1%	2.3%	1.9%	0.378	87%
145 ºC	$Sn(O_6P_2C_6H_4)_{0.5}(O_3POH)\bullet 2.99H_2O$	385.5	9.3%	10.0%	2.3%	1.6%	0.331	76%
160 ºC	$Sn(O_6P_2C_6H_4)_{0.5}(O_3POH)\bullet 3.24H_2O$	390.0	9.2%	9.6%	2.3%	1.6%	0.336	77%
180 ºC	$Sn(O_6P_2C_6H_4)_{0.5}(O_3POH)\bullet 2.23H_2O$	371.8	9.7%	9.8%	2.4%	1.5%	0.337	81%
200 ºC	$Sn(O_6P_2C_6H_4)_{0.5}(O_3POH)\bullet 2.09H_2O$	369.3	9.8%	10.0%	2.4%	1.8%	0.319	77%

a: Based on starting amount of Sn

distribution in the micropore regime. Table 17 summarizes the total surface area as determined by the BET method and the percent microporosity as determined by *t*-plot method. The total surface area increases as the synthesis temperature increases, while the percent microporosity slightly decreases with synthesis temperatures. The material synthesized at 200 ºC has a modified Type I isotherm, with a much larger H4 hysteresis loop. The region below 0.5 P/P_0 shows a much more shallow slope, which is representative of a large pore size distribution. At this point the mechanism of pore formation is uncertain, but it does appear that elevating the synthesis temperature to 200 ºC provides enough energy to allow rearrangement of ligands, thus creating a wide distribution of pores. Chemically speaking, the phenyl ring in the diphosphonate is highly hydrophobic while the phosphate is hydrophilic, increasing the energy of the reaction system could allow the ligands to migrate and aggregate together into distinct regions. The formation of distinct regions could account for the wider range of pore sizes. The materials synthesized at 200 ºC will not be investigated further, because a non-statistical arrangement of ligands creating many different types of pores adds a new level of complexity into understanding the materials and is therefore not desirable for our purpose.

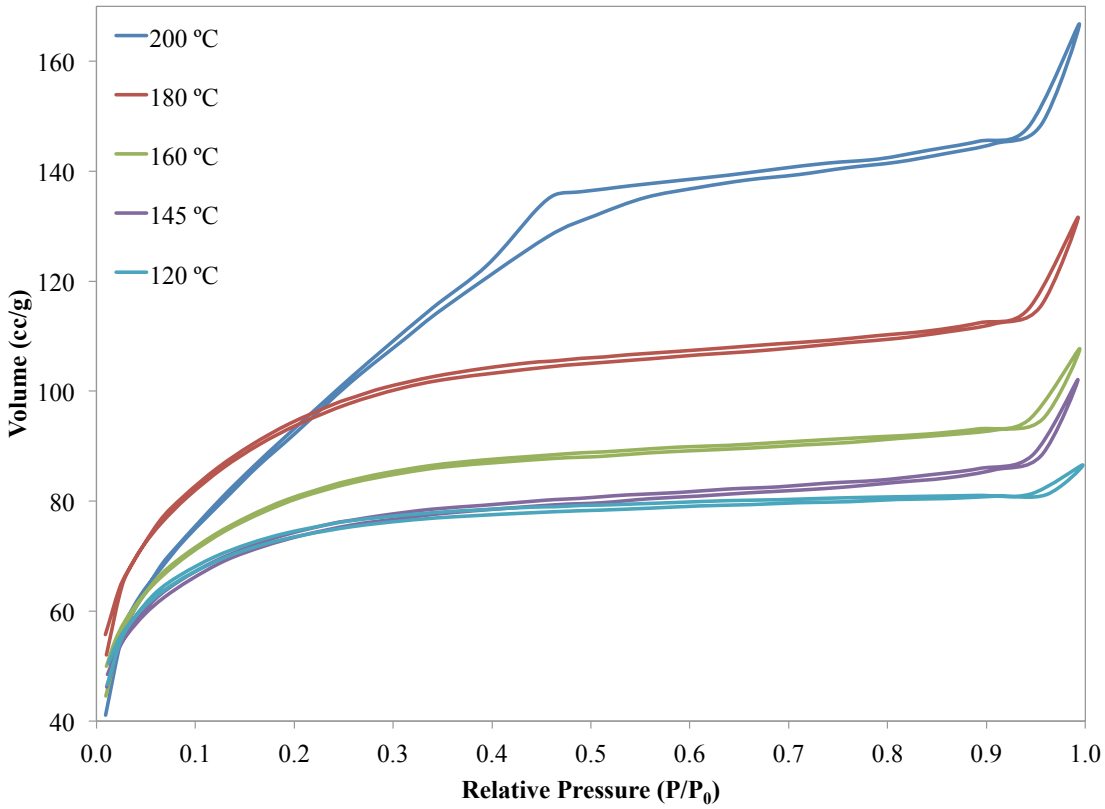

Figure 22: N_2 sorption isotherms of Sn–hybrids synthesized at 120–200 ºC.

Table 17: N_2 sorption surface area data determined from BET and percent microporosity by *t*-plot, estimated error < 10%.

Synthetic Temperature	Total Surface Area (m^2 g^{-1})	Microporous (%)
120 ºC	270	98%
145 ºC	270	95%
160 ºC	290	96%
180 ºC	340	95%
200 ºC	340	94%

The K_d values were observed for materials synthesized at 120–180 ºC and are provided in Table 18. Just as is the case with the zirconium analogs there seems to be no correlation between Nd^{3+} extraction and synthesis temperature, and therefore, no benefit to increasing the synthesis temperature above 120–145 ºC. It should be remembered that the ion exchange materials are being developed for implementation on an industrial level, therefore ease and economy of synthesis is very desirable. In the lab there is little difference in a synthesis temperature of 120 or 180 ºC, but on an industrial scale this will add to the overall cost of production.

Table 18: Nd^{3+} affinity reported in K_d

Synthesis Temperature	K_d values (mL g^{-1})
120 ºC	32,000 ± 11,000
145 ºC	60,000 ± 3,000
160 ºC	35,000 ± 2,900
180 ºC	41,000 ± 7,300

The tin hybrid materials behave very similarly to those of the zirconium analogs, with the exception of the pore structure. It appears that there is an activation energy reached

in the vicinity of 120–145 ºC that is required to produce materials that are thermally stable and homogeneous. There is no observable benefit in the affinity towards Nd^{3+} to elevating the synthesis temperature above that which is required for material formation, and so, as in the case of the Zr–hybrids, all future materials will be synthesized at 120 ºC unless otherwise stated.

4.3 Pillar-to-spacer ligand ratio

Much like the zirconium analogs, it is important to understand the limit of which the spacer ligand, phosphate, can be substituted in for the pillar ligand, p-monophenyldiphosphonate, to increase the total efficiency of the ion exchange materials without losing functionality. For this, a similar set of reactions were designed where the relative amounts of pillar and spare ligands were adjusted so that x = 0.00, 0.66, 1.00, 1.33, and 1.50 in the ideal formula of $Sn(O_3PC_6H_4PO_3)_{1-x/2}(O_3POH)_x$. Once again, this will result in a P:S ratio of 1:0, 1:1, 1:2, 1:4, and 1:6, respectively. The XRPD patterns show very little change as x increases from 1.00 to 1.50 (see Figure 23). However, much like the Zr–hybrids, the pure p-monophenyldiphosphonate shows a much stronger first reflection, with a d-spacing ~ 9.6 Å.

Thermal decomposition of the tin based materials appears to behave similarly to the zirconium based materials as x is increased. The 1st derivatives of the TGAs are presented in Figure 24. The decomposition pathways are found in very similar

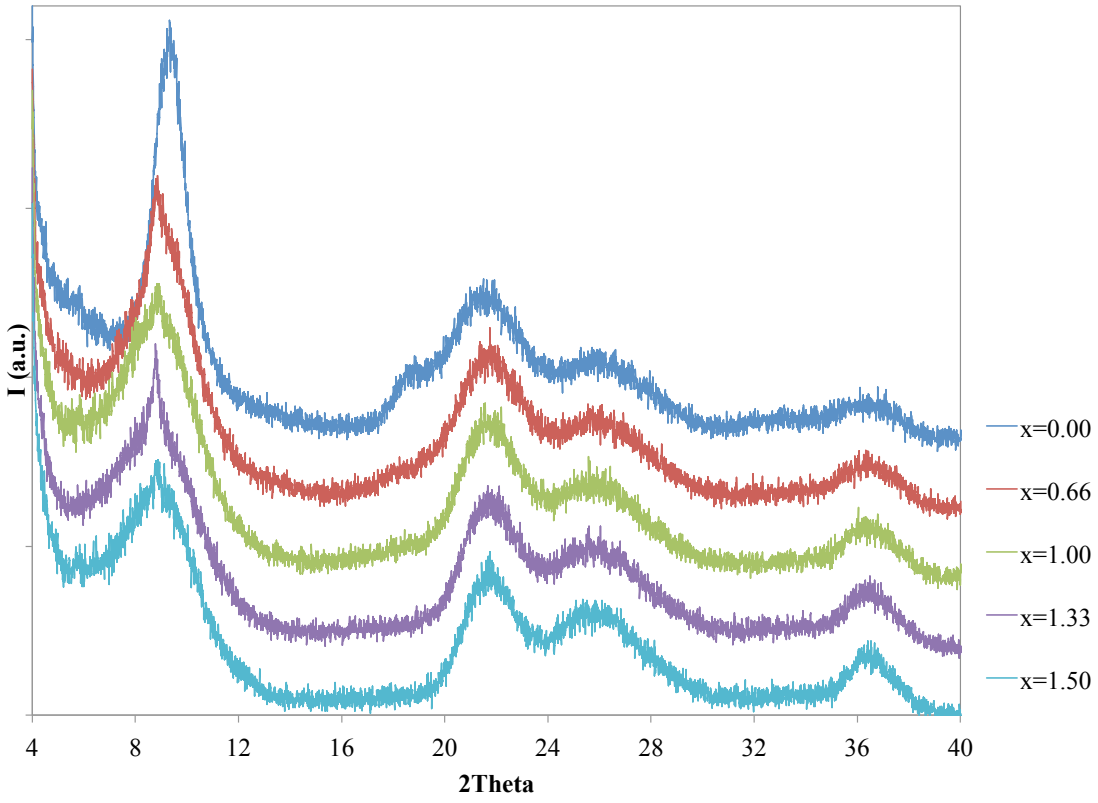

Figure 23: XRPD patterns of $Sn(O_3PC_6H_4PO_3)_{1-x/2}(O_3POH)_x$.

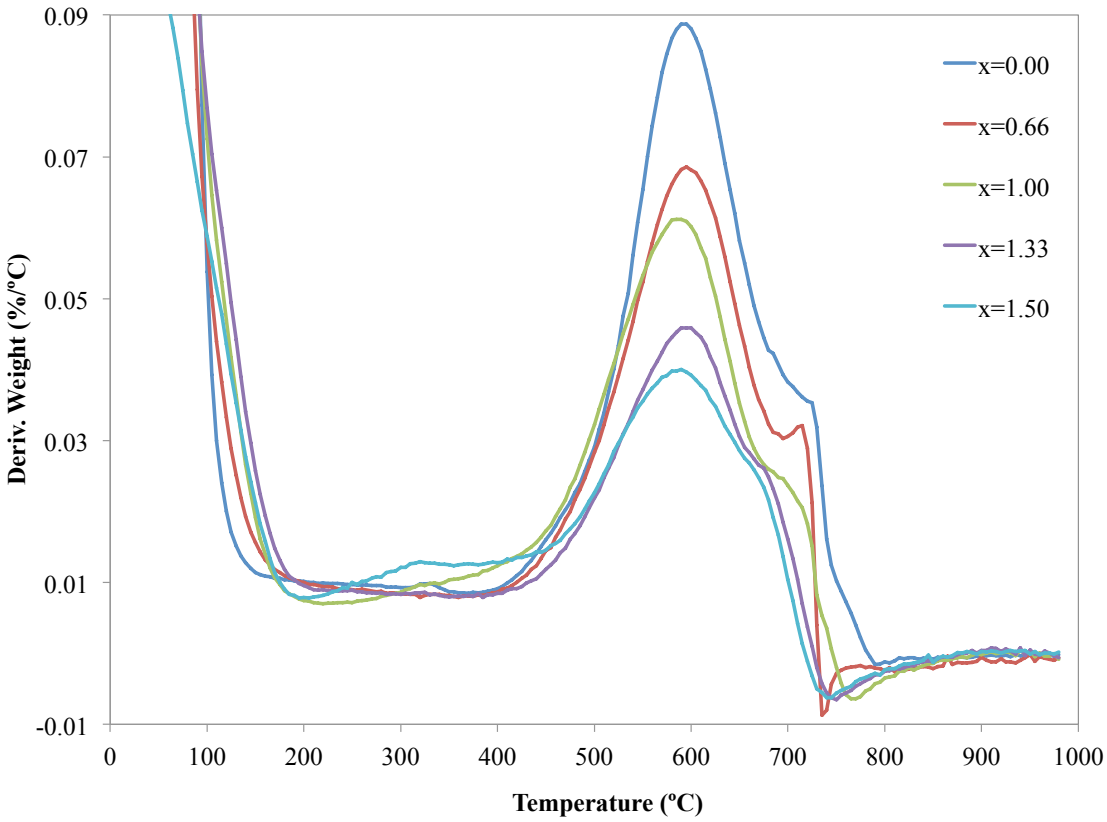

Figure 24: 1st derivative of the TGA of $Sn(O_3PC_6H_4PO_3)_{1-x/2}(O_3POH)_x$.

temperature ranges as discussed earlier for the Sn–hybrids. Still, much like the Zr–hybrid analogs, the decomposition observed from 400 ºC to just under 700 ºC decreases as the starting amount of pillar ligand is decreased. The oxidation to the pyrophosphate phase from 720 to 1,000 ºC becomes more pronounced as the relative amount of the spacer phosphate is increased which allows more condensation, thereby forcing more oxidation to occur.

The carbon hydrogen elemental analysis is in accordance with the 1st derivative of the TGA and is presented in Table 19. The amount of carbon decreases as *x* is increased from 0.00 to 1.33. Much like with the Zr–hybrids the percent carbon and hydrogen were calculated using the ideal formula of $Sn(O_3PC_6H_4PO_3)_{1-x/2}(O_3POH)_x \bullet 2H_2O$ and also showed a good correlation for the % C between the calculated and experimental values. The % H is higher than expected and probably is a result of a higher absorbed water content caused by the high microporous surface area exhibited by the tin based materials.

Table 19: C and H percent based on elemental analysis as a function pillar-to-spacer ratio of $Sn(O_3PC_6H_4PO_3)_{1-x/2}(O_3POH)_x$.

x =	% C		% H	
	Calc	Exp	Calc	Exp
0.00	18.5%	16.0%	1.5%	2.8%
0.66	12.8%	12.7%	1.4%	2.7%
1.00	9.8%	8.8%	1.4%	2.5%
1.33	6.6%	6.2%	1.3%	2.3%
1.50	5.0%	–	1.3%	–

The most curious difference between the Zr–hybrids and the Sn–hybrids when adjusting *x* is observed in the N_2 sorption isotherms and calculated surface areas, presented in Figure 25 and Table 20, respectively. There is no observable difference in the percent microporosity; conversely there is a decrease in total surface area as amount of the spacer ligand added to the reaction mixture is increased. This decrease was seen only in the zirconium based materials after an initial increase when the phosphate was first incorporated into the framework. This result is quite curious, as we were expecting the porosity to be primarily generated from the addition of the spacer phosphate ligands. It would appear rather that there is a different primary source of porosity, at this point believed to be caused by defects similar to those discussed regarding the Zr–hybrids (see Chapter III Section 3.4), because the material with the highest surface area is that with no spacer ligand. However, this is unexpected because the pore structure is very uniform as indicated by the Type I isotherms. You would imagine that if defects were the primary source of porosity, the pore structure would be more random and show a much broader pore size distribution. That being said, for this study, determining the exact source and nature of porosity is outside our goal of developing ion exchange materials. When *x* is increased to 1.50 a very large drop in surface area, roughly 46% below that of the pure derivative, is observed. Because the surface area drastically decreased, this sample was not investigated further.

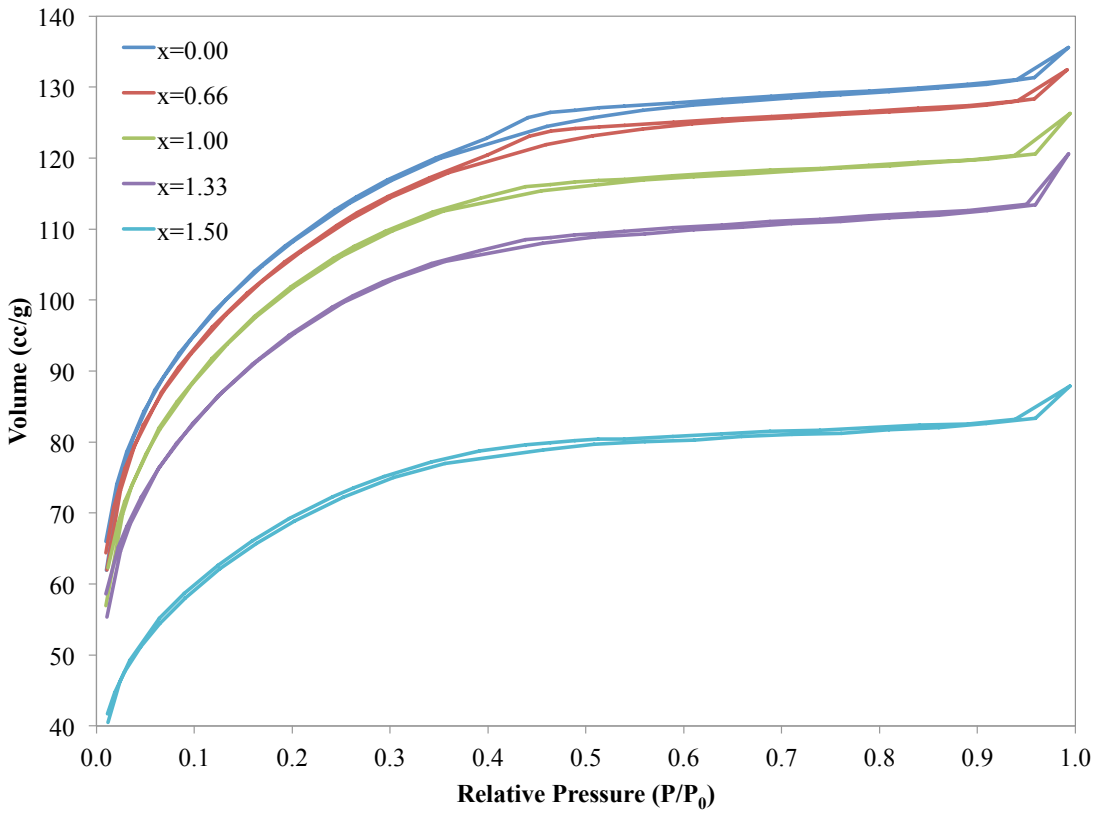

Figure 25: N_2 sorption isotherms of $Sn(O_3PC_6H_4PO_3)_{1-x/2}(O_3POH)_x$.

Table 20: The calculated total surface area (BET) and percent microporosity (*t*-plot) for $Sn(O_3PC_6H_4PO_3)_{1-x/2}(O_3POH)_x$, < 10% estimated error.

x =	Total Surface Area (m^2 g^{-1})	Microporous (%)
0.00	390	98%
0.66	380	98%
1.00	370	98%
1.33	340	98%
1.50	250	98%

The ^{31}P Magic Angle Spinning (MAS) solid-state nuclear magnetic resonance (NMR) spectra were obtained for the materials where x = 0.00, 0.66, 1.00, and 1.33 and are shown in Figure 26. The pure p-monophenyldiphosphonate, much like the zirconium counterpart, has multiple visible resonances centered on 5 ppm and aligns with literature results [74]. There is a slight shoulder downfield which indicates multiple phosphorus species in slightly different environments. These multiple phosphorus resonances are believed to be from defects in the framework as discussed earlier in regards to the high internal microporous surface area. One option is visualized in Figure 18 (see Chapter III Section 3.4), however, this is hard to imagine in case of the Sn–hybrids because a more irregular pore size distribution should result from such an arrangement. As mentioned previously to fully understand the formation and structure of these materials more research is needed.

Once a second ligand is added to the reaction mixture, the spacer ligand (S), a second major ^{31}P resonance appears at –14 ppm corresponding to the $–O_3POH$ [75-77]. This resonance grows as x is increased from 0.66 to 1.33; however, the relative amount of the

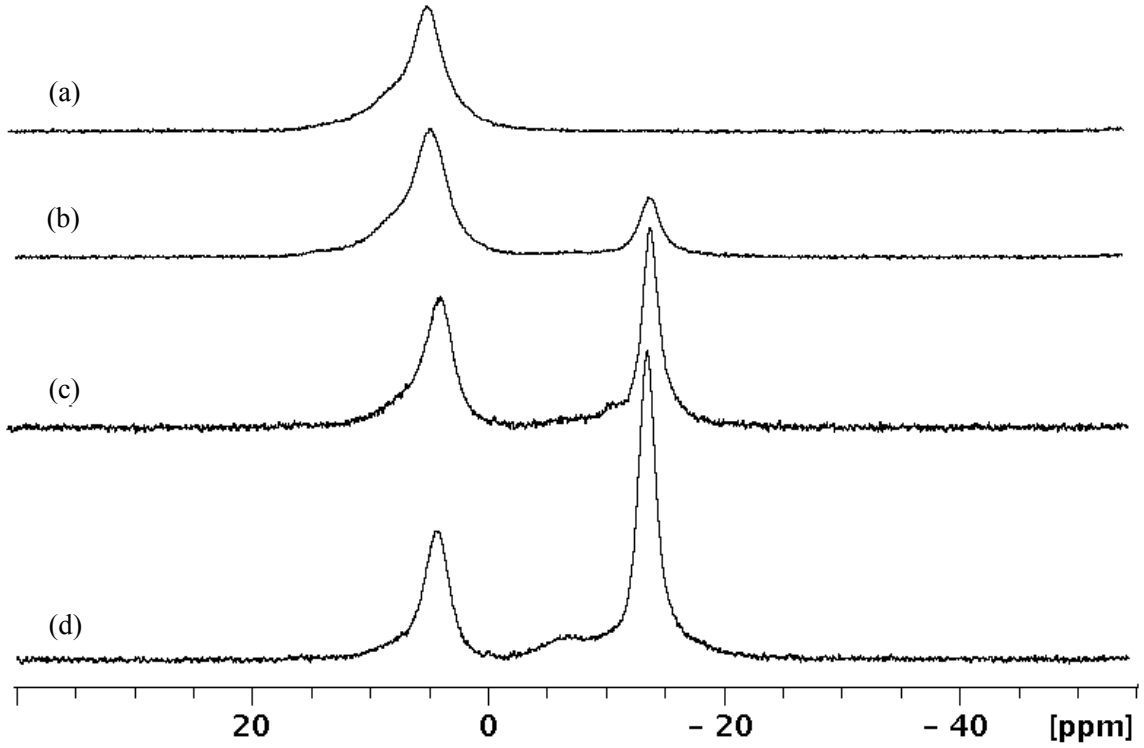

Figure 26: MAS solid-state ^{31}P NMR spectra of $Sn(O_3PC_6H_4PO_3)_{1-x/2}(O_3POH)_x$ with x = 0.00 (a), 0.66 (b), 1.00 (c), and 1.33 (d).

phosphate ligand in the reaction mixture does not correspond directly with the amount that is incorporated into the final product of the materials. By calculating the area under the respective signals a rough ratio of pillar-to-spacer ligand (P:S) can be calculated; the results of this calculation are presented in Table 21 along with the expected ratios based on the relative amounts of reagents in the reaction mixture. When x = 0.66, just over half of the spacer ligand added to the reaction mixture actually gets incorporated into ion exchange material. Likewise, when x = 1.33, the ratio is lower than what was expected, and there appears to be some small amount of spacer ligand that interacts differently than the majority of the phosphate (this point will be discussed in more detail below). Conversely, when the arbitrary ratio of 1:2 (P:S) is used, the expected amounts of pillar and spacer are observed in the ^{31}P NMR. It is interesting to note that this result is serendipitous to the implementation of generic procedure of a 1:2 pillar-to-spacer ratio.

Table 21: Pillar-to-spacer (P:S) for $Sn(O_3PC_6H_4PO_3)_{1-x/2}(O_3POH)_x$ calculated from the integration of the ^{31}P NMR spectra in Figure 26.

x =	P:S	
	Calc	Exp
0.66	1:1	1:0.6
1.00	1:2	1:2.0
1.33	1:4	1:3.8

There are other observations that can be made from the data in Figure 26. First, the shoulder observed in the pure phosphonate derivative seems to diminish as more phosphate is introduced and is almost completely nonexistent when x = 1.33. As

mentioned earlier, for the material where $x = 1.33$, the major phosphate resonance at –14 ppm is smaller than expected, nonetheless, there is a new resonance at –7 ppm that accounts for the remaining balance of phosphate. This new resonance may be the reason why the total surface area begins to decline as x increases and as will be seen momentarily why there is a large decrease in Nd^{3+} affinity.

The affinity towards neodymium was observed for $x = 0.66$–1.33 and the K_d values are provided in Table 22. The maximum uptake of Nd^{3+} was observed for $x = 1.00$, with a striking drop on increasing x to 1.33. This drop of over 75% is quite surprising when compared to the zirconium analog, as the Zr–hybrids behaved in a predictable manner having a direct correlation between relative amount of phosphate and Nd^{3+} affinity. More research is needed to understand the structure and ion exchange bonding mechanism, but it is clear from these results that the benefit of increasing the total number of active sites in the material does not guarantee that the K_d value will follow suit.

Table 22: K_d values observed for $Sn(O_3PC_6H_4PO_3)_{1-x/2}(O_3POH)_x$ at pH ~ 3.

x =	K_d values (mL g^{-1})
0.66	92,000 ± 14,000
1.00	159,000 ± 2,000
1.33	39,000 ± 2,000

Adjusting the starting pillar-to-spacer ratio in the reactions gave very different results for the tin based ion exchangers than for their counter zirconium based exchangers. While the XRPD patterns and TGA decomposition pathways have similar trends upon increasing *x*, the N_2 sorption, solid-state ^{31}P NMR, and Nd^{3+} affinity behaviors were much different. The short-range order of these materials must be different and will need to be understood to explain the differing performance of the two materials. At present, for the current study, it is clear that for the Sn–hybrid materials $x = 1.00$ produces the most advantageous product providing a large microporous surface area, a clear ^{31}P spectrum with the appropriate amounts of the two types of phosphorus, and the highest neodymium affinity.

4.4 Conclusion

The tin based hybrid ion exchange materials appear to have several similarities to their zirconium analogs such as their XRPD patterns and neodymium affinities when changing the synthesis temperature. The thermal decompositions were aligned with the Zr–hybrids, however they had a visible increase in mass in the last step of producing the metal pyrophosphate final product. As stated earlier the gain is most likely caused by the oxidation of the phosphorus that had lost an oxygen during the condensation step and is also believed to be taking place with the Zr–hybrid analogs despite not being observed. The most obvious discrepancy upon changing from zirconium to tin is the porosity. Unlike the bimodal distribution of the Zr–hybrids, the Sn–hybrids have only

one pore size distribution in the microporous regime and are zeolite-like in their pore structure. They do not exhibit the "house of cards" particle arrangement that leads to the meso- and micropore size distributions of the zirconium based materials. This should allow for a more regular environment around the active ion exchange sites.

Attempting to increase the efficiency of the Sn–hybrid ion exchange materials by altering the pillar-to-spacer ligand ratio did not result in the expected outcome. Both the surface areas and K_d values were out of line with the Zr–hybrids. There appears to be more going on at the molecular level of the materials than just a simple substitution of the tetravalent metal within the layer. Further investigation into the exact source of the discrepancy is needed to have a thorough understanding of the difference in their behavior; however, for the time being, one thing is clear, the arbitrary 1:2 pillar-to-spacer synthesis provides a material with large surface areas in the microporous regime and high affinities for Nd^{3+}.

Despite their subtle differences, both M(IV) inorganic organic hybrid ion exchange materials display promising characteristics for applications in separations, with their high affinities for trivalent lanthanides. This will be developed more in a later chapter, but suffice it to say, both are selective for ions with high charges ($\geq$ 3+) and, as such, were investigated more thoroughly regarding their ion exchange properties.

CHAPTER V

ION EXCHANGE*

5.1 Introduction

As previously mentioned the purpose for developing the pillared M(IV) phosphate phosphonate inorganic organic hybrid ion exchange materials is to produce a material that is selective for a particular ion and not another. Ion exchange is a charge neutral process, which is to say that for each ion sorbed there must be a charge equivalent ion or ions desorbed. This is important to keep in mind throughout the following sections, as some interesting results were observed in ion affinity when sodium is the exchangeable counter cation. One of the major driving forces in ion exchange is the coulombic attraction between the immobile active sites on the surface of ion exchange material and the charge of the ions in solution. Neglecting other factors, such as steric hindrance of bulky ions, there should be an increase of affinity with an increase of effective charge (Z_{eff}). The electrostatics combined with the steric restriction of the interlayer free space of ~ 3.3 Å should lend themselves to a system in which a separation can be performed.

---

* Part of this chapter is reprinted with permission from "Pillared metal(IV) phosphate-phosphonate extraction of actinides." Burns, J. D.; Clearfield, A.; Borkowski, M.; and Reed, D. T. *Radiochim. Acta*, **2012**, *100* (6), 381-387 by Copyright 2012 Oldenbourg Wissenschaftsverlag; "Separation of oxidized americium from lanthanides by use of pillared metal(IV) phosphate-phosphonate hybrid materials." Burns, J. D.; Borkowski, M.; Clearfield, A.; and Reed, D. T. *Radiochim Acta*, **in press**, by Copyright 2013 Oldenbourg Wissenschaftsverlag; and ""Separation of americium from curium by oxidation and ion exchange." Burns, J. D.; Clearfield, A.; Shehee, T. C.; and Hobbs, D. T. **2012**, 84 (16), 6930-6932 by Copyright 2012 American Chemical Society.

Although the idea of separating one constituent from another appears to be very simple, in practice it can be a nontrivial problem, especially true for the group separation of lanthanides (Ln) from actinides (An). The Ln-An separation is important for closing the nuclear fuel cycle, as roughly one-third of the fission products in the used fuel are Ln's [78], which act as poisons due to their high neutron absorption cross sections. The Ln's are limited and homogeneous in their chemistry, because the 4f orbitals have a relatively small radial extension and are actually buried below the 5d and 6s orbitals. The most stable oxidation state for the entire lanthanide series is 3+ (due to the "core"-like nature of the 4f electrons) and all are considered hard Lewis acids. The early An (while they also are filling f orbitals) have a more diverse chemistry, as the 5f orbitals extend outside of the 6d and 7s orbitals. The extension of the 5f orbitals is due to the relativistic effects from s and p electrons near the core of the nucleus in heavy elements, which shield the charge of the nucleus more effectively than those of lighter elements. The accessible 5f e^- allows for a whole gamut of reactions and oxidation states. One unique species that is only observed in the An series is the linear dioxocation, or actinyl ion ($[O=An=O]^{n+}$), which will play a major role in aqueous solution and therefore in any separation process that is proposed.

This work focuses on the separation of americium from other actinides, most importantly curium, and the separation of americium from lanthanides. This is a difficult problem, as Am in natural systems behaves primarily like a member of the heavy An, which are lanthanide-like in their chemistry due the relativistic effects being outweighed by the f-

orbital contraction. However, in strongly oxidizing environments higher oxidation states can be achieved for Am (V and VI), while Cm and Ln's are not known to exist in higher oxidation states in acidic environments (Ce, as the exception, can exist as Ce^{4+} and is widely uses as an oxidizing agent, among other uses). The difference in electronics of Am from Cm and the Ln's should serve as a basis for a separation.

This chapter will first provide a detailed description of the bulk M(IV)–hybrid materials that will be interrogated to expose their functionality in ion exchange processes (Section 5.2). Next, the ion affinity of mono- and divalent cations will be explored from groups 1 and 2 of the periodic table, respectively (Section 5.3). General trivalent cation affinity will be determined using Ln's, with a more through investigation of the series to determine what role ion size plays (Section 5.4). Other studies in this section will include the effects of pH on affinity in both a single and multi- lanthanide systems. The actinides will be investigated in a variety of oxidation states including III, IV, V, and VI, which exist as An^{3+}, An^{4+}, AnO_2^{+}, and AnO_2^{2+}, respectively (Section 5.5). The K_d values for both Am^{3+} and AmO_2^{+} were determined. A description of the synthetic route to realize the rare Am(V) species, as well as proposed mechanism of oxidation will be included. Lastly, a variety of separations will be discussed including a direct separation of americium from curium (Section 5.6). Other separations that will be discussed include intergroup alkali metals from lanthanides, alkaline earth metals from lanthanides, transition metals from lanthanides, and lanthanides from actinides. Separation factors (SF) of multi ion systems were directly observed.

5.2 Bulk M(IV)–hybrids

Four representative bulk samples were synthesized following the bulk synthesis procedure (see Chapter II Section 2.3.2) and characterized [79]. While much of this will be a rehashing of the two previous chapters, there are some important points that will be highlighted, as well as an emphasis that there is little change to the materials when the scale of the reactions is increased by a factor of ten. The XRPD patterns shown in Figure 27 are no different than what was described earlier, but it does serve to reinforce the original hypothesis that the first reflection represents the interlayer distance of roughly 9.6 Å, as it is the same for all four ion exchange materials. The next three reflections are visibly shifted to smaller d-spacings from zirconium to tin, once again these are believed to be in-plane values and account for the smaller size of the Sn^{4+} ion over the Zr^{4+} ion.

The TGA results are presented in Figure 28, and it can be seen that there is no noticeable deviation from what was discussed earlier. However, it should be pointed out that all four of these materials are stable up to ~ 500 ºC, with the only loss being that of water to this point. The organics do not begin to decompose until after 500 ºC, making these hybrid ion exchange materials very thermally stable and therefore they should be a more robust medium to perform the separations required in the harsh environments of the nuclear fuel cycle.

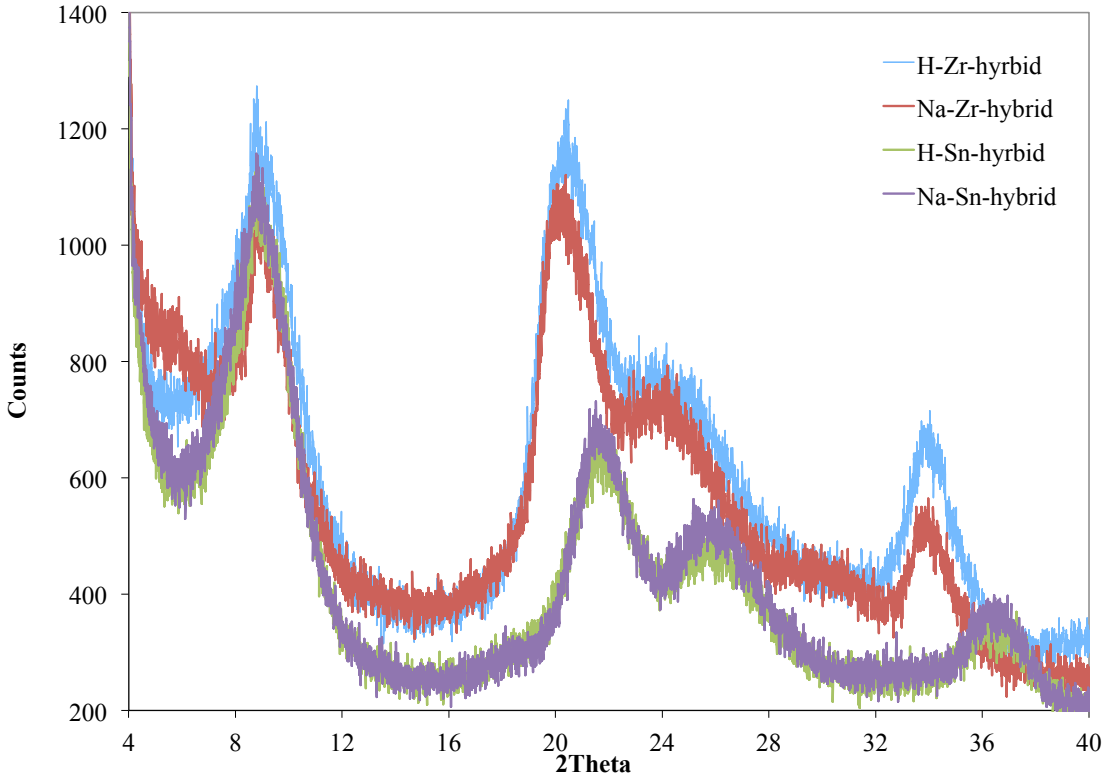

Figure 27: XRPD patterns of the four bulk M(IV)–hybrids.

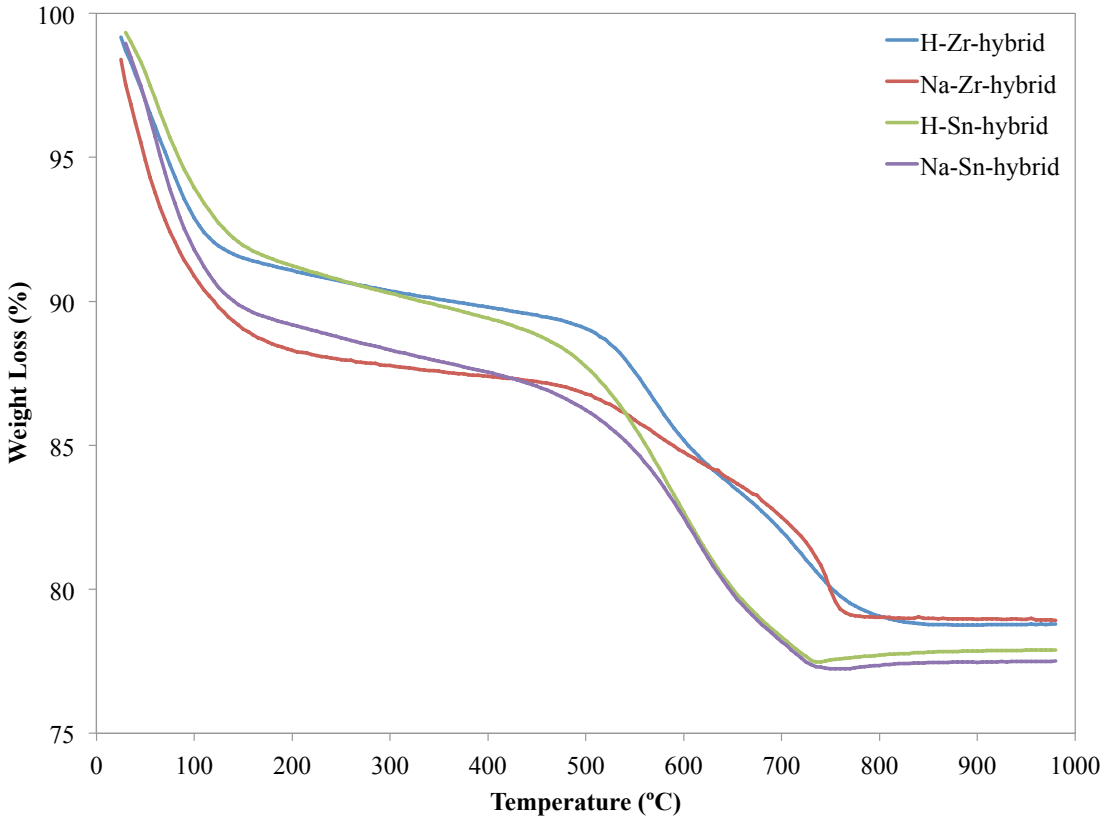

Figure 28: Thermogravimetric analyses of the four bulk samples.

The nitrogen sorption isotherms are also representative of the previous discussions. The zirconium-based materials have the same type II isotherms with an H4 hysteresis loop, while the tin-based materials are zeolite like in their isotherms (see Figure 29). The total surface area and percent microporosites are presented in Table 23 and were calculated from the multipoint BET and *t*-plot methods, respectively.

Table 23: Calculated total surface area (BET) and microporous percent (*t*-plot) for bulk ion exchange materials, estimated error < 10%.

Sample	Total Surface Area (m^2 g^{-1})	Microporous (%)
H–Zr–hybrid	440	72%
Na–Zr–hybrid	250	56%
H–Sn–hybrid	400	98%
Na–Sn–hybrid	370	98%

Imaging these materials by scanning electron microscopy (SEM) show the inherent nanoparticle nature of these materials (see Figure 30). The Zr–hybrids show larger cluster-like aggregates of platelet particles, as discussed in Chapter III forming a "house-of-cards" conformation; while the Sn–hybrids, also having platelet particles, seem to form small stacks of aggregates. The particles in all cases seem to ≤ 100 nm in size and there is no regular shape from one to the next.

Now that it is clear that the bulk materials are in line with the exploratory studies done in the previous two chapters, the focus will be shifted to an in-depth study of the ion exchange properties of these four representative hybrid materials.

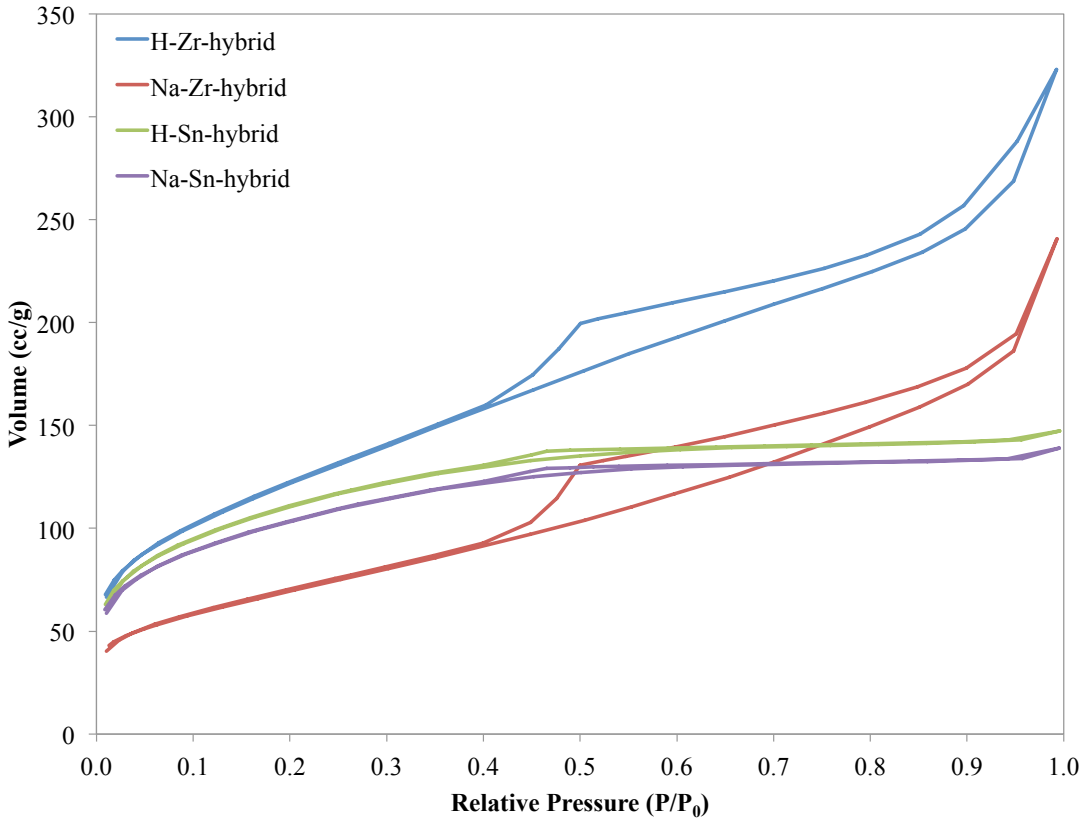

Figure 29: N_2 sorption isotherms of bulk samples.

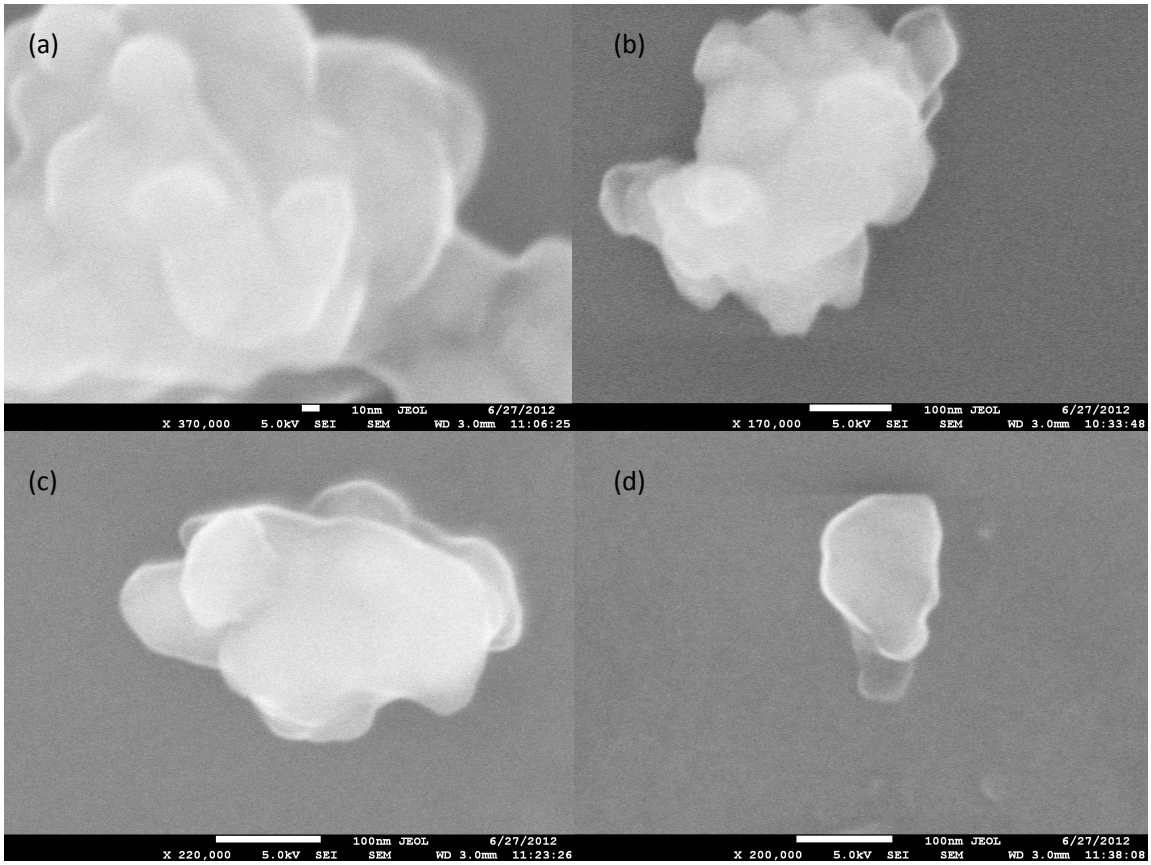

Figure 30: SEM images of the H–Zr–hybrid (a), Na–Zr–hybrid (b), H–Sn–hybrid (c), and Na–Sn–hybrid (d).

5.3 Group 1 and 2

The affinity for the metals of groups 1 and 2 in the periodic table were investigated to determine the general affinity of mono- and divalent cations, respectively. The K_d values are provided in Table 24 and reported in mL g^{-1}. In general, there is an increase in affinity going down the group, or as the size of the ion increases, $Na^+ < Cs^+$ and $Ca^{2+} < Sr^{2+}$. The increase in affinity down a group, presumably, is associated with the heat of hydration ($\Delta_{hyd}H$), which becomes less negative down the column, that is to say it becomes easier or takes less energy to remove the hydration sphere from the positively charged ion. According to our model, the free space between the metal layers is ~ 3.3 Å, leaving just enough space for the Cs^+ ion to diffuse into the material after shedding its hydration sphere. As reported earlier [49], it appears that at room temperature there is not enough energy for the Na^+ ion to dehydrate and diffuse into the layers. The divalent cations exhibit a higher attraction to the hybrid exchangers. There may be a number of effects at work here, the most important of which are the charge of the ion and the chelation-like properties of the ion occupying multiple active sites simultaneously. As discussed earlier there are believed to be clusters of pillar and spacer ligands, which would allow several ionic interactions to occur between a single divalent cation and multiple active sites in the material, as well as the ion having a higher coulombic attraction to the negatively charged $–PO^–$ moieties. It should be noted that the differences in affinity for groups 1 and 2 are of little consequence when compared to the lanthanides, as was reported in previous chapters and will be further discussed in the

next sections of this chapter. The lanthanide affinity is much larger than the mono- and divalent cations and is the major point of emphasis; moreover it will be seen that in a competitive reaction the separation factors between Nd-Cs and Nd-Sr favor the removal of Nd^{3+} by several orders of magnitude (see Section 5.6).

Table 24: K_d values (in mL g^{-1}) for groups 1 and 2 at pH 3, where <1 indicates no observable change in [M].

Sample	Na^+	Cs^+	Ca^{2+}	Sr^{2+}
H–Zr–hybrid	30 ± 30	450 ± 30	200 ± 100	650 ± 70
Na–Zr–hybrid	-	3,700 ± 300	800 ± 200	≥12,000
H–Sn–hybrid	<1	130 ± 10	20 ± 10	140 ± 10
Na–Sn–hybrid	-	260 ± 60	300 ± 100	650 ± 20

5.4 Lanthanides

The affinities of the Ln were investigated to gain a thorough understanding of their interaction with the hybrid ion exchange materials. Neodymium and samarium were chosen to represent the light Ln, while holmium and ytterbium represented the heavy Ln. This is necessary because, while the most stable oxidation state is 3+, there is a decrease of ionic radii across the series (almost 20% from La to Lu). That is to say, the size of the ion may play a large role in the overall binding. Table 25 displays the K_d values for the respective Ln. The H–Zr–hybrid shows a maximum affinity for Ho^{3+}, while the H–Sn–hybrid and the Na–M(IV)–hybrids show a decrease in affinities as the ionic radii

Table 25: K_d values (in mL g^{-1}) observed at pH 3 with a phase ratio of 250 mL g^{-1} for Nd^{3+} and 500 mL g^{-1} for Sm^{3+}, Ho^{3+}, and Yb^{3+}.

Sample	Nd^{3+}	Sm^{3+}	Ho^{3+}	Yb^{3+}
H–Zr–hybrid	29,000 ± 2,000	80,000 ± 10,000	110,000 ± 10,000	90,000 ± 10,000
Na–Zr–hybrid	≥ 1,900,000	1,310,000 ± 380,000	450,000 ± 110,000	450,000 ± 10,000
H–Sn–hybrid	340,000 ± 170,000	320,000 ± 20,000	320,000 ± 10,000	160,000 ± 10,000
Na–Sn–hybrid	480,000 ± 30,000	300,000 ± 10,000	220,000 ± 10,000	220,000 ± 10,000

decrease. These results appear to indicate a preference for a specific ion size that is most energetically favorable, presumably caused by a quasi-chelation of the ions, as mentioned earlier. This will be investigated further in a later section where these trivalent ions will compete in the same solution.

A better understanding of the final environment of the ion is required to make any conclusive statement on the binding characteristics of the materials. What can be seen however, is the much higher affinity for the Ln over the alkali and alkaline earths—in most cases three orders of magnitude—which implies an intergroup separation of the lanthanides from the alkali and alkaline earth metals, and has the possibility even to be translated to other mono- and divalent cations such as transition metals and actinides. Once again, it should be noted that, despite the apparently large errors in some cases (e.g. the sorption of Ho^{3+} on the Na–Zr–hybrid), the consequence of that error is negligible. The difference in a K_d value of 560,000 or 340,000 mL g^{-1} in terms of percent decontamination is 99.91% to 99.85% removal of Ho^{3+} from solution. These errors originate from detection limits of the instrument and the difficulty associated with scrubbing the water and acid clean of lanthanide contaminate prior to starting the analysis.

As mentioned earlier, ion exchange is a charge neutral process and while the Ln ions are trivalent, this does not guarantee that the naked cation is being sorbed to the materials. In other words, ligands such as nitrate could be coordinating the Ln ions and thereby

limiting the charge to either 1+ or 2+ of the molecular species and thereby change the nature of the ion exchange process entirely. To probe this, the pH of the lanthanide solution was determined before and after contact with the hybrids and the number of protons displaced was calculated and compared to the number of Ln^{3+} ions removed from solution. For naked Ln ions, there should be three times the number of protons released as Ln^{3+} ions removed. While the results varied slightly from sample to sample a general comparison will be made from one specific example using the H–Zr–hybrid and Sm^{3+}, where there were 2.8×10^{-3} mols of H^{+} released and 1.1×10^{-3} mols of Sm^{3+} removed from solution. These results indicate that upon sorption to the material the ions shed their coordination sphere and associate to the active site as the naked ion.

Neodymium was then selected for a more rigorous investigation, because it has been established as a good analog for americium in regard to both ionic radius and effective nuclear charge of the trivalent species [80, 81]. To probe the reversibility of the Ln/An sorption the K_d value was tracked as a function of acidity and plotted in Figure 31. The log-log plot shows a linear relationship between the K_d and acidity with slopes of 2.1, 2.9, and 1.7 for H–Zr–hybrid, Na–Zr–hybrid, and both Sn–hybrids, respectively. The Na–Zr–hybrid performed better than the other exchangers at pH 3, almost one whole order of magnitude better than the Sn–hybrids and two whole orders better than the H–Zr–hybrid; while its steeper slope indicates a greater ease of reversibility over the others, which will be shown later. These results indicate that a system of separation and

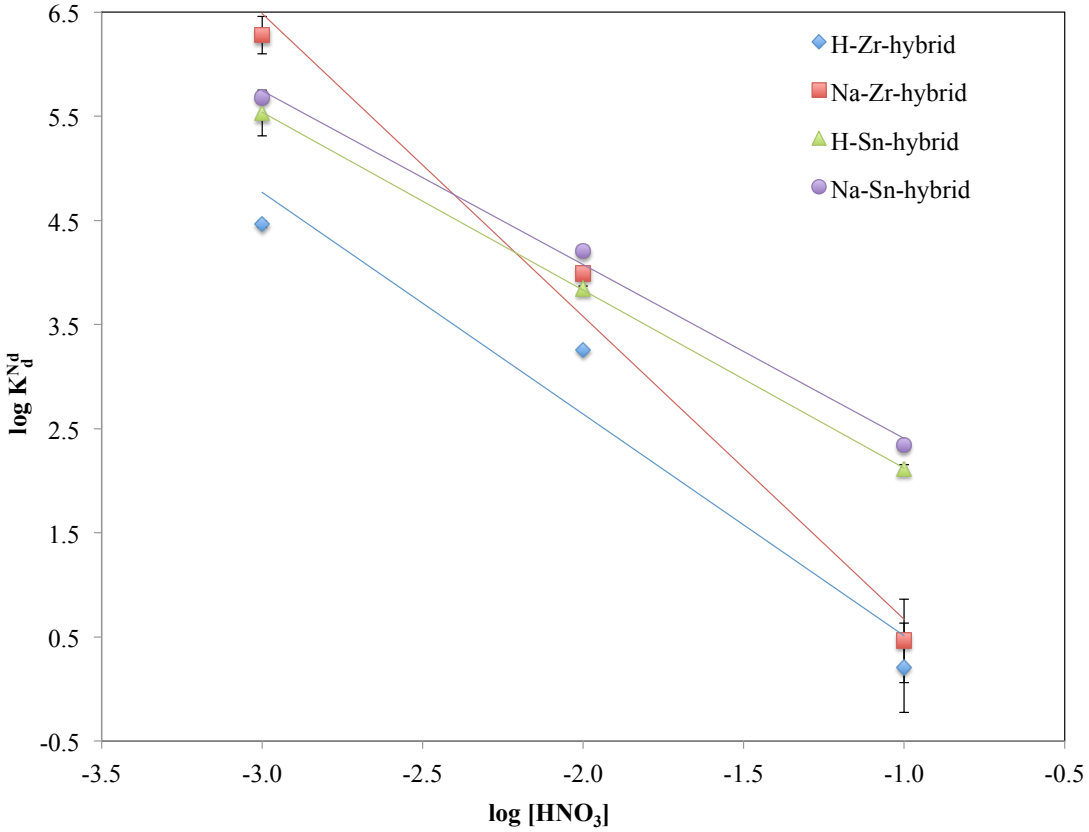

Figure 31: Extraction of Nd^{3+} as a function of [HNO_3], the initial [Nd^{3+}] was ~ 10^{-4} M. No uptake was observed for [HNO_3] > 0.1.

recovery should be able to be established and controlled by a simple manipulation of pH, most likely in some form of chromatographic separation.

5.5 Actinides

5.5.1 Basic sorption

The early transuranic elements (Np, Pu, and even Am) can exist in a variety of oxidation states including III, IV, V, and VI, which exist as An^{3+}, An^{4+}, AnO_2^{+}, and AnO_2^{2+}, respectively. Americium(III), plutonium(IV), neptunium(V) and americium(V), and plutonium(VI) were chosen as representatives for the different valencies of this series. Table 26 shows the results of the An uptake studies. The H–M(IV)–hybrids and Na–Sn–hybrid were in line with earlier results, having the general trend of increasing in K_d value as the charge on the ion increases. However, Pu^{4+}, at first glance, appears to be an exception to the trend, but taking into account that the experiments were performed at a lower pH, the results are very reasonable. It should be pointed out that the Zr–hybrid materials are not very ordered and some of the exchange sites may be isolated or even inaccessible altogether, which in turn may decrease the working exchange capacity as the charge on the ion increases. The Sn–hybrids have more regular pore structures, which should, alternatively, increase the uniformity of the active site environment, allowing for more and better access to the exchange sites. The Na–Sn–hybrid has a K_d value twice that of the H–Sn–hybrid, which can be accounted for by equilibrium

Table 26: K_d values (in mL g^{-1}) of the actinide species.

Sample	K_d $[AmO_2]^+$ pH 1.99	K_d $[NpO_2]^+$ pH 2.11	K_d Am^{3+} pH 2.00	K_d $[PuO_2]^{2+}$ pH 2.13	K_d Pu^{4+} pH 1.79
H–Zr–hybrid	2 ± 1	80 ± 4	4,870 ± 80	1,440 ± 80	1,340 ± 30
Na–Zr–hybrid	13 ± 1	3,000 ± 500	640,000 ± 53,000	240,000 ± 32,000[a]	109,000 ± 4,000
H–Sn–hybrid	14 ± 1	233 ± 9	12,100 ± 200	3,200 ± 300	43,000 ± 13,000
Na–Sn–hybrid	15 ± 3	480 ± 20	38,800 ± 1,400	6,100 ± 300	83,000 ± 5,000

[a]K_d obtained at pH 1.94

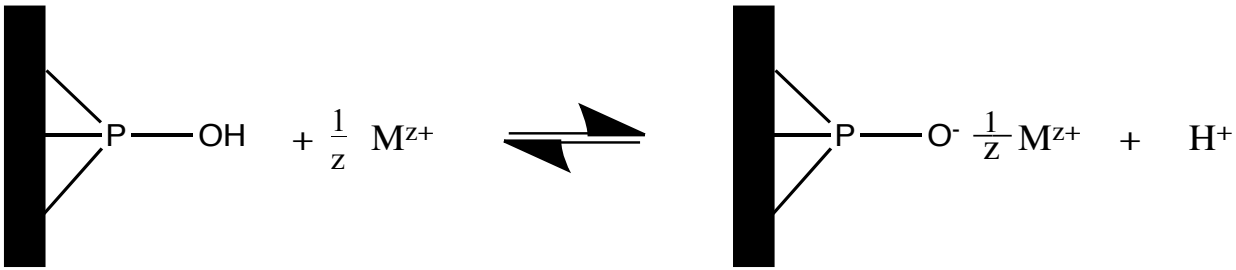

Figure 32: Schematic of the ion exchange equilibrium for the M(IV) hybrids.

considerations of the pH, meaning that because the extraction takes place in an acidic medium the equilibrium is pushed to the left in the case of the H–phased material (see Figure 32). There may also be small effects from the covalent character of the O–H bond that slightly decreases the metal sorption. At this point it should be noted that the K_d values for both Am(III) and Am(V) were observed in the presence of the Eu carrier, and therefore are not the true values but artificially lowered due to the presence of a competing ion. Am(III) will be far less affected by the presence of Eu^{3+} as the Z_{eff} of the two ions are very similar, however AmO_2^+ should be significantly reduced with a difference in Z_{eff} of 0.9 unit charges (see Chapter II Section 2.5.2 Table 6). The K_d value for carrier-free AmO_2^+ is expected to be very similar to that of NpO_2^+.

5.5.2 Plutonium redox

Plutonium has a very interesting chemistry, some [82] have even stated, "From physical, chemical, and technological perspectives, plutonium is one of the most complex and fascinating elements in the periodic table." From a chemistry standpoint, the fascination comes from the fact that Pu has accessible 5f orbitals that can involve themselves in bonding, while the redox chemistry is very diverse. Figure 33 shows the Latimer diagram [83] of the four common aqueous oxidation states and it can be seen that the redox potentials from one state to another are all very similar (roughly 1 V), and result in small changes in the standard Gibbs free energies between the species. Simply stated it only takes a small amount of energy for Pu to change from one oxidation state to

another, and in fact Pu is known to commonly undergo disproportionation reactions to exist in multiple oxidation states in a single solution or environment. In some cases all four aqueous states are present at one time [84].

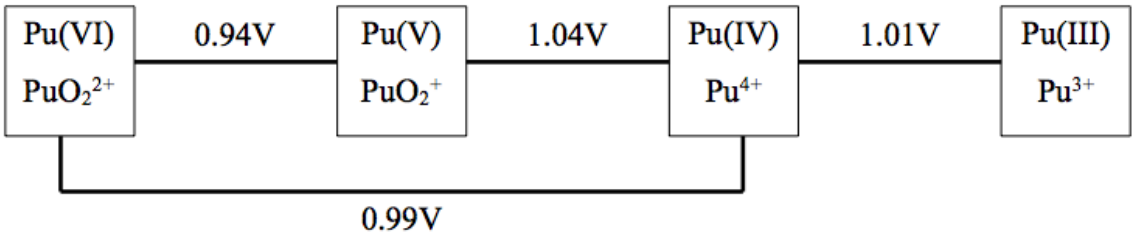

Figure 33: Latimer diagram for plutonium in 1 M perchloric acid [83].

There was an interest to observe what, if any, effect the exchange materials had on the oxidation state of Pu(VI) [79]. This is important because if any redox processes take place during or after sorption, the species will change and therefore the charge of the ion will change. If this change is charge occurs the K_d value would be misrepresentative of that reported in Table 26. To examine if any redox process occurred, 50 µL of concentrated HNO_3 was added to the sorption reactions to lower the pH roughly 0.5. The samples were shaken for 1 hour and the oxidation state was tracked by observing the solution absorption spectra between 400 and 900 nm (see Figure 34). The observation of a strong band at 830 nm is characteristic of Pu(VI) and the absence of bands at 569 nm (Pu^{V}) and 469 nm (Pu^{IV}) in all cases indicated no redox reactions occurring between the plutonium and the ion exchange materials. Other information can be gleaned from these experiments, in particular, the reversibility of the sorption for each ion exchange

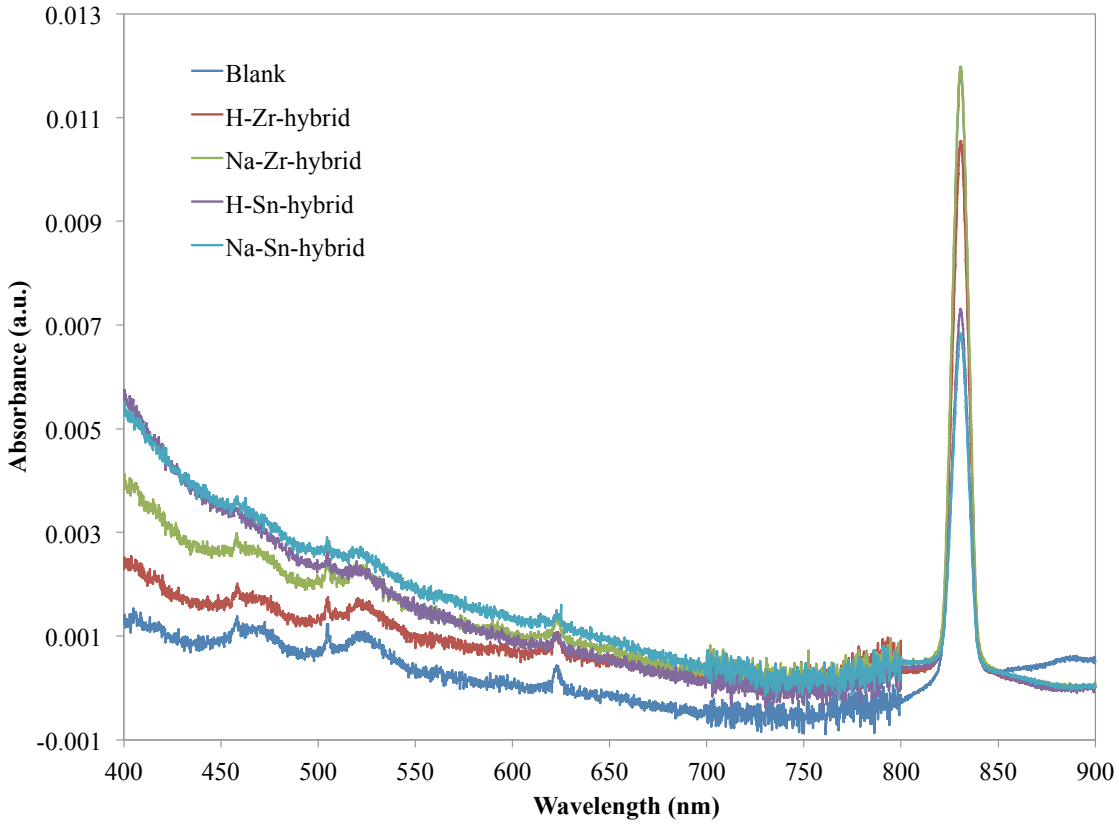

Figure 34: Absorption spectrum of PuO_2^{2+} after contact with ion exchanger material. Plutonium was washed from the hybrid material with HNO_3 pH 0.5. The blank is a control that was not interacted with the ion exchange material.

material. The fraction recovered can be determined by a comparison of the intensity of the absorption bands at 830 nm of the solution contacted with the ion exchangers and that of the solution not contacted with the ion exchangers (labeled as Blank), these comparisons are presented in Table 27. The sorption appears to be reversible by simple manipulation of the acid concentration, as stated earlier, and these results of the Pu(VI) desorption are in line with the previous neodymium studies as a function of acidity (see Section 5.4 Figure 31).

Table 27: Absorbance of PuO_2^{2+} at 830 nm after being striped from ion exchange material.

Sample	Wavelength (nm)	Abs	Recovery
Blank	830	0.0120	-
H–Zr–hybrid	830	0.0105	87%
Na–Zr–hybrid	830	0.0120	100%
H–Sn–hybrid	830	0.0073	60%
Na–Sn–hybrid	830	0.0068	57%

5.5.3 Americium oxidation

It is well known that the actinides can be broken up into two distinct groups, light and heavy. The heavy An, curium and above, are primarily trivalent cations and behave very similarly to the analogous lanthanides, while the light An, thorium through plutonium, are more transition metal-like in their electronic properties. Americium however, acts as a bridge between the two: in natural conditions Am is a trivalent cation like the heavy An, but in strongly oxidizing conditions it can exist in higher oxidation states (V/VI).

For the interested reader a recent review article has just been published on the higher oxidation states of Am [85]. Only a handful of reports have been published discussing the synthesis and stabilization of oxidized Am [86-99]. In acidic media, pentavalent americium is highly unstable and readily reduces to Am(III). Magirius *et al*. [95] reported the quantitative radiolytic oxidation of ^{241}Am(III) to ^{241}Am(V) in 5 M NaCl within a week under slightly basic conditions. They proposed the radiolytic generation of OCl^- from the brine, which then initiates the oxidation of Am. Under acidic conditions (pH $\leq$ 2) hypochlorite does not appear to be a strong enough oxidant to convert Am(III) to Am(V), as we saw no change in the absorbance spectra of Am^{3+} with just the addition of $Ca(OCl)_2$. However, when $Na_2S_2O_8$ is introduced to the Am solution and heated to 80 ºC the intensities of the Am(III) characteristic bands at 503 nm and 806 nm decreased, while the characteristic bands for Am(VI) at 666 nm and 996 nm grew in as previously reported [97-99]. After 30 minutes at temperature the bands for Am(III) completely disappear and the bands for Am(VI) reached a maximum. If the solution is allowed to cool Am(VI) immediately begins to reduce to Am(V) and subsequently to Am(III) and upon reheating is converted back to the hexavalent state. However, if OCl^- is added to the solution while it is still warm, Am(V) is synthesized in $\geq$ 97% yield with trace amounts of Am(III) present. As shown in Figure 35, if there is only a slight excess of hypochlorite, as it is consumed either by redox or degradation processes, Am(V) begins to reduce to Am(III). The Am(III) band at 503 nm grows in at a constant rate over 60 hours, while there is only a slight decrease in the Am(V) band at 514 nm. The

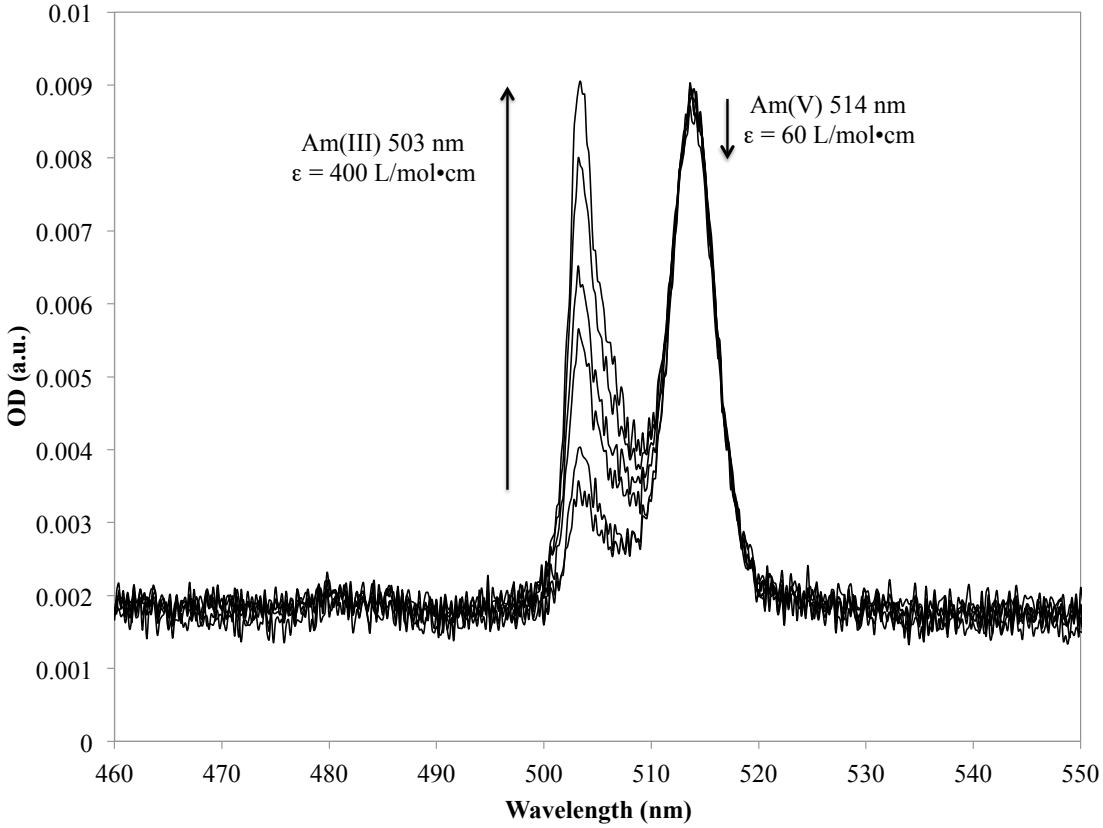

Figure 35: Ingrowth of Am(III) over time 0 hours to 60 hours as OCl^- is consumed.

asymmetric tail of the Am(III) 503 nm band, which extends past 514 nm, causes the near constant intensity of the Am(V) band.

When OCl^- is in large excess there was no observable change in the ratio Am(V) to Am(III) after 24 hours, with an ingrowth of only ≤ 10% Am(III) at 48 hours. It is believed at this time the mechanism of oxidation of Am(III) to Am(V) first requires the formation of a highly oxidizing radical, in this case $SO_4^{\bullet-}$, which produces Am(VI). Generation of the $SO_4^{\bullet-}$ requires enough energy for the O–O bond to cleave (≤ 80 ºC). In order to produce Am(V) with a long enough lifetime to be observed or used, a stabilizing agent of moderate oxidizing strength must be present to allow Am(VI) to reduce to Am(V) without further reduction, *e.g.* hypochlorite. Am(V) should persist as long as there is an excess of the stabilizing agent present. To our knowledge this is the first report of using a mixture of persulfate and hypochlorite to synthesize and stabilize Am(V).

The above findings [100] and subsequent discussion were a result of research collaboration with Dr. Donald T. Reed and Dr. Marian Borkowski at Los Alamos National Laboratory-Carlsbad Operations (LANL-CO) who invited me to the Carlsbad Environmental Monitoring and Research Center (CEMRC) located in Carlsbad, NM to perform the actinides studies. The oxidation of americium was performed in ~ 1 M perchloric acid. Following this success I was invited to go and work with Dr. David T. Hoobs and Dr. Thomas C. Shehee at Savannah River National Laboratory (SRNL)

located in Aiken, SC. Our aim was to reproduce americium oxidation and conduct a separation of Am from Cm. However, as life continually reminds us, not everything goes according to plan. In the purification process of the on-hand Am stock at SRNL, our working stock ended up being 0.01 M nitric acid [101]. In the work at SRNL, we were able to significantly increase the stability of the AmO_2^+ species from the work done at LANL-CO, with a lifetime of at least 48 hours ~ 10 % ingrowth of Am^{3+}, to only ~ 5% ingrowth after 5 days by changing the matrix to nitric acid from perchloric acid [100]. Our finding showed that there are several key differences in the oxidation of americium when the matrix is HNO_3 rather than $HClO_4$, and this was verified by repeating the original studies performed at CEMRC at SRNL in 0.01 M $HClO_4$. The most notable difference is the oxidation products resulting from the sulfate radical oxidation, AmO_2^+ and AmO_2^{2+} in nitric acid and perchloric acid, respectively. The nitric acid is limiting to Am(V), while the perchloric acid allows for the americium to reach the hexavalent state. This difference is most likely caused by the evolution of the reducing agent nitrite upon heating the HNO_3 system. Both systems require an excess of OCl^- in order to stabilize and maintain Am in the pentavalent state. In nitric acid, 17 hours after the $Ca(OCl)_2$ addition, nice colorless crystals form that appeared to be monoclinic, presumably gypsum ($CaSO_4 \bullet 2H_2O$). After filtering and inspecting the spectrum, presented in Figure 36, the solution was absent of the trace amounts of Am^{3+} seen immediately after synthesis of AmO_2^+, but there was no visible decrease in the amount of Am(V) present. The Am^{3+} undoubtedly co-precipitated with the gypsum, resulting in a very pure AmO_2^+ solution [97]. In perchloric acid no precipitation was

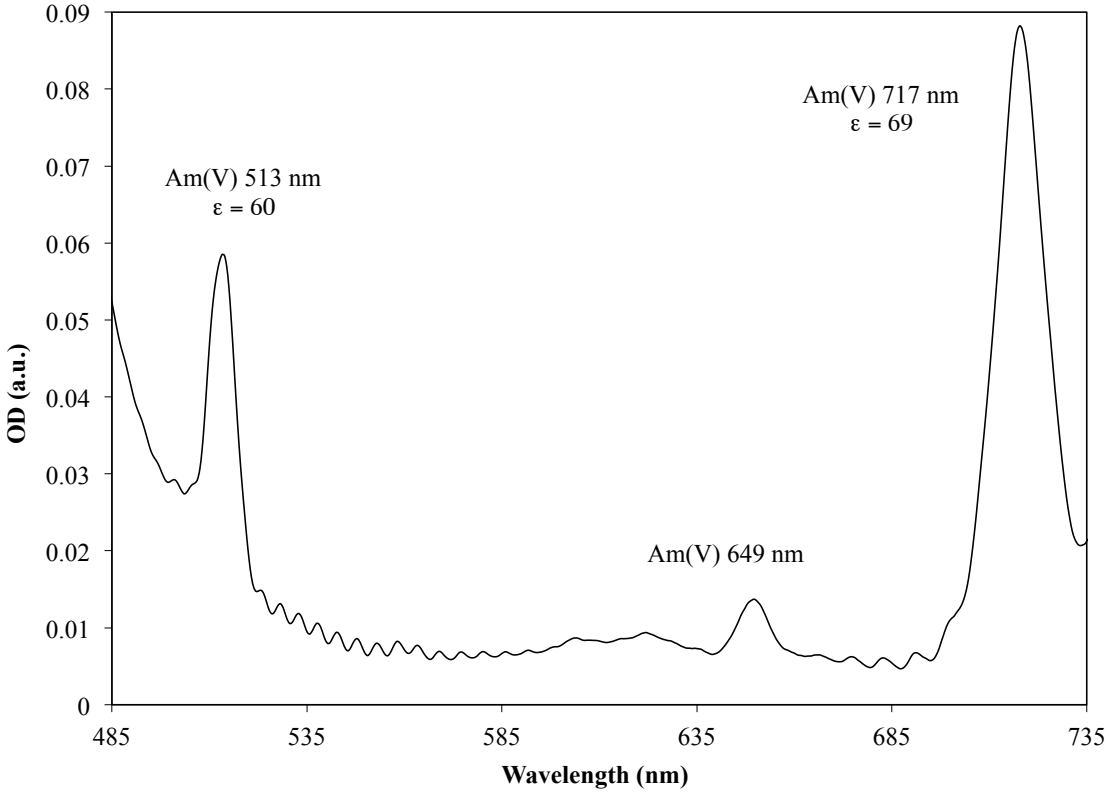

Figure 36: Spectrum of pure AmO_2^+ in 0.01 M HNO_3 after solution was allowed to age resulting in precipitation of $CaSO_4$ and co-precipitation of any Am^{3+} not oxidized.

observed even up to 5 days, at either 0.1 M or 0.01 M concentrations. These two results are very interesting, as they provide tools to control the oxidation and speciation of actinides, allowing for a diverse set of experiments. If the chemistry is pH sensitive, the *in situ* generated sulfate buffer system may be advantageous and therefore the perchloric matrix should be used; however, if a simple environment is desired that resembles more closely an ideal system, the nitrate matrix can be aged, allowing the majority of the calcium sulfate to precipitate, leaving in solution AmO_2^+, OCl^-, and small amounts of ClO_x^- from the decomposition of the hypochlorite.

5.5.4 Challenges in americium oxidation

Developing a new method of oxidizing americium was not the original goal in the process of producing the higher oxidation states of Am. The first attempt made was to reproduce the work of Mincher *et al.*, employing sodium bismuthate as an oxidizing agent to oxidize Am(III) to either Am(V) or Am(VI) [96]. This, however, proved to be unfruitful. The following is an account of experimental procedure and results followed by an explanation of what is believed to have taken place.

Mincher *et al.* first reported that Am(III) could be oxidized to either Am(V) or Am (VI) by simply shaking a solution of Am with an excess of $NaBiO_3$ at either 80 or 25 ºC, respectively. In both cases the conversion was reported to be quantitative and oxidation states to be pure. For our systems it was important to use an excess of $NaBiO_3$, because

these experiments were to be performed in triplets. So, extra $NaBiO_3$ was added to the solution of Am(III) to ensure that each sorption reaction would have excess solid $NaBiO_3$. The procedure was carried out as follows: 1 g of $NaBiO_3$ along with 2 mL of ~ 1×10^{-4} M $^{243}Am^{3+}$ was added to a 30 mL high-density polyethylene bottle with a screw cap. The container was sealed and placed in an 80 ºC water bath for 4 hours. The solution was filtered and upon investigation of the oxidation state by means of the absorption spectroscopy, no americium was observed! The Am was not in the solution, so it must have been in the solid phase. There are two obvious reasons this could have happened: 1) the Am precipitated, or 2) the Am sorbed to the bismuthate. The Am solution was ~ 0.1 M $HClO_4$, so it was unlikely that any precipitate formed. With the excess of $NaBiO_3$ it was very possible that sorption took place. To test this hypothesis two experiments were designed. 40 mg of $NaBiO_3$ was weighed out and 2 mL of pH 2 Am^{3+} or Nd^{3+} solution was added (the rest of the experiment was performed following the general K_d determination procedure, see Chapter II Section 2.5). K_d values for the bismuthate were observed to be 1,000 ± 5.6 and 340 ± 2.4 mL g^{-1} for Nd^{3+} and Am^{3+}, respectively ($[Nd^{3+}]_I \sim 2.9 \times 10^{-4}$ M, $[Am^{3+}]_I \sim 6.2 \times 10^{-5}$ M). These results were conclusive that Am had sorbed to the bismuthate, and therefore, was not detected in the solutions. Following these results the Am was stripped from the 1 g of bismuthate by adding 4 M HNO_3. No oxidation was observed for the stripped Am, however the solid bismuthate underwent a color change from a light brown to a dark auburn red. This color change is believed to be due to a decomposition of the bismuthate to one of the

bismuth oxide phases. This decomposition is not surprising, as it is well know that bismuthate decomposes in acid [102-104].

The oxidation was attempted a second time on a smaller scale inside a sealed cuvette, so the reaction could be tracked by UV-Vis spectroscopy in real time. To perform this experiment 1 mL of ~ 1 $\times 10^{-5}$ M Am^{3+} and 10-20 mg of $NaBiO_3$ were added to the cuvette; the Am^{3+} solutions were ~ 0.1 M $HClO_4$. The cuvette was sealed by means of a screw cap and placed in the spectrometer. An initial spectrum from 400-1100 nm was obtained before the addition of bismuthate, and again as quickly as possible after the addition of the bismuthate. These two scans showed no observable change in [Am^{3+}], however over time there was slight decrease in absorbance in the band at 503 nm with no growth of other bands. Most certainly, this reduction of intensity in the 503 nm band is a result of Am^{3+} sorption to the surface the bismuthate. Once the band height stabilized, meaning no further decrease was detected, the cell was heated in the spectrometer to 80 ºC and scans were taken every 10 minutes. The quality of the spectra were very poor while heating; the elevated temperature increased the rate of decomposition of the bismuthate, which generates O_2 (see Equation 7). The O_2 evolution agitated the solid and increased particulate suspension in the solution. Other than the poor quality of the spectra the only noticeable change was a slight increase in intensity of the 503 nm band, presumably caused by the release of Am^{3+} as the BiO_3^- decomposed to Bi_2O_3. Upon visual inspection of the cuvette the solid had turned white, providing further evidence of the formation of the oxide.

$$4\ NaBiO_3 + 2\ H_2O \xrightarrow{\Delta} 2\ Bi_2O_3 + 4\ NaOH + 2\ O_2 \quad (7)$$

Other attempts were made at a lower temperature of 60 ºC, in hopes that the bismuthate would decompose slower and allow for oxidation to take place. In every attempt concerning that bismuthate no oxidation was observed. To the best of our knowledge, we reproduced the reported experimental conditions, but were unable to achieve the reported results.

As an aside, I have had several conversations with Bruce Mincher since the unsuccessful bismuthate oxidation, and he has suggested several possibilities as to why we were unable to reproduce his findings. The most likely of which is that one of the byproducts of $NaBiO_3$ synthesis is peroxide, but most manufactures do not report this in their assay of the chemical. The presence of peroxide will most certainly prevent Am oxidation. As a result of our conversations, Mincher has contacted the manufacture from which he purchased the bismuthate and they have agreed to prepare the $NaBiO_3$ with the lowest amount of peroxide possible. Mincher will test this 'peroxide-free' bismuthate to determine what effect the peroxide has on the oxidation system.

5.6 Separations

Single ion measurements help in predicting separation factors (SF's), but there is no substitute for a direct measurement of affinity in a mixed ion system. To this end, several mixed ion systems have been investigated and experimental separation factors have been calculated. These systems include intergroup studies of lanthanide and alkali metals, lanthanide and alkaline earth metals, lanthanide and transition metals, and lanthanide and actinide metals as well as intragroup separations of a variety of lanthanides.

The SF's of Ln and mono- or divalent ions using alkali, alkaline earth, and transition metals were observed in several mixed ion systems: Cs^{+} / Nd^{3+}, Sr^{2+} / Nd^{3+}, and Ni^{2+} / Nd^{3+} [101]. The K_d values and SF's are presented in Table 28, Table 29, and Table 30; and the experimental conditions for these studies are presented in Chapter II Section 2.5.1. These results correlate with the single ion studies: the more highly charged neodymium ion sorbs much more readily than the ions of lower charge namely cesium, strontium and nickel(II). Separation factors are observed in the hundreds in most cases and as high as the thousands in all three systems. Not only do these results reveal the fact that group separations can be performed on the basis of charge, but more importantly they show the effects of steric hindrance are negligible in comparison to the coulombic driving force. This will become important later in the discussion of the larger dioxo americium(V) multi-ion studies.

Table 28: K_d values (in mL g^{-1}) and separation factors (SF) of Nd^{3+} from Cs^+ at pH 2.

Sample	K_d Nd^{3+}	K_d Cs^+	SF Nd^{3+} / Cs^+
H–Zr–hybrid	1,190 ± 30	79 ± 3	15 ± 1
Na–Zr–hybrid	29,000 ± 8,000	370 ± 50	80 ± 20
H–Sn–hybrid	25,600 ± 800	89 ± 5	290 ± 18
Na–Sn–hybrid	71,500 ± 300	89 ± 5	800 ± 50

Table 29: K_d values (in mL g^{-1}) and separation factors (SF) of Nd^{3+} from Sr^{2+} at pH 2, where <1 indicates no observable change in [M].

Sample	K_d Nd^{3+}	K_d Sr^{2+}	SF Nd^{3+} / Sr^{2+}
H–Zr–hybrid	1,600 ± 300	<1	> 1,000
Na–Zr–hybrid	131,000 ± 8,000	<1	> 100,000
H–Sn–hybrid	31,900 ± 1,100	17 ± 2	1,900 ± 200
Na–Sn–hybrid	84,000 ± 2,000	35 ± 4	2,400 ± 300

Table 30: K_d values (in mL g^{-1}) and separation factors (SF) of Nd^{3+} from Ni^{2+} at pH 2.

Sample	K_d Nd^{3+}	K_d Ni^{2+}	SF Nd^{3+} / Ni^{2+}
H–Zr–hybrid	430 ± 30	30 ± 16	14 ± 8
Na–Zr–hybrid	50,000 ± 5,000	100 ± 30	500 ± 200
H–Sn–hybrid	53,000 ± 8,000	58 ± 7	900 ± 200
Na–Sn–hybrid	111,000 ± 12,000	110 ± 30	1,000 ± 300

Other intragroup separation studies were performed with a mixture of four Ln's: Nd, Sm, Ho, and Yb. In this experiment the pH was varied from 1.0, 1.5, 2.0, 2.5, and 3.0. The K_d values are presented in Figure 37, Figure 38, Figure 39, Figure 40, and Figure 41, respectively. There appears to be very little to no discrimination between the four lanthanides for any of the hybrid exchangers as a function of pH. There is a slight preference for the heavier lanthanides at a pH of 1 for the Na–Zr–hybrid, however with

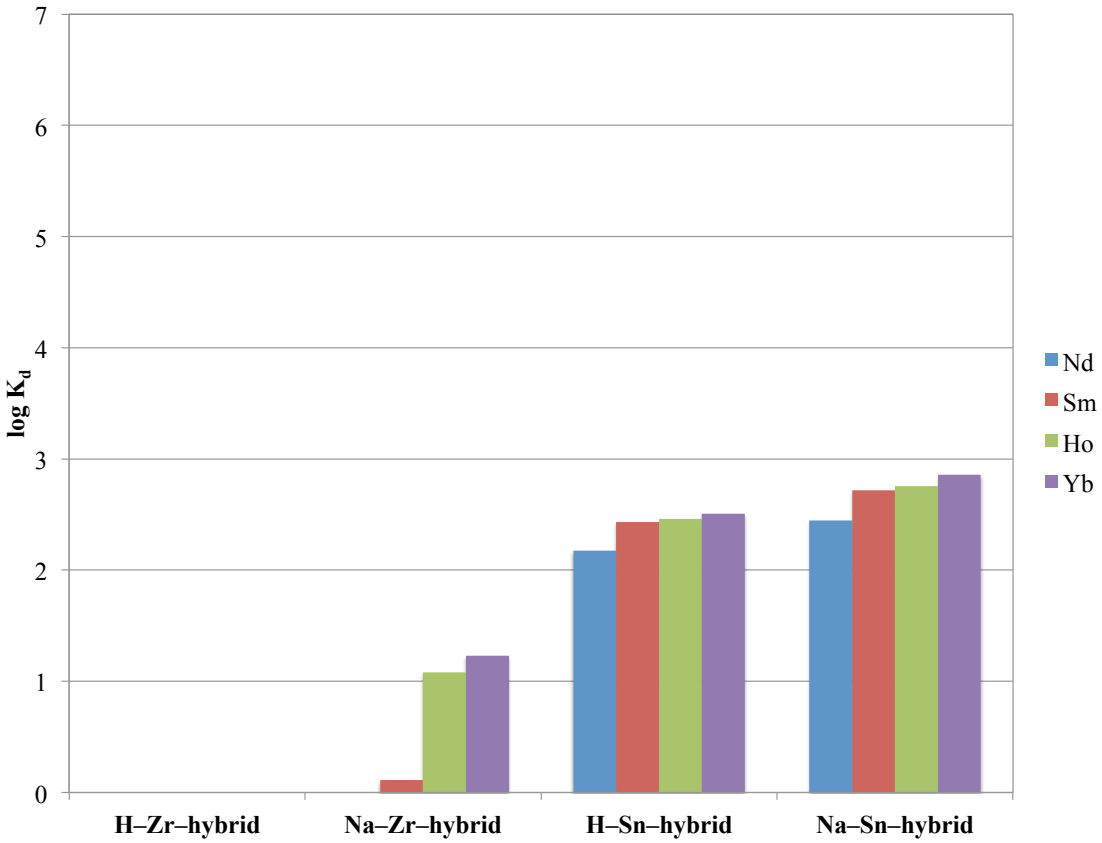

Figure 37: Multi-ion uptake of select lanthanide ions at pH 1.0, K_d reported in mL g^{-1}. Estimated error < 5%.

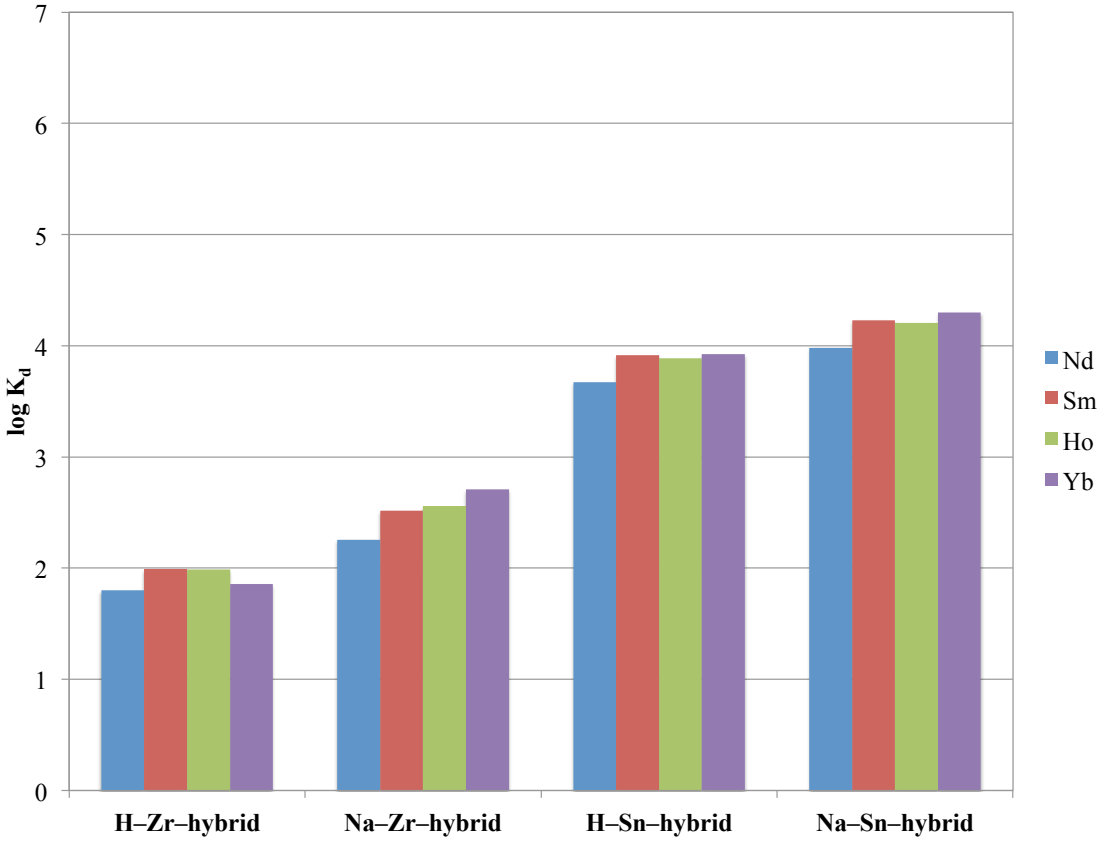

Figure 38: Multi-ion uptake of select lanthanide ions at pH 1.5, K_d reported in mL g^{-1}. Estimated error < 5%.

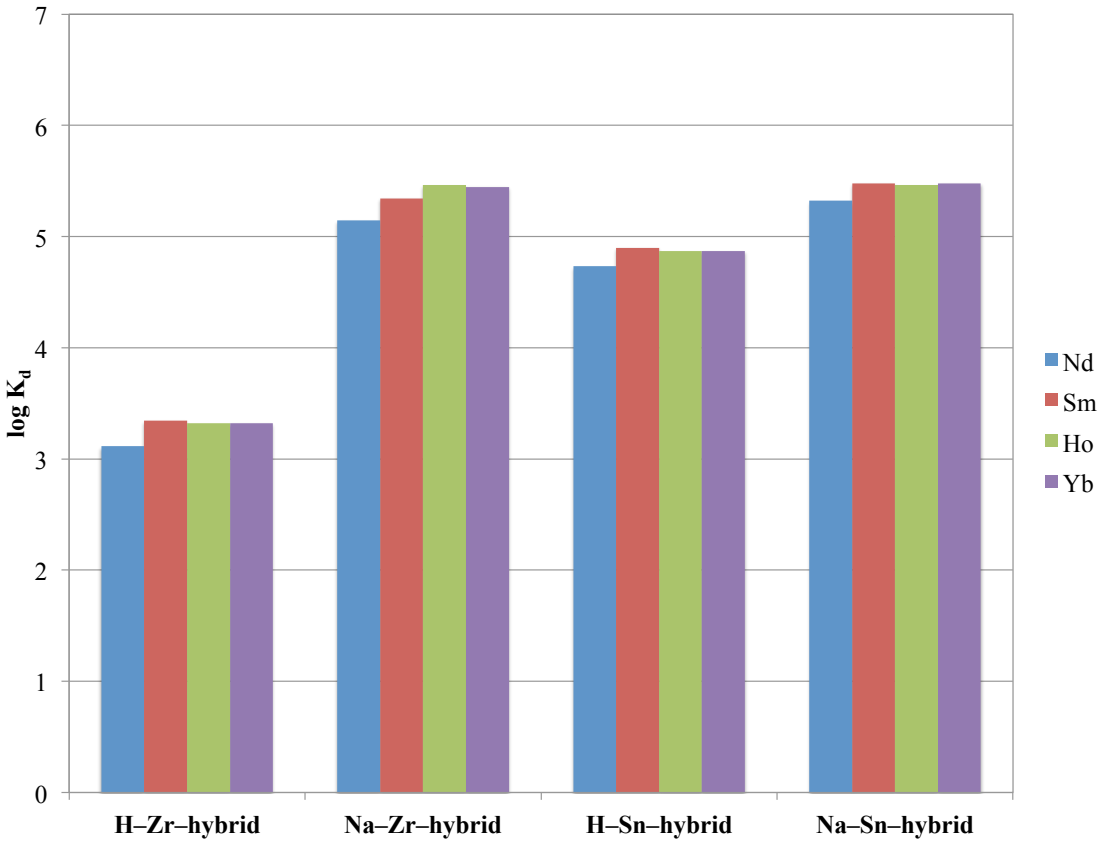

Figure 39: Multi-ion uptake of select lanthanide ions at pH 2.0, K_d reported in mL g^{-1}. Estimated error < 5%.

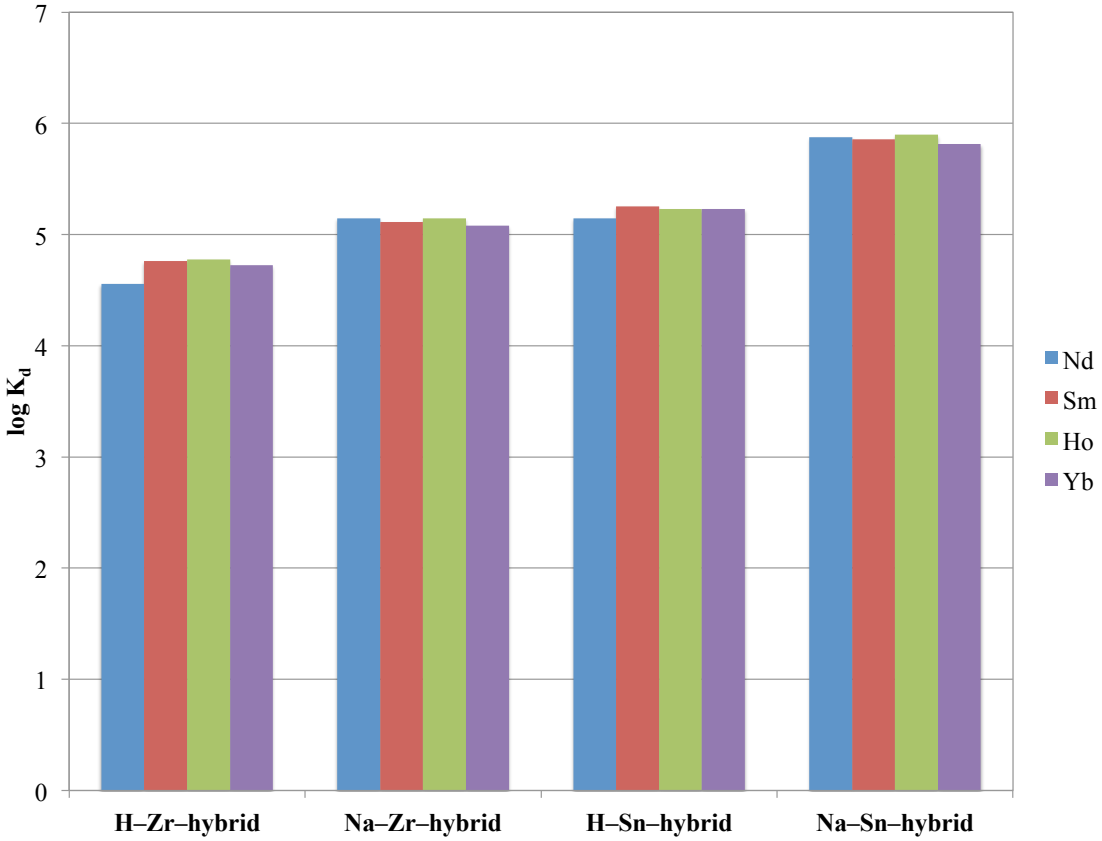

Figure 40: Multi-ion uptake of select lanthanide ions at pH 2.5, K_d reported in mL g^{-1}. Estimated error < 5%.

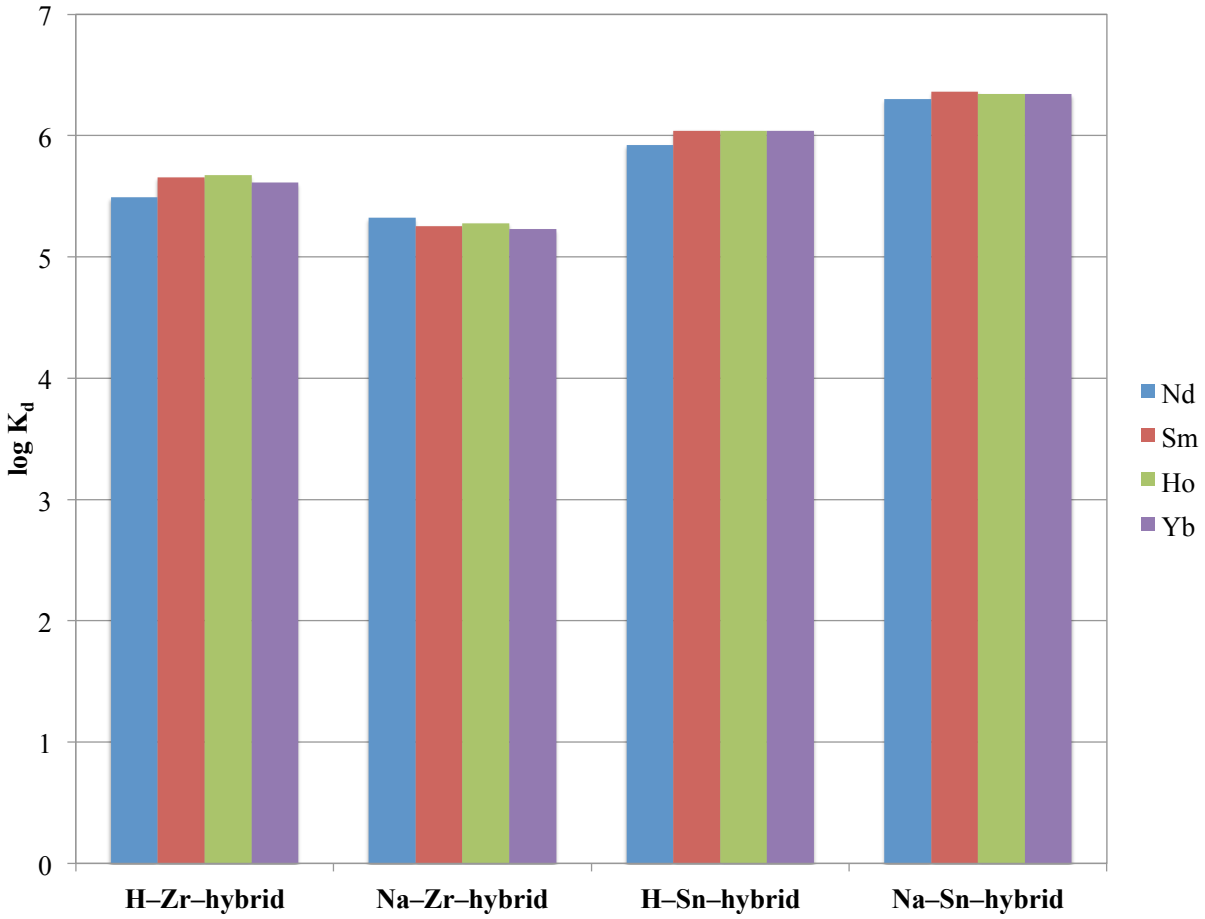

Figure 41: Multi-ion uptake of select lanthanide ions at pH 3.0, K_d reported in mL g^{-1}. Estimated error < 5%.

such a low K_d value for the preferred Ho^{3+} and Yb^{3+}, roughly 12 and 17 mL g^{-1}, respectively, this separation is not very efficient. Contrary to what was previously hypothesized there appears to be no size discrimination across the lanthanide series, preventing an intragroup separation of the lanthanides using these ion exchangers.

The last and most important separations observed were those of a Ln / An mixed ion system. A mixed ion system was created to directly observe separation between the different An species and Nd^{3+}, the results of which are summarized in Table 31. ICP-MS data were unable to be obtained for the NpO_2^+ and PuO_2^{2+} systems, so only the difference in activity of solutions in the presence and absence of Nd^{3+} will be discussed. There is a noticeable reduction in the K_d value for NpO_2^+ with all four materials upon introduction of Nd^{3+} into the system, as high as 56% for the Na–Zr–hybrid down to 26% for the H–Sn–hybrid. Nd^{3+}, like Am^{3+}, has a significantly higher Z_{eff} than NpO_2^+ and so the K_d value was expected to decrease upon the addition of Nd^{3+} into the system. The Na–Zr–hybrid was also investigated for purposes of separating PuO_2^{2+} and Nd^{3+}, due to its high affinity for PuO_2^{2+} [79]. It can be seen, as expected from the Z_{eff}, the K_d is only very slightly reduced indicating a separation factor for PuO_2^{2+} and Nd^{3+} very close to unity. These simple two ion systems revile interesting separation properties of the hybrid ion exchange materials, Nd^{3+} cannot be separated from PuO_2^{2+}, but it can be separated from NpO_2^+. By analogy, PuO_2^{2+}, like Nd^{3+}, can be separated from NpO_2^+ and therefore should be able to be separated from AmO_2^+.

Table 31: The K_d values (in mL g^{-1}) for the M(IV) hybrid exchangers after Nd^{3+} was introduced into the actinide systems.

Sample	K_d AmO_2^+ / Nd^{3+} / Eu^{3+} pH 1.99	K_d PuO_2^{2+} pH 1.95	K_d NpO_2^+ pH 2.10
H–Zr–hybrid	5 ± 2 / 36 ± 2 / 80 ± 12	-	55 ± 2
Na–Zr–hybrid	17 ± 2 / 181 ± 5 / 658 ± 2	215,000 ± 15,000	1,400 ± 300
H–Sn–hybrid	19 ± 2 / 295 ± 3 / 662 ± 7	-	166 ± 3
Na–Sn–hybrid	19 ± 3 / 630 ± 20 / 1,150 ± 20	-	330 ± 20

The results from the pentavalent americium studies require a more critical examination, as the electrolyte system is much more complex and, as mentioned earlier, the impact of the carrier is more significant. In all other ion sorption studies the electrolyte mixture was made up of either nitrate or perchlorate as counter anions and minimal amounts of sodium originating from NaOH added for pH adjustments, all three of which are assumed to be non-interactive. Remember that ion exchange is a charge neutral process, so upon sorption the ion should be completely disassociated from the counter cations (both NO_3^- and ClO_4^- are very non-complexing themselves); while the affinity for Na^+ is negligible at pH ≤ 3. In the case of AmO_2^+ there are a variety of species present because they were required for synthesis and stabilization purposes, including $S_2O_8^{2-}$, SO_4^{2-}, OCl^-, as well as ClO_x^- generated from the decomposition of the hypochlorite. All these species are believed to have little effect on the ion exchange processes themselves, but persulfate and sulfate serve to generate an *in situ* buffer, which has the potential to affect the sorption of the metals and therefore affect the K_d values. Figure 32 illustrates the equilibrium of sorption in acidic media for the M(IV) hybrids, which is highly dependent upon pH. The impact of the buffer should result in a more accurate value because it will

reduce the difference in pH_I and pH_{Eq}. Despite the generation of the buffer, the existence of the Eu carrier used in manufacturing should have the most significant impact in the sorption of AmO_2^+. This is assumed to be the explanation for the almost identical K_d values before and after introduction of Nd^{3+} to the system. Moreover, the K_d values associated with neodymium are reduced due to the increase in population of trivalent ions and the lower pH. With all this being said, in the mixed ion system of AmO_2^+, Nd^{3+}, and Eu^{3+} the K_d values were obtained and separation factors calculated (see Table 31 and Table 32). Taking into account the complex system required for synthesis of AmO_2^+, these SF indicate the potential for a practical Am / Cm separation, which will be discussed next.

Table 32: Observed separation factors calculated from data in Table 31 at pH 1.99.

Sample	AmO_2^+ / Nd^{3+}	AmO_2^+ / Eu^{3+}
H–Zr–hybrid	7 ± 2	16 ± 7
Na–Zr–hybrid	11 ± 1	39 ± 5
H–Sn–hybrid	16 ± 2	35 ± 4
Na–Sn–hybrid	33 ± 5	60 ± 10

Traditionally the separation of Am from Cm has been a very difficult problem to tackle because of their very similar chemical properties that require complex solvent extraction systems [105-107] using exotic ligands or chromatography [108-111] that depend on organic resins, which are highly susceptible to radiolydic degradation. As was discussed earlier, the inorganic hybrid materials, which are the focus of this dissertation, show increased affinity for highly charged cations [79], which resulted in a separation of

americium from neodymium and europium. Using the same procedure of oxidation, stabilization, and ion exchange, americium can be separated from curium (see Table 33) [101]. The K_d values for AmO_2^+ were observed to be slightly higher than what was observed in the separation of AmO_2^+ from Nd^{3+} and Eu^{3+} and is believed to be a result of performing the oxidation in nitric acid and not allowing the $CaSO_4$ to precipitate out prior to contact with the ion exchange materials. In other words, the $CaSO_4$ may have precipitated during the incubation time, allowing co-precipitation of some Am or Cm. This precipitation effect was discussed earlier (see Section 5.5.3). Unfortunately, due to the limited availability of radiological laboratory space and time, both the americium stability and Am-Cm separation experiments had to be run in parallel, so the $CaSO_4$ precipitation results from the stability experiments were not compensated for in the Am-Cm separation experiments. It should be noted that the Na–Sn–hybrid removed ~ 98% of the Cm^{3+} out of solution, leaving almost pure Am in solution. As a side note, the Ca^{2+} concentration was tracked by ICP-MS as well for the Na–Sn–hybrid and a K_d value of 3.1 ± 0.3 was observed. This reaffirms the single ion studies and confirms that the counter cations found in the oxidation system do not interfere with sorption of trivalent species of interest, in this case Cm^{3+}. The charge discrimination of these ion exchange materials makes them very interesting and unique to classic ion exchange materials; the inability of Na^+ or even Ca^{2+} to sorb provides a useful tool for a separation that involves oxidized Am(V).

Table 33: K_d values (in mL g^{-1}) and separation factors (SF) of Cm^{3+} from AmO_2^+ at pH 2.05.

Sample	K_d AmO_2^+ / Cm^{3+}	SF Cm^{3+} / AmO_2^+
H–Zr–hybrid	62 ± 6 / 100 ± 10	1.6 ± 0.2
Na–Zr–hybrid	85 ± 8 / 1,300 ± 100	15 ± 2
H–Sn–hybrid	120 ± 10 / 1,600 ± 200	13 ± 1
Na–Sn–hybrid	220 ± 20 / 4,400 ± 400	20 ± 3

5.7 Conclusions

The four bulk hybrid inorganic/organic ion exchange materials can be synthesized and used for the separations of species based on charge. It was shown that these materials behaved as expected, judging from the results in the previous two chapters. They possess very desirable attributes of mild synthetic routes, high thermal stability, high surface areas with large microporosities, and participation in ion exchange.

The ion exchange properties, display very interesting selectivity for highly charged ions (≥ 3+), while almost completely discriminating against ions that are singly or doubly charged. In single ion studies the alkali and alkaline earth metals have very low K_d values; within error Na^+ shows no affinity toward the ion exchangers and Ca^{2+} is only slightly higher. The trivalent lanthanides on the other hand, are readily sorbed and are completely removed from the solution at pH 3 with a phase ratio of 250–500 mL g^{-1}. The actinides behaved accordingly with respect to oxidation state and respective ion species; with an increasing affinity as follows $AnO_2^+ << AnO_2^{2+} \leq An^{3+} < An^{4+}$. It

should be remembered that the formal charge and effective charge of An metals are not equal and so PuO_2^{2+} and Am^{3+} both have a Z_{eff} of 2.9 charge units and similar K_d values.

Despite the challenges in americium oxidation in aqueous acidic media a method has been developed that employs sodium persulfate as an oxidizing agent and calcium hypochlorite as a stabilizing agent. Of course, this is not without adversity either; concerns of sulfate precipitation and hypochlorite stability are paramount. In our work, we found that Am(V) is stable up to at least 5 days as long as OCl^- is present and presumably longer times with the addition of fresh hypochlorite source.

The multi ion studies show definitively that intergroup separations can be made. The lanthanides are sorbed in competition with group 1, group 2, and a transition divalent metal, resulting in separation factors in the hundreds and even reaching the thousands in some select cases. The most important implication of these results is that the driving force for these separations is not based on sterics, but rather primarily on the charge state of the specific ions in the system. This was further observed in the intragroup separation studies of Nd^{3+}, Sm^{3+}, Ho^{3+}, and Yb^{3+} where there was little to no discrimination of one Ln to another, or even light to heavy Ln's. Some small discriminations were observed at low pH's, but those were accompanied with very low K_d values and would require some sort of chromatography to achieve a separation, if at all possible.

Lanthanides can be separated from actinides using these hybrid ion exchange materials, but this requires controlling the oxidation state of the An in a very strict manner, and is best accomplished when AnO_2^+ is the dominate actinide species. For certain An, like neptunium, this is less of an obstacle, but for plutonium and especially for americium this proves to be a more rigorous task. In simple systems where only Am and one or two non-redox active species are present (Nd^{3+}, Eu^{3+}, or Cm^{3+}) a separation can be achieved using the $Na_2S_2O_8$ / $Ca(OCl)_2$ oxidation system. The conditions have not been optimized, however, SF's were seen around 60 and 20 for the Am(V)-Ln and Am(V)-Cm, respectively. As mentioned earlier, in these studies the trivalent ions were almost quantitatively removed from solution leaving pure Am behind. This is a great success in the field of nuclear fuel cycle separations. These ion exchange materials show significant promise in the challenging separations needed in the harsh environment of the back end of the nuclear fuel cycle.

CHAPTER VI

SUMMARY AND

FUTURE WORK

The previous five chapters have shown the development and usefulness of these M(IV) phosphate phosphonate inorganic organic hybrid ion exchange materials. The zirconium-based materials (Chapter III) are similar to their tin based analogs (Chapter IV), but the two have some distinct differences including pore structure. Both types of materials have desirable properties with respect to closing the nuclear fuel cycle, with mild synthetic routes, high thermal stability, large surface areas, high microporosity, and ion exchange properties. The ion exchange properties of these hybrid materials (Chapter V) are very interesting, as they are discriminatory towards ions of low charge, but possess increased affinity towards ions of high charge ($\geq$ 3+). The ion exchange properties allow for intergroup and intragroup separations to be realized based on charge.

While there are still many directions this research could go, one interesting course would be to change the active site in the materials away from the hard oxo binding site to a softer thiol or amine binding site. The actinides, while they are still fairly hard metals, are well known to be significantly softer than their lanthanide counter parts [113-117]; and have been shown to complex much more readily to soft donor ligands. There are a number of ways this could potentially be done; one is to increase the interlayer distance

by changing the pillar to a biphenyldiphonsphonate to accommodate changing the spacer ligand to a short chain thiolphosphonate or aminephosphonate. Another way is to use an inert spacer ligand, like methylphosphonate, and bipyridyldiphosphonate. Along these lines, materials possessing two different active sites with different functionalities could be investigated. These types of materials could lend themselves to utility in more areas than just the nuclear fuel cycle, but could be useful in a wide range of separations.

REFERENCES

[1] L. Gagnon, C. Belanger, Y. Uchiyama, Life-Cycle Assessment of Electricity Generation Options: The Status of Research in Year 2001, Energy Policy, 30 (2002) 1267-1278.

[2] K.L. Nash, G.J. Lumetta, S.B. Clark, J. Friese, Significance of the Nuclear Fuel Cycle in the 21st Century, in: Separations for the Nuclear Fuel Cycle in the 21st Century, American Chemical Society, Washington, DC, 2006, pp. 3-20.

[3] S.J. Davis, K. Caldeira, H.D. Matthews, Future CO_2 Emissions and Climate Change from Existing Energy Infrastructure, Science, 329 (2010) 1330-1333.

[4] A.F. Ghoniem, Needs, Resources and Climate Change: Clean and Efficient Conversion Technologies, Prog. Energy Combust. Sci., 37 (2011) 15-51.

[5] M.I. Hoffert, K. Caldeira, G. Benford, D.R. Criswell, C. Green, H. Herzog, A.K. Jain, H.S. Kheshgi, K.S. Lackner, J.S. Lewis, H.D. Lightfoot, W. Manheimer, J.C. Mankins, M.E. Mauel, L.J. Perkins, M.E. Schlesinger, T. Volk, T.M.L. Wigley, Advanced Technology Paths to Global Climate Stability: Energy for a Greenhouse Planet, Science, 298 (2002) 981-987.

[6] http://www.world-nuclear-news.org/WR-US_utilities_regulators_sue_DoE_over_waste_fund-0604108.html

[7] http://www.world-nuclear-news.org/WR-Xcel_recovers_used_fuel_storage_costs-1107114.html

[8] http://www.world-nuclear-news.org/WR-US_utility_wins_45.5_million_spent_fuel_settlement-2202117.html

[9] R.G. Anthony, C.V. Philip, R.G. Dosch, Selective Adsorption and Ion Exchange of Metal Cations and Anions with Silico-Titanates and Layered Titanates, Waste Manage., 13 (1993) 503-512.

[10] A. Clearfield, D.G. Medvedev, S. Kerlegon, T. Bosser, J.D. Burns, M. Jackson, Rates of Exchange of Cs^{+} and Sr^{2+} for Poorly Crystalline Sodium Titanium Silicate (CST) in Nuclear Waste Systems, Solvent Extr. Ion Exch., 30 (2012) 229-243.

[11] W.J. Paulus, S. Komarneni, R. Roy, Bulk Synthesis and Selective Exchange of Strontium Ions in $Na_4Mg_6Al_4Si_4O_{20}F_4$ Mica, Nature, 357 (1992) 571-573.

[12] J.M. Zachara, S.C. Smith, C.X. Liu, J.P. McKinley, R.J. Serne, P.L. Gassman, Sorption of Cs^{+} to Micaceous Subsurface Sediments from the Hanford Site, USA, Geochim. Cosmochim. Acta, 66 (2002) 193-211.

[13] J.K. Bates, J.P. Bradley, A. Teetsov, C.R. Bradley, M.B. Tenbrink, Colloid Formation During Waste Form Reaction - Implications for Nuclear Waste-Disposal, Science, 256 (1992) 649-651.

[14] E.P. Horwitz, M.L. Dietz, R. Chiarizia, H. Diamond, S.L. Maxwell, M.R. Nelson, Separation and Preconcentration of Actinides by Extraction Chromatography Using a Supported Liquid Anion-Exchanger - Application to the Characterization of High-Level Nuclear Waste Solutions, Anal. Chim. Acta, 310 (1995) 63-78.

[15] C.D. Bowman, E.D. Arthur, P.W. Lisowski, G.P. Lawrence, R.J. Jensen, J.L. Anderson, B. Blind, M. Cappiello, J.W. Davidson, T.R. England, L.N. Engel, R.C.

Haight, H.G. Hughes, J.R. Ireland, R.A. Krakowski, R.J. Labauve, B.C. Letellier, R.T. Perry, G.J. Russell, K.P. Staudhammer, G. Versamis, W.B. Wilson, Nuclear-Energy Generation and Waste Transmutation Using an Accelerator-Driven Intense Thermal-Neutron Source, Nucl. Instrum. Methods Phys. Res., Sect. A, 320 (1992) 336-367.

[16] R.A. Jameson, G.P. Lawrence, C.D. Bowman, Accelerator-Driven Transmutation Technology for Incinerating Radioactive-Waste and for Advanced Application to Power Production, Nucl. Instrum. Methods Phys. Res., Sect. B, 68 (1992) 474-480.

[17] W.M. Stacey, J. Mandrekas, E.A. Hoffman, Sub-Critical Transmutation Reactors with Tokamak Fusion Neutron Sources, Fusion Sci. Technol., 47 (2005) 1210-1218.

[18] F. De Corte, A. Simonits, K_0-Measurements and Related Nuclear-Data Compilation for (N, Gamma) Reactor Neutron-Activation Analysis, Journal of Radioanalytical and Nuclear Chemistry-Articles, 133 (1989) 43-130.

[19] E. Gryntakis, D.E. Cullen, G. Mundy, Thermal Neutron Cross-Sections and Infinite Dilution Resonance Integrals, 1987, pp. 199-260.

[20] S.F. Mughabghab, Neutron Cross Sections, Vol. 1: Neutron Resonance Parameters and Thermal Cross Sections, Pt. B:Z = 61-100, Academic Press, Inc., 1984.

[21] S.F. Mughabghab, M. Divadeenam, N.E. Holden, Neutron Cross Sections, Vol. 1: Neutron Resonance Parameters and Thermal Cross Sections, Pt. A: Z = 1-60, Academic Press, 1981.

[22] A.L. Nichols, D.L. Aldama, M. Verpelli, Handbook of Nuclear Data for Safeguards: Database Extensions, August 2008, Vienna International Centre, P.O. Box 100, A-1400 Vienna, Austria, 2008.

[23] T.A. Todd, R.A. Wigeland, Advanced Separation Technologies for Processing Spent Nuclear Fuel and the Potential Benefits to a Geologic Repository, in: Separations for the Nuclear Fuel Cycle in the 21st Century, American Chemical Society, Washington, DC, 2006, pp. 41-55.

[24] G.R. Choppin, Technology for Nuclear Reprocessing: Present and Future Directions, Sep. Sci. Technol., 41 (2006) 1955-1963.

[25] A. Clearfield, J.A. Stynes, The Preparation of Crystalline Zirconium Phosphate and Some Observations on Its Ion Exchange Behaviour, J. Inorg. Nucl. Chem., 26 (1964) 117-129.

[26] A. Clearfield, W.L. Duax, Crystal Structure of Ion Exchanger Zirconium Bis(Monohydrogen Orthoarsenate) Monohydrate, Acta Crystallogr., Sect. B: Struct. Sci., 25 (1969) 2658-2662.

[27] J.M. Troup, A. Clearfield, Mechanism of Ion-Exchange in Zirconium-Phosphates .20. Refinement of Crystal-Structure of Alpha-Zirconium Phosphate, Inorg. Chem., 16 (1977) 3311-3314.

[28] A. Clearfield, Inorganic-Ion Exchangers with Layered Structures, Annu. Rev. Mater. Sci., 14 (1984) 205-229.

[29] A. Clearfield, J.R. Berman, On the Mechanism of Ion-Exchange in Zirconium-Phosphates. 34. Determination of the Surface-Areas of Alpha-$Zr(HPO_4)_2$-H_2O by Surface Exchange, J. Inorg. Nucl. Chem., 43 (1981) 2141-2142.

[30] A. Clearfield, G.A. Day, A. Ruvarac, S. Milonjic, On the Mechanism of Ion-Exchange in Zirconium-Phosphates. 29. Calorimetric Determination of Heats of K^+-H^+ Exchange with Alpha-Zirconium Phosphate, J. Inorg. Nucl. Chem., 43 (1981) 165-169.

[31] L. Kullberg, A. Clearfield, Mechanism of Ion-Exchange in Zirconium-Phosphates. 31. Thermodynamics of Alkali-Metal Ion-Exchange on Amorphous ZrP, J. Phys. Chem., 85 (1981) 1578-1584.

[32] L. Kullberg, A. Clearfield, Mechanism of Ion-Exchange in Zirconium-Phosphates. 32. Thermodynamics of Alkali-Metal Ion-Exchange on Crystalline Alpha-ZrP, J. Phys. Chem., 85 (1981) 1585-1589.

[33] L. Kullberg, A. Clearfield, On the Mechanism of Ion-Exchange in Zirconium-Phosphates. 35. An Equilibrium Study of Na^+-Cs^+-H^+ Exchange on Crystalline Alpha-Zirconium Phosphate, J. Inorg. Nucl. Chem., 43 (1981) 2543-2548.

[34] G. Alberti, M.G. Bernasconi, M. Casciola, U. Costantino, Ion-Exchange of Some Divalent and Trivalent Cations on Surface of Zirconium Acid Phosphate Micro-Crystals, J. Chromatogr., 160 (1978) 109-115.

[35] G. Alberti, Syntheses, Crystalline-Structure, and Ion-Exchange Properties of Insoluble Acid Salts of Tetravalent Metals and Their Salt Forms, Acc. Chem. Res., 11 (1978) 163-170.

[36] G. Alberti, M. Casciola, U. Costantino, G. Levi, Inorganic-Ion Exchange Membranes Consisting of Microcrystals of Zirconium-Phosphate Supported by Kynar, J. Membr. Sci., 3 (1978) 179-190.

[37] G. Alberti, M.G. Bernasconi, M. Casciola, U. Costantino, Ion-Exchange Processes on the Surface of Micro-Crystals of Zirconium Bis-(Monohydrogen Ortho-Phosphate) Monohydrate, Ann. Chim. (Rome), 68 (1978) 265-274.

[38] A. Clearfield, A. Oskarsson, C. Oskarsson, On the Mechanism of Ion Exchange in Crystalline Zirconium Phosphates. VI. The Effect of Crystallinity of the Exchanger on Na^+/H^+ Exchange, Ion Exch. Membr., 1 (1972) 91-107.

[39] C.B. Amphlett, L.A. Mcdonald, M.J. Redman, Synthetic Inorganic Ion-Exchange Materials .1. Zirconium Phosphate, J. Inorg. Nucl. Chem., 6 (1958) 220-235.

[40] W.J. Boo, L.Y. Sun, J. Liu, A. Clearfield, H.J. Sue, Effective Intercalation and Exfoliation of Nanoplatelets in Epoxy via Creation of Porous Pathways, J. Phys. Chem. C, 111 (2007) 10377-10381.

[41] R.Z. Ma, T. Sasaki, Nanosheets of Oxides and Hydroxides: Ultimate 2D Charge-Bearing Functional Crystallites, Adv. Mater., 22 (2010) 5082-5104.

[42] L.Y. Sun, W.J. Boo, D.H. Sun, A. Clearfield, H.J. Sue, Preparation of Exfoliated Epoxy/Alpha-Zirconium Phosphate Nanocomposites Containing High Aspect Ratio Nanoplatelets, Chem. Mater., 19 (2007) 1749-1754.

[43] G. Alberti, U. Costantino, S. Allulli, N. Tomassini, Crystalline $Zr(R\text{-}PO_3)_2$ and $Zr(R\text{-}OPO_3)_2$ Compounds (R = Organic Radical): A New Class of Materials Having Layered Structure of the Zirconium Phosphate Type, J. Inorg. Nucl. Chem., 40 (1978) 1113-1117.

[44] M.D. Poojary, H.L. Hu, F.L. Campbell, A. Clearfield, Determination of Crystal-Structures from Limited Powder Data Sets - Crystal-Structure of Zirconium Phenylphosphonate, Acta Crystallogr., Sect. B: Struct. Sci., 49 (1993) 996-1001.

[45] A. Clearfield, Z.K. Wang, Organically Pillared Microporous Zirconium Phosphonates, J. Chem. Soc., Dalton Trans., (2002) 2937-2947.

[46] M.B. Dines, P.M. Digiacomo, K.P. Callahan, P.C. Griffith, R.H. Lane, R.E. Cooksey, Derivatized Layered M(IV) Phosphonates, in: Chemically Modified Surfaces in Catalysis and Electrocatalysis, American Chemical Society, 1982, pp. 223-240.

[47] G. Alberti, U. Costantino, J. Kornyei, M.L.L. Giovagnotti, Derivatives of Alpha-Zirconium Phosphate with 2 Different Functional-Groups, React. Polym., 4 (1985) 1-10.

[48] R. Cahill, B. Shpeizer, G.Z. Peng, L. Bortun, A. Clearfield, Use of Selective Inorganic Ion Exchangers for the Separation of Rare Earths, in: Separations of F Elements, Plenum Press, New York, NY, 1995, pp. 165-176.

[49] A. Clearfield, Inorganic Ion Exchange Materials for Nuclear Waste Effluent Treatment, in: D.T. Sawyer, A.E. Martell (Eds.) Industrial Environmental Chemistry, Plenum Press, New York, NY, 1992, pp. 289-299.

[50] L. Pauling, The Nature of the Chemical Bond and the Structure of Molecules and Crystals: An Introduction to Modern Structural Chemistry, Cornell University Press, 1960.

[51] A. Clearfield, Unconventional Metal Organic Frameworks: Porous Cross-Linked Phosphonates, Dalton Trans., (2008) 6089-6102.

[52] G.E.P. Box, Robustness in the Strategy of Scientific Model Building, in: R.L. Launer, G.N. Wilkinson (Eds.) Robustness In Statistics, Academic Press, New York, NY, 1979.

[53] G.E.P. Box, N.R. Draper, Empirical Model-Building and Response Surfaces, Wiley, 1987.

[54] F.G. Helfferich, Ion Exchange, Dover Publications, 1995.

[55] J. Lehto, R. Harjula, Experimentation in Ion Exchange Studies - The Problem of Getting Reliable and Comparable Results, React. Funct. Polym., 27 (1995) 121-146.

[56] T. Hirao, T. Masunaga, Y. Ohshiro, T. Agawa, Stereoselective Synthesis of Vinylphosphonate, Tetrahedron Lett., 21 (1980) 3595-3598.

[57] T. Hirao, T. Masunaga, N. Yamada, Y. Ohshiro, T. Agawa, Palladium-Catalyzed New Carbon-Phosphorus Bond Formation, Bull. Chem. Soc. Jpn., 55 (1982) 909-913.

[58] Y. Belabassi, S. Alzghari, J.L. Montchamp, Revisiting the Hirao Cross-Coupling: Improved Synthesis of Aryl and Heteroaryl Phosphonates, J. Organomet. Chem., 693 (2008) 3171-3178.

[59] H. Perry, J. Zon, J. Law, A. Clearfield, Structural Variations of Sn-II Pyridylphosphonates Influenced by an Uncommon Sn-N Interaction, J. Solid State Chem., 183 (2010) 1165-1173.

[60] H. Moriyama, A. Kitamura, K. Fujiwara, H. Yamana, Analysis of Mononuclear Hydrolysis Constants of Actinide Ions by Hard Sphere Model, Radiochim. Acta, 87 (1999) 97-104.

[61] E. Mauerhofer, K. Zhernosekov, F. Rosch, Limiting transport properties of lanthanide and actinide ions in pure water, Radiochim. Acta, 91 (2003) 473-477.

[62] G.R. Choppin, L.F. Rao, Complexation of Pentavalent and Hexavalent Actinides by Fluoride, Radiochim. Acta, 37 (1984) 143-146.

[63] G. Alberti, F. Marmottini, R. Vivani, P. Zappelli, Preparation and Characterization of Pillared Zirconium Phosphite-Diphosphonates with Tuneable Inter-Crystal Mesoporosity, J. Porous Mater., 5 (1998) 221-226.

[64] L.Y. Sun, W.J. Boo, H.J. Sue, A. Clearfield, Preparation of Alpha-Zirconium Phosphate Nanoplatelets with Wide Variations in Aspect Ratios, New J. Chem., 31 (2007) 39-43.

[65] A. Clearfield, G.D. Smith, Ion Exchange Behaviour of Crystalline Zirconium Phosphate Towards Alkaline Earth Cations, J. Inorg. Nucl. Chem., 30 (1968) 327-329.

[66] Z.K. Wang, J.M. Heising, A. Clearfield, Sulfonated Microporous Organic-Inorganic Hybrids as Strong Bronsted Acids, J. Am. Chem. Soc., 125 (2003) 10375-10383.

[67] A. Cabeza, M.D. Gomez-Alcantara, P. Olivera-Pastor, I. Sobrados, J. Sanz, B. Xiao, R.E. Morris, A. Clearfield, M.A.G. Aranda, From Non-Porous Crystalline to Amorphous Microporous Metal(IV) Bisphosphonates, Microporous Mesoporous Mater., 114 (2008) 322-336.

[68] J.D. Wang, A. Clearfield, G.Z. Peng, Preparation of Layered Zirconium Phosphonate Phosphate, Zirconium Phosphonate Phosphite and Related-Compounds, Mater. Chem. Phys., 35 (1993) 208-216.

[69] S. Pawsey, M. McCormick, S. De Paul, R. Graf, Y.S. Lee, L. Reven, H.W. Spiess, H-1 Fast MAS NMR Studies of Hydrogen-Bonding Interactions in Self-Assembled Monolayers, J. Am. Chem. Soc., 125 (2003) 4174-4184.

[70] N.J. Clayden, Solid-State Nuclear-Magnetic-Resonance Spectroscopic Study of Gamma-Zirconium Phosphate, J. Chem. Soc., Dalton Trans., (1987) 1877-1881.

[71] A.K. Cheetham, N.J. Clayden, C.M. Dobson, R.J.B. Jakeman, Correlations between P-31 Nmr Chemical-Shifts and Structural Parameters in Crystalline Inorganic Phosphates, J. Chem. Soc., Chem. Commun., (1986) 195-197.

[72] D.J. Maclachlan, K.R. Morgan, P-31 Solid-State NMR-Studies of the Structure of Amine-Intercalated Alpha-Zirconium Phosphate - Reaction of Alpha-Zirconium Phosphate with Excess Amine, J. Phys. Chem., 94 (1990) 7656-7661.

[73] H. Nakayama, T. Eguchi, N. Nakamura, S. Yamaguchi, M. Danjyo, M. Tsuhako, Structural Study of Phosphate Groups in Layered Metal Phosphates by High-Resolution Solid-State P-31 NMR Spectroscopy, J. Mater. Chem., 7 (1997) 1063-1066.

[74] M.D. Gomez-Alcantara, A. Cabeza, P. Olivera-Pastor, F. Fernandez-Moreno, I. Sobrados, J. Sanz, R.E. Morris, A. Clearfield, M.A.G. Aranda, Layered Microporous Tin(IV) Bisphosphonates, Dalton Trans., (2007) 2394-2404.

[75] M.J. Hudson, A.D. Workman, High-Resolution Solid-State P-31 and Sn-119 Magic-Angle Spinning Nuclear-Magnetic-Resonance Studies of Amorphous and Microcrystalline Layered Metal(Iv) Hydrogenphosphates, J. Mater. Chem., 1 (1991) 375-379.

[76] A.B. Yaroslavtsev, Z.N. Prozorovskaya, V.F. Chuvaev, V.V. Parshutkin, G.G. Shifanova, Structure and Properties of Tin Acidic Phosphate, Zh. Neorg. Khim., 34 (1989) 1188-1192.

[77] J.I. Corredor, B. Leon, C.P. Vicente, J.L. Tirado, Local Effects of the Electrochemical Reaction of Lithium with Sn_2ClPO_4 and $SnHPO_4$: A Combined P-31, Li-7 MAS NMR and Sn-119 Mossbauer Spectroscopy Study, J. Phys. Chem. C, 112 (2008) 17436-17442.

[78] B.J. Mincher, G. Modolo, S.P. Mezyk, Review: The Effects of Radiation Chemistry on Solvent Extraction 4: Separation of the Trivalent Actinides and Considerations for Radiation-Resistant Solvent Systems, Solvent Extr. Ion Exch., 28 (2010) 415-436.

[79] J.D. Burns, A. Clearfield, M. Borkowski, D.T. Reed, Pillared Metal(IV) Phosphate-Phosphonate Extraction of Actinides, Radiochim. Acta, 100 (2012) 381-387.

[80] G. Dupouy, I. Bonhoure, S.D. Conradson, T. Dumas, C. Hennig, C. Le Naour, P. Moisy, S. Petit, A.C. Scheinost, E. Simoni, C. Den Auwer, Local Structure in Americium and Californium Hexacyanoferrates - Comparison with Their Lanthanide Analogues, Eur. J. Inorg. Chem., (2011) 1560-1569.

[81] K.B. Krauskopf, Thorium and Rare-Earth-Metals as Analogs for Actinide Elements, Chem. Geol., 55 (1986) 323-335.

[82] D.L. Clark, S.S. Hecker, G.D. Jarvinen, M.P. Neu, Plutonium, in: L.R. Morss, N.M. Edelstein, J. Fuger (Eds.) The Chemistry of the Actinide and Transactinide Elements, Springer, Netherlands, 2011, pp. 813-1264.

[83] J.J. Katz, G.T. Seaborg, L.R. Morss, The Chemistry of the Actinide Elements, in: The Chemistry of the Actinide Elements, Chapman and Hall, 1986.

[84] G.R. Choppin, Actinide Speciation in the Environment, J. Radioanal. Nucl. Chem., 273 (2007) 695-703.

[85] W.H. Runde, B.J. Mincher, Higher Oxidation States of Americium: Preparation, Characterization and Use for Separations, Chem. Rev., 111 (2011) 5723-5741.

[86] L.B. Asprey, S.E. Stephanou, R.A. Penneman, A New Valence State of Americium, Am(VI), J. Am. Chem. Soc., 72 (1950) 1425-1426.

[87] L.B. Werner, I. Perlman, The Pentavalent State of Americium, J. Am. Chem. Soc., 73 (1951) 495-496.

[88] J.S. Coleman, Kinetics of Disproportionation of Americium (V), Inorg. Chem., 2 (1963) 53-57.

[89] J.S. Coleman, W.T. Carnall, L.H. Jones, R.A. Penneman, T.K. Keenan, Preparation and Properties of Americium(VI) in Aqueous Carbonate Solutions, Inorg. Chem., 2 (1963) 58-61.

[90] M. Hara, Chemistry of Americium. I. A Study of Preparation of Am(V) and Its Behavior by Means of TTA Extraction, Bull. Chem. Soc. Jpn., 43 (1970) 89-94.

[91] W.W. Schulz, The Chemistry of Americium, DOE Technical Information Center, Oak Ridge, TN, 1976.

[92] M. Hara, S. Suzuki, Chemistry of Americium. IV. Stability of Am(V) and Am(VI) in Nitric-Acid Solutions and in the Solutions Containing Ozone Gas, Fluoride, or Phosphate Ions, Bull. Chem. Soc. Jpn., 52 (1979) 1041-1045.

[93] D.E. Hobart, K. Samhoun, J.R. Peterson, Spectroelectrochemical Studies of the Actinides - Stabilization of Americium (IV) in Aqueous Carbonate Solution, Radiochim. Acta, 31 (1982) 139-145.

[94] J.Y. Bourges, B. Guillaume, G. Koehly, D.E. Hobart, J.R. Peterson, Coexistence of Americium in 4 Oxidation-States in Sodium-Carbonate Sodium-Bicarbonate Medium, Inorg. Chem., 22 (1983) 1179-1184.

[95] S. Magirius, W.T. Carnall, J.I. Kim, Radiolytic Oxidation of Am(III) to Am(V)in NaCl Solutions, Radiochim. Acta, 38 (1985) 29-32.

[96] B.J. Mincher, L.R. Martin, N.C. Schmitt, Tributylphosphate Extraction Behavior of Bismuthate-Oxidized Americium, Inorg. Chem., 47 (2008) 6984-6989.

[97] T. Shehee, L.R. Martin, P.R. Zalupski, K.L. Nash, Redox-Based Separation of Americium from Lanthanides in Sulfate Media, Sep. Sci. Technol., 45 (2010) 1743-1752.

[98] T.W. Newton, Kinetics of the Oxidation-Reduction Reactions of Uranium, Neptunium, Plutonium, and Americium in Aqueous Solutions, NTIS, 1975. http://www.osti.gov/bridge/servlets/purl/4188896-Y9ogJf/native/4188896.pdf

[99] M. Ward, G.A. Welch, The Oxidation of Americium to the Sexavalent State, J. Chem. Soc., (1954) 4038-4038.

[100] T.W. Newton, The Kinetics of the Oxidation-Reduction Reactions of Uranium, Neptunium and Americium in Aqueous Solutions, 1975.

[101] J.D. Burns, M. Borkowski, A. Clearfield, D.T. Reed, Separation of Oxidized Americium from Lanthanides by use of Pillared Metal(IV) Phosphate-Phosphonate Hybrid Materials, Radiochim. Acta, in press (2013).

[102] J.D. Burns, T.C. Shehee, A. Clearfield, D.T. Hobbs, Separation of Americium from Curium by Oxidation and Ion Exchange, Anal. Chem., 84 (2012) 6930-6932.

[103] W. Rigby, Oxidations with Sodium Bismuthate - Glycol Fission and Related Reactions, J. Chem. Soc., (1950) 1907-1913.

[104] W. Rigby, Sodium Bismuthate as an Oxidizing Agent for Organic Compounds, Nature, 164 (1949) 185-186.

[105] J.F. Lhotka, Histochemical Use of Sodium Bismuthate, Stain Technol, 27 (1952) 259-262.

[106] E.D. Collins, C.G.D. Del, B.A. Moyer, Advanced Reprocessing for Fission Product Separation and Extraction, in: Woodhead Publishing Series in Energy, Woodhead Publishing Ltd., 2011, pp. 201-228.

[107] G. Modolo, P. Kluxen, A. Geist, Demonstration of the LUCA Process for the Separation of Americium(III) from Curium(III), Californium(III), and Lanthanides(III) in Acidic Solution Using a Synergistic Mixture of Bis(Chlorophenyl)Dithiophosphinic Acid and Tris(2-Ethylhexyl)Phosphate, Radiochim. Acta, 98 (2010) 193-201.

[108] S. Trumm, A. Geist, P.J. Panak, T. Fanghanel, An Improved Hydrolytically-Stable Bis-Triazinyl-Pyridine (BTP) for Selective Actinide Extraction, Solvent Extr. Ion Exch., 29 (2011) 213-229.

[109] K. Hayasaka, T. Kaneshiki, M. Nomura, T. Suzuki, Y. Fujii, Calcium Ion Selectivity and Isotope Effects Studied by Using Benzo-18-Crown-6 Resins, Prog. Nucl. Energ., 50 (2008) 510-513.

[110] T. Kimura, J. Akatsu, Extraction Chromatography in the DHDECMP-Nitric Acid System. I. Extraction Behavior of Cerium(III) and Americium(III) with the DHDECMP/XAD-4 Resin, J. Radioanal. Nucl. Chem., 149 (1991) 13-23.

[111] T. Kimura, J. Akatsu, Extraction Chromatography in the DHDECMP-Nitric Acid System. II. Characteristics of the DHDECMP/XAD-4 Resin on Separation of Trivalent Actinide Elements, J. Radioanal. Nucl. Chem., 149 (1991) 25-34.

[112] H. Kurosaki, S.B. Clark, Chromatographic Separation of Am and Cm, Radiochim. Acta, 99 (2011) 65-69.

[113] G.R. Choppin, Comparison of the Solution Chemistry of the Actinides and Lanthanides, J. Less-Common Met., 93 (1983) 323-330.

[114] C.J. Burns, B.E. Bursten, Covalency in f-Element Organometallic Complexes: Theory and Experiment, Comments Inorg. Chem., 9 (1989) 61-93.

[115] M.P. Jensen, L.R. Morss, J.V. Beitz, D.D. Ensor, Aqueous Complexation of Trivalent Lanthanide and Actinide Cations by N,N,N ',N '-Tetrakis(2-Pyridylmethyl)Ethylenediamine, J. Alloys Compd., 303 (2000) 137-141.

[116] K.L. Nash, A Review of the Basic Chemistry and Recent Developments in Trivalent F-Elements Separations, Solvent Extr. Ion Exch., 11 (1993) 729-768.

[117] B.F. Smith, G.D. Jarvinen, M.M. Jones, P.J. Hay, The Synthesis and Actinide and Lanthanide Complexation of Soft Donor Ligands - Comparison between 4-Benzoyl-2,4-

Dihydro-5-Methyl-2-Phenyl-3H-Pyrazol-3-Thione (HBMPPT) and 4-Thiobenzoyl-2,4-Dihydro-5-Methyl-2-Phenyl-3H-Pyrazol-3-One (HTBMPP) with Tri-n-Octylphosphine Oxide (TOPO) Synergist for Am(III) and Eu(III) Extraction, Solvent Extr. Ion Exch., 7 (1989) 749-765.